2002-05-10

Development of an Unstructured 3-D Direct Simulation Monte Carlo/Particle-in-Cell Code and the Simulation of Microthruster Flows

Jeffrey Robert Hammel
Worcester Polytechnic Institute

DEVELOPMENT OF AN UNSTRUCTURED 3-D DIRECT SIMULATION MONTE CARLO/PARTICLE-IN-CELL CODE AND THE SIMULATION OF MICROTHRUSTER FLOWS

by

Jeffrey Robert Hammel

A Thesis submitted to the Faculty of the

WORCESTER POLYTECHNIC INSTITUTE

in partial fulfillment of the requirements for the

Degree of Master of Science

in

Mechanical Engineering

by

_____

Jeffrey Robert Hammel

March 8, 2002

APPROVED:

_____

Dr. Nikolaos A. Gatsonis, Advisor
Mechanical Engineering Department

_____

Dr. John Blandino, Committee Member
Mechanical Engineering Department

_____

Dr. Grétar Tryggvason, Committee Member
Mechanical Engineering Department

_____

Dr. Mark Richman, Graduate Committee Representative
Mechanical Engineering Department

Abstract

This work is part of an effort to develop an unstructured, three-dimensional, direct simulation Monte Carlo/particle-in-cell (DSMC/PIC) code for the simulation of non-ionized, fully ionized and partially-ionized flows in micropropulsion devices. Flows in microthrusters are often in the transitional to rarefied regimes, requiring numerical techniques based on the kinetic description of the gaseous or plasma propellants. The code is implemented on unstructured tetrahedral grids to allow discretization of arbitrary surface geometries and includes an adaptation capability.

In this study, an existing 3D DSMC code for rarefied gasdynamics is improved with the addition of the variable hard sphere model for elastic collisions and a vibrational relaxation model based on discrete harmonic oscillators. In addition the existing unstructured grid generation module of the code is enhanced with grid-quality algorithms. The unstructured DSMC code is validated with simulation of several gaseous micronozzles and comparisons with previous experimental and numerical results. Rothe's 5-mm diameter micronozzle operating at 80 Pa is simulated and results are compared favorably with the experiments. The Gravity Probe-B micronozzle is simulated in a domain that includes the injection chamber and plume region. Stagnation conditions include a pressure of 7 Pa and mass flow rate of 0.012 mg/s. The simulation examines the role of injection conditions in micronozzle simulations and results are compared with previous Monte Carlo simulations. The code is also applied to the simulation of a parabolic planar micronozzle with a 15.4-

micron throat and results are compared with previous 2D Monte Carlo simulations. Finally, the code is applied to the simulation of a 34-micron throat MEMS-fabricated micronozzle. The micronozzle is planar in profile with sidewalls binding the upper and lower surfaces. The stagnation pressure is set at 3.447 kPa and represents an order of magnitude lower pressure than used in previous experiments. The simulation demonstrates the formation of large viscous boundary layers in the sidewalls.

A particle-in-cell model for the simulation of electrostatic plasmas is added to the DSMC code. Solution to Poisson's equation on unstructured grids is obtained with a finite volume implementation. The Poisson solver is validated by comparing results with analytic solutions. The integration of the ionized particle equations of motion is performed via the leapfrog method. Particle gather and scatter operations use volume weighting with linear Lagrange polynomial to obtain an acceptable level of accuracy. Several methods are investigated and implemented to calculate the electric field on unstructured meshes. Boundary conditions are discussed and include a formulation of plasma in bounded domains with external circuits. The unstructured PIC code is validated with the simulation of a high voltage sheath formation.

Acknowledgments

The author wishes to thank those without whose support this thesis would not be possible.

My thanks go out to my advisor, Professor Nikolaos Gatsonis, who introduced me to the field of plasma physics and laid the foundation for a deep appreciation of the field. Thank you for your aid and support on this project.

I would also like to thank the authors of the DSMC solver, Valeriy Tenishev, and the unstructured grid generator, Konstantin Kovalev. Your programs taught me much about programming and computational problem solving. Thank you for providing a firm basis on which to build my thesis. I hope I have given you credit where credit is due in this work.

Thank you to all of the teachers who have gone beyond the call of duty and who taught me that engineering and science is an art of contemplation. In particular, let me acknowledge Professor John Sullivan, Jr. for an intriguing introduction to numerical methods, Professor Vladimir Entov for introducing me to the kinetic theory of gases, and Professor John Davies of Clarke University for teaching me electrodynamics. I would like to think your skills as teachers show through in this thesis. Your contributions will not be forgotten.

Thank you to all of those at the Computational Gas and Plasmadynamics Laboratory, both past and present, for your intellectual and social contributions.

I would also like to thank my parents and grandparents for their financial and moral support throughout my education.

Last, but certainly not least, I would like to thank my fiancée Sarah Foster for never losing faith in me and putting up with the late night runs up to lab to check on one of my programs. I couldn't have done it without you.

Support from AFOSR Grant No. F49620-00-1-0278 is greatly appreciated.

Table of Contents

Table of Figures

Nomenclature

SI units were used throughout this work. When a symbol corresponds to more than parameter, the variable of interest will be made clear by the context. Boldface denotes vector or matrix (tensor) quantities. The magnitude of a vector is denoted using the same symbol without boldface type. Parameters not listed here are denoted explicitly in the text.

A	area
B	magnetic flux density
C	capacitance
c	speed of light in free space
D	electric displacement
d	molecular diameter
E	electric field
E	energy
e	elementary charge (1.602177×10^{-19} coulombs)
F	force vector
f	distribution function
g	relative velocity
H	magnetic field
h	(local) characteristic mesh spacing; also, Planck's constant

I	current
j	current density
k	Boltzmann's constant (1.380658×10^{-23} J/K)
Kn	Knudsen number
L	inductance
m	mass
N	number of nodes
$N_{F,i}$	number of neighbors of node *i*
$\hat{\mathbf{n}}$	unit normal vector (outward, where applicable)
n	number density; also, time-step counter
Q	total charge
q	electric charge
R	resistance
r	(radial) distance
Re	Reynolds number
T	temperature
t	time
v	velocity vector
x	position vector
Θ	characteristic temperature
Λ	fraction of inelastic collisions

Ξ average degrees of freedom

Φ (electric) scalar potential

α thermal accommodation coefficient

ε electric permittivity; also, angle between collisional plane and local x-y plane

ε_o permittivity of free space

θ (impact) angle

λ mean free length; also, wavelength

μ magnetic permeability

μ_o permeability of free space

ν variable hard sphere exponent; also, frequency

ρ density (of mass or charge)

σ molecular cross section; also, surface charge density

χ molecular scattering angle

ω viscosity temperature exponent

Subscripts

* nozzle throat (sonic) condition; also post-collisional values

c capacitor

cm center of mass

conv convective

De Debye

e	electron
i	ion
M	momentum
ref	reference
rot	rotational
S	surface
T	total
tr	translational
V	volume
vib	vibrational
x	x-component
y	y-component
z	z-component

Chapter 1

1.1 Introduction

The increasingly prolific nature of microspacecraft has motivated interest in smaller propulsion systems. As electronics continue to be manufactured with greater capabilities at smaller sizes, new space missions are conceived of consisting of capable spacecraft with minimal weight. Micropropulsion is a mission enabling technology for microspacecraft, providing precision maneuvering necessary for the nature of such craft. Missions consisting of constellations of microspacecraft have been conceived of where the precision maneuvering and communication among the spacecraft lead to collective capabilities, such as an antenna with an aperture equal the diameter of the constellation (*Schilling et al., 2000)*. Manufacturing techniques similar to those used in MEMS (Micro Electro Mechanical Systems) have enabled the precision manufacture of very small propulsion systems.

Microthrusters typically have thrusts in the millinewton range and are applicable for use as precision manuevering propulsion for spacecraft up to 100 kg and as primary propulsion for smaller spacecraft. Table 1 summarizes the classes of microspacecraft and applicability of micropropulsion (reproduced from *Mueller, 2000*).

Table 1: Classication of Microspacecraft (from *Mueller, 2000*)

Designation	Spacecraft mass, kg	Spacecraft power, W	Spacecraft dimension, m
Microspacecraft (Air Force/European definition)	10-100	10-100	0.3-1
Class I microspacecraft (≤10 kg, nanosat)	5-20	5-20	0.2-0.4
Class II microspacecraft	1-5	1-5	0.1-0.2
Class III microspacecraft (picosat)	<1	<1	<0.1

Micropropulsion was considered to some degree during the 1960s and earlier. Early efforts involving low-thrust propulsion were mainly concerned with station-keeping, as the miniaturization of electronics at this phase of space exploration had not matured to allow microspacecraft in the modern sense of the word. It is worth mentioning that Explorer I would fit into the category of microspacecraft, having a mass of 14.5 kg (*Ketsdever and Micci, 2000*). A modern focus in microspacecraft research involves the complete integration of technologies in a light but highly capable package. Towards this end, new manufacturing techniques are being developed, some similar to those used for the manufacture of MEMS.

Micropropulsion may be classified by the dominant thrust production mechanism as cold-gas, chemical, electrothermal, electrostatic, or electromagnetic. Cold-gas microthrusters derive all of their energy from this thermodynamic

expansion. An example of a cold-gas microthruster is shown in Figure 1 (courtesy of Robert Bayt). Chemical reactions may also be used to increase thrust levels – however, only a few chemical microthrusters have so far been investigated due to the complexity of regulating a chemical reaction reliably on such a small scale. Electrical microthrusters appear more promising as electrical energy may in principle be converted to mechanical thrust with no limit on power supply (save weight and thermal considerations) . The efficiency of the propulsion system is of concern both in terms of energy and in the velocity imparted to a unit mass of propellant (specific impulse). A thruster with high energy-efficiency and specific impulse minimizes the size and weight of the power supply (for electric micropropulsion) and propellant.

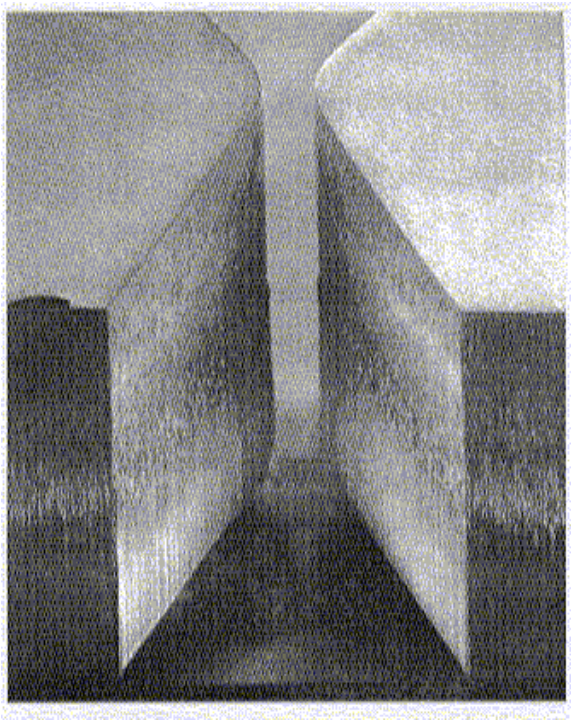

Figure 1. MEMS Micronozzle, 19 micron throat, 5.4:1 expansion ratio (from *Bayt, 1999)*

The optimization of micropropulsion systems is an issue of increasing concern. Currently, many micropropulsion devices have low efficiencies in terms of directed kinetic energy versus potential energy (thermal, chemical, and electrical) due to a lack of understanding of the flows in such devices. In order to improve micropropulsion techniques, the flows of such devices must be modeled in order to gain insight into the driving thrust mechanisms. With accurate models of microthrusters, engineers may improve the operation of such devices through minimization of loss mechanisms and corresponding increase of thrust and specific impulse. The optimization of micro propulsion system will enable better performance per unit mass and lead to enablement of microspacecraft systems.

The continuum assumption commonly used in gas and plasma dynamics breaks down at smaller densities and/or characteristic dimensions of flow. The Knudsen number is the ratio of the mean free path of gas molecules to a characteristic dimension of flow. As the Knudsen number becomes larger, the collision rate becomes too low to maintain local thermodynamic equilibrium. Furthermore, the expansion of a propellant from chamber conditions to vacuum often involves flow regimes from continuum to transition to free molecular, though the smallest devices may not have any component in the continuum regime. The transition and free-molecular regimes need to be modeled using kinetic theory. From a computational point, particle-base methods must be used to accurately model transitional micropropulsion flows.

The objective of this thesis is the development of a computational method for the simulation of rarefied and transitional flows in gaseous and plasma micropropulsion devices. The computational model will be based on stochastic particle simulation methods and contain the necessary algorithms for three-dimensional simulations of neutral and fully ionized microflows in arbitrary geometries. This computational method is applied to internal flows of cold-gas microthrusters and electrostatic plasma simulations.

1.1.1 Cold-Gas and Chemical Micropropulsion

In this section, we review the previous work and state of the art of cold-gas and chemical microthrusters. The small thrust levels in traditionally machined nozzles are achieved through use of a low plenum pressure. The use of a low pressure corresponds to low Reynolds number and large boundary layers in the nozzle. In contrast, MEMS nozzles such as shown in Figure 1 use plenum pressures often greater than one atmosphere, minimizing the viscous effects and leading to higher nozzle efficiencies.

Rothe's experiments (*Rothe, 1971*) demonstrated the qualitative difference between high and low Reynolds number nozzle flows. Rotational temperature and number density along the nozzle centerline were measured using analysis of electron-beam fluorescence by two spectrometers. Two graphite nozzles, as shown in Figure 2 (2.5 and 5.1mm throat diameters), were used by Rothe. The test gas was nitrogen at a stagnation temperature of 300K at chamber pressures from 88-2000 Pa. Electron

beams were passed through small holes in the nozzle and reflected to the spectrometers downstream. For higher Reynolds numbers, the temperature decreased along the centerline was monotonic. For more rarified flows, the temperature reached a minimum and increased again, due to the broadening of the viscous boundary layer at low densities.

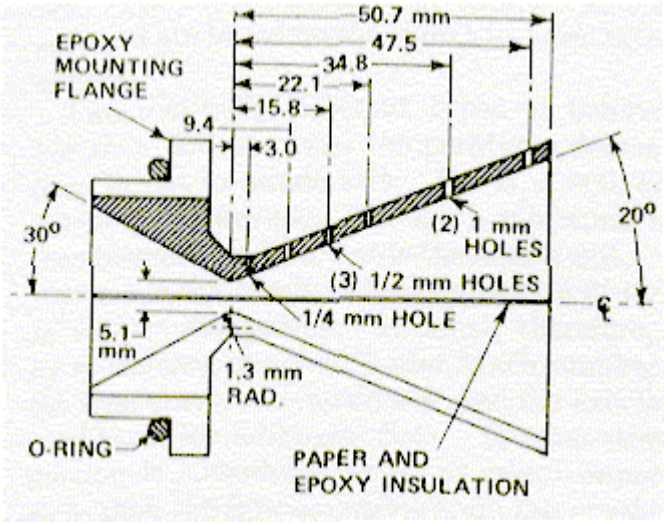

Figure 2. Schematic of Rothe's nozzle with 5.1 mm throat diameter (from *Rothe 1971*)

The Gravity Probe-B (GP-B) spacecraft considered cold-gas micropropulsion as mission-enabling technology. GP-B is scheduled for launch in Septemeber. 2002 (*Mullins, 2000*) and is designed to investigate the relativistic precession of an Earth orbiting gyroscope in a drag-free environment. By monitoring the drag-makeup thrust, detailed information may be obtained about the variations of density and winds of the atmosphere at the orbital altitude of 600 km. The nullification of the drag force is to be accomplished with cold gas thrusters operating in the milli-Newton range.

The experiments on board must be cryogenically cooled, and the boil-off helium used for attitude control and drag correction. The Knudsen number in the nozzle at these conditions is 0.01-1 corresponding to stagnation pressures of 7-930Pa (*Boyd et al., 1994*). The fluid effects and thermal non-equilibrium of this regime lead to experimental (*Jafry et al., 1992*) and computational (*Boyd et al., 1994*) investigations of a prototype nozzle and comparison to theories for this flow regime.

Mass flow measurements of the GP-B prototype nozzle were performed by Jafry and Vanden Beukel (1992) using a helium mass spectrometer in a vacuum facility. The stangation temperature was maintained at 286K. The throat diameter of the prototype nozzle used is 2.5mm and the exit diameter is 5mm. Mass flux relative to centerline values are given in ten-degree increments 2.38 cm from the nozzle exit. The far field plume shape was also observed. Results were compared with free molecular and continuum (Boynton-Simons) models and a good comparison was found with both models.

The most recent advance in micronozzles is their manufacture by techniques used for MEMS. Etching technology as used in the production of integrated circuits may be used to create micropropulsion devices. Isotropic etching may be achieved by wet chemical etching, while anisotropic etching may be achieved with ion etching (*Bayt et al., 1997*). Use of deep reactive ion etching allows the creation of several two-dimensional micronozzles on a single chip. The development of boundary layers on the sidewalls decreases the effectiveness of 2-D MEMS nozzles, however. Three-dimensional nozzles may be created with anisotropic etching of a single silicon

crystal to create converging-diverging with a square cross-section. Laser machining may also be used to create nozzles of arbitrary shape (*Janson et al., 1999*). The use of new manufacturing techniques has facilitated the creation of smaller nozzles than possible with traditional machining techniques. The ability to manufacture smaller nozzles permits lower thrust for higher chamber pressures and Reynolds numbers, which may minimize viscous effects associated with low thrust nozzles (*Ivanov et al., 1999*).

Several geometries (conical, bell, and trumpet) of two-dimensional ion etched micronozzles were investigated experimentally and computationally by *Bayt et al.* (1997). The throat diameter of the nozzles studied was about 30 microns, compared to an etch depth of 370 microns. Nitrogen was used as a propellant at chamber pressures from 1-150 psia (6895-1.03x10^6 Pa), exhausting into an atmospheric or 5 torr (667 Pa) background pressure. Mass flow rates were determined as a function of chamber pressure. At Re = 1000, the Knudsen number was found to be 0.001 at the throat and 0.005 inside the nozzle at the lip. This is well into the velocity slip regime. A two-dimensional finite volume approximation of the Navier-Stokes equation was used to model the micronozzles. The code included velocity slip effects, present in this regime.

Bayt and Breuer (*1998*) measured the discharge coefficients of 2-D nitrogen ion-etched micronozzles. Throat widths were from 18 to 37.5 microns with expansion ratios from 5.4:1 to 17:1. Mass flow rates were measured with a 0-1000 sccm flow meter and thrust measurements were taken on a thrust stand accurate to 1

mN over the range of 1-20 mN. The stagnation pressure was varied between 35,000-689,000 Pa with a constant stagnation temperature of 295.65K (*Bayt,* 1999). A two-dimensional finite volume Navier-Stokes solver was used similar to that used in *Bayt et al., 1997*. Numerical and experimental results increasingly diverged as the Reynolds number decreased. The effects of sidewall boundary layers on thruster performance are discussed and cited as a reason for the disagreement of experiment and two-dimensional numerical calculations. As the Reynolds number drops, the boundary layer thickness increases, decreasing thruster performance.

The ability to batch manufacture several thrusters on a single wafer using MEMS fabrication techniques has enabled the concept of digital microthruster arrays. Each thruster is packaged with propellant and can only be fired once. Chemically reacting propellants are most often recommended for this application, and the disposable nature of such devices eliminate many of the reliability concerns of other chemically propelled microthrusters. The failure of a single thruster is negligible compared to the number of thrusters in the array. The use of digital microthruster arrays is recommended for station keeping and attitude control due to the small impulse bits. Control algorithms for thruster firing must be developed taking into account the thruster position and impulse bits. The advantages of digital microthruster arrays are their simplicity and small discrete impulse bit.

Decomposing solid thrusters using heated filament or laser ignition were fabricated using MEMS manufacturing techniques (deep etching) and tested by *de Groot et al.* (1998). Expansion ratios from 1-25 were considered. The throat width

was 0.3mm and the throat height was 0.55mm. Fuel pellets of $C_2H_4N_6O_2$ reside in each two-dimensional chamber and were ignited to produce nitrogen, hydrogen and carbon monoxide. Screens within the chamber were machined to prevent throat blockage by incompletely decomposed chunks of solid propellant. With an array of similar thrusters, a single laser could be used for ignition of the array. Chamber pressures from 0.22 to 0.1 MPa were achieved with thrusts of the order of Newtons for durations of a few hundred milliseconds. The initial temperature of decomposition was 440-465K and the stagnation temperature was estimated at around 1000K. Laser ignition was not successful; the data for pressure, temperature and thrust reflect only the heated wire ignition. *De Groot et al.* recommend research into alternative solid fuels, as $C_2H_4N_6O_2$ proved unsatisfactory due to poor ignition characteristics from lasers and incomplete decomposition of the propellant.

1.1.2 Electric Micropropulsion

In general, electric propulsion offers an increased specific impulse over cold gas or chemical propulsion. The three types of electric propulsion are electrothermal propulsion (electrically heats the propellant), electrostatic propulsion (derives thrust from the $q\boldsymbol{E}$ force), and electromagnetic propulsion (derives thrust from the $\boldsymbol{j}\times\boldsymbol{B}$ force). It is to be noted that more than one thrust mechanism many be present in a single device. The drive of electric propulsion devices to smaller sizes has been enabled by the miniaturization of power supplies and capacitors as well as MEMS fabrication techniques.

Field emission electric propulsion (FEEP) is an electrostatic propulsion technique offering high specific impulses (~10,000 s) and thrust levels ranging from micro-Newtons to milli-Newtons. These characteristics make FEEP an attractive option for very spacecraft requiring precise control. Liquid metal is fed from a reservoir to a needle-like emitter that is biased to a positive potential relative to an accelerator electrode. A conductor with a small aperture opposite and near to the emitter is biased to a negative potential. Due to the high electric field, the liquid metal forms cusps. At a local electric field strength of 10^6 V/mm, the electrons are stripped off the liquid metal surface through field emission (*Mueller, 2000*). The walls collect the electrons and the ions serve as the propellant. The beam must be neutralized as in an ion thruster to avoid spacecraft charging. A downside of FEEP thrusters is potentially high power requirements due to low thrust to power values (*Mueller, 2000*). As with any propulsion system, trade-off studies must be conducted to determine whether the benefits of FEEP thrusters outweigh the penalties for a particular mission.

The Austrian Research Centre Seibersdorf has investigated FEEP thrusters for space applications including in-orbit operations. *Fehringer et al*. (1999) have experimentally investigated indium FEEP thrusters in attempt to improve their operational efficiency and minimize their weight. The mass efficiency (ratio of ionized mass emitted to total mass emitted) was determined and optimized with improved emitter design. The ionized mass emitted was determined by current collection assuming that all ions were singly ionized. The total mass emitted was

determined from precision weighing. The optimizations substantially improved mass efficiency, especially at higher currents. A 12kV power converter with a maximum current of 1mA was used as the power supply. A 500-microampere current for the optimized thruster corresponds to a thrust of 55 micro-Newtons. The needle diameter was 50 microns at the tip. A compact electron emitter was developed for neutralization of the emitted ions. The effectiveness of the neutralization was tested through use of external current collection in a vacuum facility. The experiments demonstrated charge neutralization of the ion beam. The Austrian program as well as an Italian program using Cesium demonstrate the applicability of FEEP technology to micropropulsion.

Field emission cathodes utilize a large electric field to allow electrons to tunnel off the cathode surface into a vacuum. Field emission cathodes appear promising for use in electric microthrusters, as they may be fabricated using MEMS techniques and have much smaller size and weight than hollow and other thermionic cathodes. In addition, field emission cathodes have a lower power requirement than thermionic cathodes for comparable emission currents.

Pulsed plasma thrusters are unsteady electric propulsion devices that are powered by exposing the propellant to a short-duration current discharge (from a capacitor) in pulses. Pulsed plasma thrusters (PPTs) achieve propellant acceleration from both electrothermal and electromagnetic means. Though gas-fed PPTs have been experimented with, use of Teflon as a propellant for micro-PPTs is more attractive due to the simple feed mechanism and high reliability. To maximize the

efficiency of PPTs, high current discharges across the propellant in each pulse, leading to electromagnetic acceleration as the current increases to the point where maximum inductance is achieved (*Jahn, 1968*). This is similar to the acceleration mechanism of a railgun. Another mode of operation for the PPT is the current arc remaining stationary over the discharge that accelerates the plasma (*Keefer et al., 1997*). The discharge also heats the propellant, leading to thermal (gasdynamic) acceleration. The relative contributions to electrothermal and electromagnetic forms of acceleration depend on the thruster configuration, mass ablated, and characteristics of the circuit.

Keefer and Rhodes (*1997*) present an analytical and computational study of the acceleration mechanisms of a Teflon coaxial pulsed plasma thruster. A model is developed of the maximum possible component of electromagnetic acceleration and compared to the MHD code MACH2. Two ablated masses were considered for the MACH2 simulation: 7.3 and 73 micrograms, where the higher mass is consistent with that of a laboratory PPT model (*Kamhawi et al., 1996*). For the high-mass case, the PPT received most of its thrust from electrothermal acceleration. The MACH2 simulation also showed the current being concentrated near the base of the PPT for the duration of the pulse, similar to a MHD accelerator. For the low-density case, the thruster received substantial electromagnetic contributions to its thrust. The simulation illustrated the current sheet accelerating down the PPT, pushing the propellant in a manner similar to railgun acceleration. The lower density PPT

simulation showed a higher specific impulse and a different mode of acceleration than the higher density case.

The Air Force Research Lab (AFRL) conducted studies of Teflon coaxial Micro-PPTs for use on microsattelites (*Gulczinkski et al., 2000*). Instead of a sparkplug triggering mechanism used traditionally in PPTs, the AFRL designs featured pulsed discharge initiation by semiconductor switches or alternatively a self-triggered design where voltage is applied to a capacitor until the voltage breaks down across the propellant face and the discharge is initiated. Three different propellant diameters were studied: 2.21, 3.58, and 6.35mm. Maximum capacitor energy ranged from 3.3 to 15.2 J for a capacitance of 0.1-0.31μF. The semiconductor switch triggered microPPT produced more consistently repeatable impulse bits than the self-triggered device. Several designs for the self-triggered PPT were considered before finding a configuration that did not fail over 16000 seconds of testing with a firing rate of about 1 Hz. For this configuration, the ablation rate was 1.3 micrograms per discharge with 2.4 J expended per discharge (average). Thrust measurements of the self-triggered PPT were made in a vacuum facility with the thruster was fired in resonance with a thrust stand so that large deflections could be observed. Measured thrusts ranged from 20 to 80 micro-Newtons.

Cassady et al. (*2000*) studied a small rectangular Teflon PPT for use on sattelite constellations in the 10-20 kg regime. The impulse bits produced by the PPT was 70 μN s and its total mass was 3.8 kg. A modular test unit was developed to allow the testing of a wide variety of configurations of electrodes and capacitors. The

dimensions of the propellant bar was 0.76 cm by 3.05 cm, the longer length being the distance between the electrodes. Several capacitors were tested to determine which one produced the short duration high currents required by the PPT: an oil-filled capacitor, a ceramic capacitor, a mica capacitor, and a metallized film capacitor. Current waveforms presented show that all capacitors discharge in under 10 μs. The research presented by *Cassady et al.* (*2000*) continues in the selection of an appropriate capacitor and miniaturization of the power supply for the PPT.

1.2 Modeling of Gaseous Microthrusters

Microthrusters involve the expansion of a propellant into vacuum. As the collision rate falls off in the expansion and flow temperatures freeze (relaxation time >> residence time), the continuum assumption commonly used in Navier-Stokes based CFD codes fails and the accuracy of results suffers. Consequently, particle-based codes such as direct simulation Monte Carlo (DSMC) for gas dynamics and particle in cell (PIC) codes for ionized flows must be used in the portion of the domain where the continuum description breaks down or throughout the flow. Additionally, particle based methods can provide a prediction of backflow and plume impingement on spacecraft. As device scales draw near to the characteristic length of particle interaction, breakdown of the continuum assumption occurs further inside the device and a kinetic description becomes increasingly necessary.

The direct simulation Monte Carlo (DSMC) method for gasdynamics (*Bird, 1994*) is based on a kinetic description and is applicable to flows where local equilibrium breaks down. A number of computational particles are used to

approximate the phase space of the gas. The DSMC method uses the dilute gas assumption that the time of collisions is much less than the time between collisions. The motion and collisional processes are uncoupled in time and it can be shown that the DSMC method is a first-order solution in time to Boltzmann's equation (*Nanbu, 2000*). Collisions are modeled probabilistically using models of molecular cross-sections. Internal energies, chemical reactions, and other behaviour important to the modeling of gases may also be included (*Bird, 1998*). The DSMC method has been applied to many nozzle flows of in the transition regime.

The effects of nozzle geometry and stagnation temperature were studied using the DSMC method by *Zelesnik et al.* (1993) for low Reynolds number nozzle flows. The variable hard sphere molecule was used as the collisional model and the nozzle walls were assumed to be diffusely reflecting. Particles entered the region downstream of the throat according to the results of a Navier-Stokes code. The code was first verified against numerical and experimental results of *Boyd et al, 1992*. The geometries considered were conical, trumpet shaped and bell shaped, chosen with the same throat radius (0.5mm) and area ratio (104.04). Nitrogen was used with stagnation temperatures of 300 K and 1000 K, with stagnation pressure of 1109.6 Pa. Data available in the study were the pressure at the exit plane, temperature fields, velocity vector fields, and Mach contours. The trumpet nozzle proved the most efficient at low temperatures, though the conical nozzle produced the most thrust as it had the highest mass flow rate. For the heated case (1000 K stagnation temperature),

both the trumpet and bell nozzle had comparable efficiencies, 6.5% above that of the conical nozzle.

The Gravity Probe-B prototype cold-gas nozzle was modeled by *Boyd, et al.* (1994) using the DSMC method and compared to experimental results. The simulation was performed on non-uniform, structured, 2-D grids and the nozzle surface was assumed have full thermal accommodation. The calculated angular distribution of mass flux compared well with experiment, as did the plume centerline mass flux and nozzle discharge coefficient. Mach contours interior to the nozzle were presented, as well as velocity profiles along the plume centerline. The effect of back pressure on calculations was shown by comparing simulation results at vacuum to those with a back pressure of 8.7×10^{-4} Pa. This study illustrated the application of DSMC to supersonic micro-flows and confirmed the experimental and theoretical data used in the Gravity Probe-B mission.

Piekos and Breuer (*1996*) presented results for the application of the DSMC method to helium MEMS flows in a micro-channel and micronozzle. The DSMC method used unstructured 2D grids for the benefit of handling arbitrary geometries. The outlet Knudsen numbers in the channel flows was between 0.05 and 0.44. Boundary conditions for these subsonic cases came from the method of characteristics using a weighted time average of flow statistics. The interior of a 2-D parabolic micronozzle was also simulated with a 15.4 micron throat height and a nozzle length of 92.6 microns. An equilibrium free-stream at atmospheric conditions was used upstream and vacuum conditions were used downstream. Mach and

temperature contours were presented, and a Mach number for the velocity component tangential to the wall at the exit exceeding 0.5 was observed.

Rothe's nozzle (*Rothe, 1971*) was modeled by *Ivanov et al.* (*1997*) with a stagnation pressure of 474 Pa using a parallel, axisymmetric, DSMC code. The calculated density and rotational temperatures agreed with the experimental data. A multizone approach was used where a Navier-Stokes code was used when Bird's breakdown parameter was sufficiently small, the DSMC was used in the transition region, and a test-particle Monte Carlo (TPMC) was used in the free-molecular regime. This multizone approach features optimal computational efficiency as only the necessary computation for each region is performed. This approach was applied (*Ivanov et al., 1997*) to the study of plume interaction with surfaces similar to the ESA's XMM satellite. The calculations showed that 15% of the total thrust of two thrusters is lost due to plume interaction and impingement on the satellite.

The role of surface conditions in DSMC is shown with respect to a free-molecular micro-resistojet (FMMR) by *Ketsdever et al., 1998*. The design utilizes a surface covered by a thin heated film, which is arranged to be the last surface to contact the propellant. Argon was used as the simulation gas for simplicity, though the authors recommended ammonia or water as a propellant for future investigation. The throat diameter was 0.1mm and the wall temperature was kept at 300 or 600 K. The effects of expansion geometry were studied using surfaces with fully diffuse reflection. The specific impulse was studied as a function of surface accommodation

using the Maxwell model and two forms of the Cercignani-Lampis-Lord model. Favorable comparison between DSMC results and free-molecular theory was found.

Spacecraft contamination and the induced environment due to cold-gas attitude control thrusters were studied by *Gatsonis et al.* (*1999*). The Environmental Monitor Package (EMP) spacecraft carried a pressure sensor which collected data from the firings of eight attitude control thrusters. The EMP spacecraft has a 0.56 m diameter base and a length of 0.52 m. The thrusters used produced thrust from 1.2 to 3.3 N with an exit diameter 4.8-5.6 mm and a throat diameter of 0.9-1.6 mm. The flow inside the thrusters had a Knudsen number in the order of 1.5×10^{-6} at the throat (Reynolds number ~ 650,000) and 7×10^{-5} at the exit (Reynolds number 26,000-60,000). As the flow is initially continuous, a Navier-Stokes code was used until the breakdown of the continuty assumption according to Bird's breakdown parameter (*Bird, 1970*). The Navier-Stokes solution then provided input into a three-dimensional, unstructured DSMC code which is used to simulate the rarefied portion of the plume. The grid for the DSMC code was sized to accurately capture the surface geometry and the flow physics. The DSMC results at the location of the pressure sensor entrance were used to determine the presure inside the sensor according to the theory of Hughs and de Leeuw. The simulation results for the pressure sensor chamber pressure showed good agreement with the experimental measurements for the pitch and yaw thrusters. Agreement with the roll thrusters is less good, but it is demonstrated that this is due to lack of knowledge of the exact thruster configuration, as two orders of magnitude difference is observed by slight

(2.5 cm) changes in the radial position in the roll thrusters. This study illustrates the value of unstructured DSMC and Navier-Stokes codes to predict complex flow configuations with transitions from continuous to rarefied flow.

The breakdown of the Navier-Stokes equations and equilibrium in micronozzles was studied numerically by *Ivanov et al.* (1999) using a Navier-Stokes solver (GASP) and the DSMC method. The studied focused on characterizing the performance of nozzles based on the two techniques. A conical helium nozzle was considered with a sharp throat (radius: 27 microns) that diverged at a 15 degree angle to an exit diameter of 81.3 microns. Two stagnation pressures, 10 and 1 atm, were studied at a constant stagnation temperature (297K) to assess the effects of breakdown. GASP used first order extrapolation at the nozzle exit, as is common in nozzle flow modeling (*Ivanov et al., 1999*). The DSMC code featured the majorant cell and free cell schemes, adaptation, different time steps, and radial weighting. These contribute to the efficiency and accuracy of the calculations. The two inlet DSMC boundary conditions on velocity (uniform and Poiseuille profiles) produced similar results. An area slightly outside the nozzle was also modeled with DSMC for accuracy. The DSMC code showed the sonic isoline touching the nozzle lip, while the Navier-Stokes calculation showed it removed from the wall an increasing distance with increasing rarefaction. While properties from both calculations agreed near the nozzle centerline, as equilibrium breaks down near the nozzle lip pressure and Mach contours produced by the different methods diverged. Breakdown of equilibrium occurred further inside the nozzle for the lower chamber pressure case. The Navier-

Stokes prediction for specific impulse were higher than the DSMC ones for both pressures, and for the lower pressure the N-S results showed a specific impulse higher than that of an ideal nozzle. The DSMC results illustrated a decrease in specific impulse for higher expansion ratios for very low Reynolds number nozzle flows. Rothe's nozzle was also studied for Re = 270 and Re = 120. Both simulations compared well with the centerline values of temperature and density found by experiment. The DSMC method compared more favorably to experimental values near the nozzle exit wall. The lower Reynolds number case accentuated this behavior, and additionally illustrated a breakdown of equilibrium of translational and rotational temperature, which the DSMC code accurately predicted and the Navier-Stokes code did not. This study illustrates the importance of outflow boundary conditions and the breakdown of the continuum assumption near the nozzle lip.

The role of the nozzle lip in backflow was studied numerically (*Ivanov and Markelov, 2000*) using the DSMC method with respect to contamination issues associated with micronozzle plumes. Navier-Stokes calculations were also performed for the sake of comparison. It was found that a thick lip (five radii of the nozzle exit) can reduce contamination but not eliminate it altogether. Bird's breakdown parameter along with density and temperature was plotted in the region near the nozzle lip of a bell nozzle previously studied (*Ivanov et al., 1997*). The loss of efficiency when scaling small traditionally machined thrusters to microthrusters is chiefly due to increased viscous boundary losses. In order to reduce these losses, the slip velocity at the wall must be increased. Ivanov and Markelov introduce a fraction

of helium (0.1) into the chamber of Rothe's nitrogen nozzle in order to study the effect. Being a lighter gas, helium is forced to the wall and provides an effective gasdynamic lubrication. Velocity profiles at the exit show that the introduction of helium decreases the boundary layer thickness and provides a higher exit velocity than either nitrogen or helium alone.

Three-dimensional modeling of microthruster flows is still a developing art. The shear magnitude of three-dimensional particle simulation has only been recently accessible with modern high-speed computers. Surface interaction models have not been completely studied either empirically or computationally, and often play an important role in microthruster simulations. Injection conditions and chemical kinetics appropriate to micronozzle flows are other outstanding issues that have only been partially addressed in DSMC modeling. For high temperature flows, vibrational degrees of freedom must also be considered. Many micronozzle geometries, such as planar MEMS micronozzles, result in fully three-dimensional flows that must be modeled appropriately. If spacecraft interaction is to be considered, complex flow geometry must be simulated as well. Gasdynamic modeling of microthrusters useful to engineering applications continues to be investigated and improved as understanding of issues important to micronozzle flows increases.

1.3 Modeling of Plasma Microthrusters

When ionization become important, it is necessary to include electric effects when modeling microthrusters. Plasma modeling performed in the continuum regime utilizes the magnetohydrodynamic equations. As the flows in electric

micropropulsion devices may deviate far from equilibrium and the density level is low, a kinetic description is most appropriate for the treatment of these flows.

The particle-in-cell (PIC) method uses weighted particles to represent a distribution function, similar to the DSMC method for gasdynamics. There are several levels of approximation in PIC, each of which may be used to treat different types of plasma flows. Flows may be modeled as electrostatic and collisionless. The flow may be modeled as electrostatic with collisions included probabilistically, in which case the the simulations are PIC/DSMC models. The flow may also be modeled as electromagnetic (EM-PIC), both with and without collisions. If collisions are included then Boltzmann's equation is stochastically solved; if collisions are neglected then the PIC methodology reproduces Vlasov's equation (*Nanbu, 2000*).

1.3.1 Electrostatic Models

Electrostatic PIC codes are the most widely used and developed, both because of their well-studied computational properties and their application to many problems of engineering interest. Despite the neglect of time-varying magnetic fields, the electrostatic formulation is accurate for most electrically driven flows.

Electrostatic codes are usually based upon a solution to Poisson's equation (*Birdsall, 1991*) but may be also derived from the current balance equation (*Gatsonis and Yin, 1997*a; *Gatsonis and Yin, 1997*b) or Gauss's law for simple geometries. In both the former cases, electrons may be described as fluids through the inclusion of

fluid operators as part of the charge density, making the resulting matrices algebraically non-linear.

A 3-D PIC model was applied to the study of field emission cathodes with respect to application in electric microthrusters (*Marrese et al., 2000*). A planar field emission array was modeled as if attached to a spacecraft surface. The area of the field emitter array was 0.22 cm^2, and the domain was loaded initially with ambient ions and electrons in a Maxwellian distribution. Thermal particles were also injected from the open boundaries, and the field emission cathode array emitted particles in a cold beam. The current density was varied from 34 to 236 mA/cm^2, and at lower values of current density, potential contours closely resembled planar behavior (especially near the center of the array). At higher values, a more spherical sheath is seen.

Several outstanding computational issues exist in electrostatic plasma modeling. Development of arbitrary circuit boundary conditions for three dimensions remains to be done for arbitrary geometries. In partially ionized flows, a methodology for appropriate interaction between neutral and charged particles has been developed (*Nanbu, 2000*) but is not yet widely applied. Appropriate electric flux and particle-surface interaction boundary conditions have not been widely developed. Further development of appropriate boundary condition models and particle collision models is important to accurate electrostatic modeling of micropropulsion devices.

1.3.2 Electromagnetic Models

When the physical problem includes time-varying fields, it becomes necessary to turn to a solution of the full or partial set of Maxwell's equations:

$$\begin{aligned} \nabla \times \mathbf{H} &= \mathbf{J} + \frac{\partial \mathbf{D}}{\partial t} \\ \nabla \times \mathbf{E} &= -\frac{\partial \mathbf{B}}{\partial t} \\ \nabla \bullet \mathbf{B} &= 0 \\ \nabla \bullet \mathbf{D} &= \rho \end{aligned} \tag{1.1}$$

In these equations, **H** is the magnetic field; **J** is the current density; **D** is the electric displacement; **E** is the electric field; **B** is the magnetic-flux density; ρ is the charge density (*Jackson, 1999*). In a linear medium, **D** and **E** are related according to $\mathbf{D}=\varepsilon\mathbf{E}$, and **B** and **H** are related according to $\mathbf{B}=\mu\mathbf{H}$, where ε and μ are the permitivity and permeability of the medium, respectively.

Yee (*1966*) proposed a computational method for electromagnetic wave propagation and scattering on two staggered Cartesian grids. The method is based on the Ampere-Maxwell law and Faraday's law. The magnetic flux density and electric displacement vector are linearly discretized and a leap-frog method is used to advance the fields in time for second-order accuracy. The method is based upon the integral representation of the Maxwell equations and that the edges of one mesh correspond and are orthogonal to the faces of its dual, and vice versa. The fields are updated on a face by taking the sum of contributions from the alternate field along the edges of the face, including contributions of current when updating the magnetic field. This is a

discretized approximation of Stoke's theorem relating the curl of a field normal to a surface to the line integral around the surface.

Yee's lattice method may be generalized in principle to any polyhedral mesh and a suitable dual using the method of discrete surface integrals (*Hermeline, 1993; Madsen, 1995*). The discrete surface integral (DSI) method is based on the duality of edges and faces of two meshes and uses a discrete approximation to Stoke's theorem for the Ampere-Maxwell law and Faraday's law. The DSI method becomes Yee's method on a Cartesian mesh.

Hermeline (*1993*) proposed a method for Maxwell's equations on the Delaunay mesh and its Voronoi dual in two and three spatial dimensions with field components represented in three dimensions. It is shown that there are two separate methods as the electric and magnetic fields may be associated with either mesh. Attention is given to particle and current weighting procedures, which use a combination of piecewise linear functions and the least squares method. Since the piecewise linear charge distribution and current density do not exactly satisfy charge conservation locally, it is desirable to introduce a correction scheme for the electric field based upon deviation from the divergence equation:

$$\nabla\bullet(E-\nabla\varphi)=\frac{\rho}{\varepsilon_o} \tag{1.2}$$

In this equation, φ is the correction potential and ρ is charge density (in coulombs). Since the charge density electric field is known, this leads to a formulation for Poisson's equation:

$$\nabla^2 \varphi = \nabla \bullet \mathbf{E} - \frac{\rho}{\varepsilon_o} \tag{1.3}$$

Once the correction potential is obtained, the gradient of this value is added to the electric field. *Hermeline* (*1993*) also notes that since all that is needed in the DSI formulation is the product of current integrated over the area of the control volume. If this current is obtained using particles (via the PIC method) then the enforcement of the discretized Gauss law remains a consequence of the discretized Ampere's law and it is unnecessary to correct the electric field. However, it is noted that this method provides noisy results. Calculations, with error analysis, are presented for the case of eigenmodes of a square cavity on 2-D Cartesian and unstructured meshes. The error was comparable for the two meshes and in both cases negligible. Radiation from a dipole was also modeled and results of the two methods were similar. A thermal cathode and photo-injector were also modeled in two dimensions.

The discrete surface integral method was presented for non-orthogonal staggered polyhedrons by *Madsen* (*1995*). Previous approaches to electromagnetics in irregular domains, such as stair-stepping Cartesian grids, finite elements, and two finite volume formulations, are reviewed and found inadequate. Madsen presented an algorithm for the finite difference time domain method for non-orthogonal polyhedral grids with a dual constructed through joining the barycenters of primary cells. This led to one-to-one correspondence between nodes, edges, faces, and cells of the primary grid to cells, faces, edges, and nodes of the dual grid. It was noted that solution accuracy degenerates when primary edges and faces do not intersect with

their dual faces and edges. Though electric currents were not taken into account in this paper, their effects could be added in a manner similar to cases for Cartesian grids (*Birdsall and Langdon, 1991*) or the Voronoi-Delaunay dual (*Hermeline, 1993*). The components of a field (for example, **E**) normal to the surface may be updated using an integral around the edges of the face of the complement field (**B** in this example). The field at the nodes may be obtained through a 3x3 system of equations based on the values calculated at the faces of the grid bordering the edge of interest. This leads to several values of the field which are interpolated to the face either by a vector sum average, a partially volume weighted averaged, or a fully volume weighted average. The field obtained at the face due to the updating of its derivative is projected onto the edge to update the complementary field in a similar manner. It was noted that this algorithm is charge conservative. It was also noted that if the grids used are orthogonal, the averaging procedure may be avoided entirely and the algorithm reduces to the general finite-difference time domain technique.

Madsen (*1995*) presented tests and error analysis for the DSI algorithm on distorted grids. In a grid constructed by mapping a square to a circle, it was shown that all methods are conditionally stable. The simple vector sum provided the lowest level of stability and the fully volume weighted method the highest stability. A rectangular wave-guide was modeled with a sinusoidal driving signal using orthogonal and skewed grids composed of hexahedra, tetrahedra, pyramids, and hybrid meshes. This problem was chosen for the availability of an analytic solution. Error in all cases was comparable and the most accurate solution was obtained on

tetrahedral grid derived from the division of skewed hexahedra. Comparison of results for scattering of a Gaussian pulse from a conducting sphere showed that discretization of the sphere into a non-orthogonal surface provides a better comparison to analytic data than a comparable stair-stepped approximation of the sphere. The three-dimensional DSI algorithm also showed favorable comparison to radiation from a dipole on a mostly orthogonal grid. As a final example, a twisted wave-guide was modeled using DSI. The electric field time history for the twisted and straight wave-guides were essentially identical, showing a good validation for the model where no analytic solution is known and methods based on Cartesian grids do not apply.

A three-dimensional EM-PIC method was presented by *Wang, et al.* (*1997*) using a non-orthogonal grid of hexahedral cells and the discrete surface integral method to update the electric and magnetic fields. Particle location was tracked in Cartesian logical space while the velocity was kept in physical coordinates. The code takes advantage of the fact that if charge is rigorously conserved, both globally and locally, then the fields may be updated by the Maxwell curl equations alone. Tri-linear interpolation was used to map logical coordinates to physical coordinates. Current deposit was done in logical space by use of *Villasenor and Buneman's* (*1992*) rigorously conservative algorithm based on area and volume weighting. Particle movement was done using the standard leap-frog technique with the addition of a rotation matrix that maps physical and logical space.

Fields were updated in *Wang, et al.* (*1997*) using the discrete surface integral method for non-orthogonal grids. The fields were found at the vertices from knowledge of their normal components at the three faces within the cell that share the node. Three methods were considered in weighting the results at each node among the cells that share it: simple vector weighting, full volume weighting, and one-sided volume weighting. In one-sided volume weighting, the vector associated with the face is split into two components from the centers of the cells to the center of the face. The components associated with each side of the cell are averaged separately. Once the field components are updated, their values at the vertices are computed using a similar method involving the solution at the three faces of interest for each cell containing the node.

Analysis of error for the EM-PIC method is presented in *Wang, et al.* (*1997*). The particle pusher was accurate as long as grid distortion is not too great due to its dependence on a rotation matrix. EM wave propagation was studied on distorted grids all three weighting schemes studied lead to non-physical instabilities despite the fact the Courant condition is satisfied. The simple vector weighting method was shown to be the most stable and one-sided volume weighting the least. Greater grid distortion increased the growth rate of error. Results on a skewed grid were always numerically stable. Properties of the weak instabilities of the DSI method on non-orthogonal grids were discussed and recommendations given on how to deal with this source of error. Energy conservation was monitored for the unstable configuration of two opposing relativistic electron streams. It was found that error did not exceed 2%

even for highly distorted grids. The EM-PIC code was shown to be highly parallelizable, as only local information must be exchanged.

The finite difference time domain (FDTD) method (Yee's lattice (*1966*) on Cartesian meshes and DSI on general meshes (*Heremline, 1993; Madsen, 1995*) require knowledge of the electric current if free currents are considered in the problem, as is the general case with particle methods. In general, finite difference time domain electromagnetic solutions satisfy the Maxwell divergence equations for electric and magnetic fields if they were satisfied initially and charge is rigorously conserved (*Birdsall and Langdon, 1991*). It was advised that a potential correction based on Poisson's equation be used to ensure conservation of charge in particle methods (*Birdsall and Langdon, 1991*). However, weighting procedures that rigorously conserve charge may allow electromagnetic calculations to be performed without the computational cost of a Poisson solve at every electromagnetic step (*Villasenor and Buneman, 1992; Wang et al., 1997*). If the Poisson correction is not used, the FDTD method is a purely local method -- this has several conceptual and computational advantages.

Villasenor and Buneman (*1992*) developed a rigorous charge conservation scheme for electromagnetic particle simulation methods based on area weighting. The particle was considered a cloud with charge uniformly distributed over the area of a Cartesian cell (a square shaped particle, in 2-D). The formulation was given for two and three dimensions, for an arbitrary number of boundaries being affected by the particle. It was assumed that the computational particle would cross no more than a

single boundary within a time-step, as implied from the Courant condition. It was found that area weighting, identical to that used to weight currents, eliminated self-force during the field-to-particle weighting procedure. The scheme was tested through the assignment of a charge distribution and electric field that satisfied Poisson's equation for electrostatics. It was shown that the magnetic field remained zero, as the electric field was initially curl-free. *Villasenor and Buneman* (*1992*) compared this result to that obtained to the potential correction method used to ensured conservation of charge, and it was found that the two methods agree to within round-off.

Electromagnetic plasma modeling is generally more computationally expensive and not as well developed than electrostatic modeling. Appropriate boundary conditions for circuit elements have been developed with limiting assumptions, but further work is needed. Modeling of arbitrary boundary conditions for electromagnetics is still developing. A charge conserving routine similar to that of *Villasenor and Buneman* (*1992*) has not been developed for arbitrary geometries. In order to accurately model electromagnetic micropropulsion devices, adequate study of appropriate boundary conditions and particle interaction models must be done.

1.4 Objectives and Approach

The goal of this work is to further develop a particle-based code appropriate to the modeling of partially ionized flows with application to micropropulsion devices. Specifically, an unstructured tetrahedral DSMC-PIC code will be developed in order

to characterize and assess the gasdynamic and plasmadynamic effects in micro thrusters. Much of the work for the DSMC kernel and the code of grid generator has been developed through previous efforts (*Kovalev, 2000*). The specific objectives for this work are:

- Development of a simple triangular surface generator to characterize domains of engineering interest for aid in mesh generation.
- Addition of quality assessment and control techniques to the unstructured tetrahedral generator. Higher quality grids lead to greater accuracy and computational efficiency for both particle and field solvers.
- Implementation of techniques to minimize and prevent lost particles encountered in particle movement.
- Addition of the variable hard sphere model for molecular cross-sections. The use of variable hard spheres offers much more accurate characterization of molecules than hard spheres and without much additional computational cost.
- Validation of molecular rotational degrees of freedom and addition of discreet vibrational degrees of freedom. In the continuum regime, it may be assumed that rotational degrees of freedom may be relaxed, but this does not hold as collisions grow more infrequent. Vibrational degrees of freedom are rarely fully excited and must be treated as discrete levels.
- Implementation and validation of an electrostatic solver based on Poisson's equation for electric potential.

- Application of the DSMC code to gaseous microthruster simulations and comparison with experimental and computational results.
- Preliminary application of the unstructured PIC to electrostatic plasmas.

This thesis is organized as follows: in Chapter 2, the grid generator, DSMC, and PIC methodologies and their implementation on unstructured grids are presented. In Chapter 3, the DSMC and PIC simulations are presented. In Chapter 4, the conclusions of the work are outlined along with recommendations for future work.

Chapter 2

DSMC-PIC Methodology, Implementation, and Validation

2.1 Overview

This chapter summarizes the methods used and implemented for the DSMC-PIC solver on unstructured grids. The methodology for grid generation is presented with application to particle modeling. The models for molecular cross-section and internal energy exchange are presented with application to the DSMC solver. A finite-volume electrostatic solver is presented with applications to plasma modeling. Validation examples are presented with the computational methods used to illustrate their accuracy and applicability.

2.2 Unstructured Tetrahedral Grids and Application to DSMC-PIC Modeling

Flows encountered in the study of micropropulsion devices are often three-dimensional. The microthruster may have a geometry that itself gives rise to a three-dimensional flow, such as a planar MEMS nozzle or a rectangular PPT. In the study of plume-spacecraft interaction, the thruster plume may impinge upon the spacecraft in such a way that the flow is three-dimensional. In order to study such flows, a grid methodology must be applied that accurately captures surface geometry.

An unstructured tetrahedral Delaunay mesh generator is utilized in this work in order to satisfy these requirements. The full methodology of the grid generator

used in this work is available in *Kovalev,* (*2000*), where the algorithms are presented in some detail. A surface triangulation of the relevant geometry is used as input to the mesh generator, which produces a Delaunay triangulation of the surface geometry with spacing values that match the input triangulation. Due to the deficiencies of the grid generator by *Kovalev,* (*2000*), meshes were generated with poor grid quality for certain geometries of interest. To correct this, heuristic optimization is implemented in this work to increase grid quality.

In order to generate meshes for engineering use, a mesh generator is utilized based on Watson's algorithm for point insertion (*Watson, 1981*). Watson's algorithm creates a new Delaunay mesh from an existing one by meshing the new node to the facets of the cells whose circumspheres contain the new node, checking that tetrahedra with positive volumes are created. Delaunay triangulations have several properties that make them useful for purposes of mesh generation and scientific computations. A perspective in Delaunay triangulations with respect to bounded mesh generation is available in *Baker,* (*1989*). In the mesh generator used herein and presented by *Kovalev,* (*2000*), the Delaunay triangulation starts with a cube divided into six tetrahedra to generate a background mesh, into which the boundary points are inserted. Constrained edges and faces are then recovered. New points are generated by the exponential division of edges (*Borouchaki and George, 1997*), which generates points with good spacing values for the numerical methods considered here. It is necessary to filter the generated nodes to examine if they are too close to existing nodes.

2.2.1 The Delaunay Triangulation and Voronoi Tessellation

A Delaunay triangulation of a set of points in N dimensions divides the set into simplex elements of $N + 1$ points such that the N circumsphere of each element does not contain points from any other element. In two dimensions the circumcircle of each triangle element contains no other points save its three defining points. Similarly, in three dimensions the circumsphere of each tetrahedron contains no other points save its four defining points. The Delaunay triangulation of a set of points is unique if no set of more than $N + 1$ points lies on the same N circumsphere.

The Voronoi diagram is formed by the set of points (lines in two dimensions, faces in three dimensions) equidistant to a point and its nearest neighbor. The points inside a Voronoi cell are nearer to the node defining the cell than any other.

Examination of the Delaunay triangulation and Voronoi diagram shows that the two are natural duals. In three dimensions, there is a one-to-one correspondence between Delaunay nodes, edges, faces, and cells to Voronoi cells, faces, edges and nodes, respectively. In the case of other dimensions, a similar hierarchy of associations may be found. Edges of one mesh are orthogonal to the face of the other. These properties of the Delaunay triangulation and the Voronoi tessellation make them favorable for computational use.

Construction of Voronoi Dual from the Delaunay Triangulation

The Voronoi mapping is complex in terms of variations in structure from cell to cell. However, the finite volume formulation on the Voronoi mesh is essentially identical in computational efficiency to a standard finite difference scheme – the

coefficient matrix simply has a variable number of coefficients per row depending on the valence of the node. In order to obtain an acceptable level of accuracy, the mesh used must have a high orthogonality (or alternatively, use a more complex formulation with more coefficients) and enforce properties at the boundaries.

The Voronoi mesh is constructed as follows. The circumcenters of each tetrahedral cell are found. The boundaries of the tetrahedral mesh are enforced while preserving important properties of the Voronoi dual. The Voronoi dual of each tetrahedral edge is found and relevant properties (associated area and volume) are determined.

The circumcenters of each cell are found according to the equation for a sphere, which may be uniquely determined from four non-degenerate cells. An example of a two-dimensional Delaunay triangulation and associated Voronoi diagram is shown in Figure 3. Characteristics appropriate to the Delaunay and Voronoi meshes will be illustrated in two-dimensions, as three-dimensional examples cannot be adequately presented in two-dimensional figures.

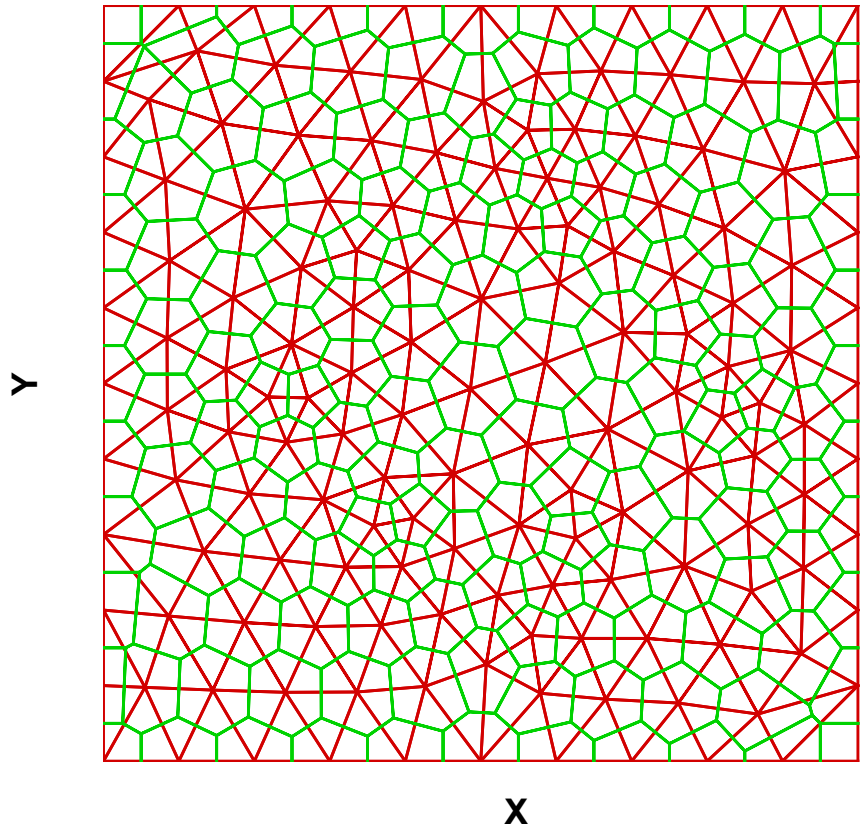

Figure 3. Example of a bounded 2-D Delaunay triangulation (red) and its Voronoi dual (green).

Care must be taken in enforcement of the boundary to preserve the characteristics of the Voronoi mesh. The general methodology is to map any Voronoi node laying outside of its boundary component to its Voronoi equivalent in the next lower geometric dimension. The circumcenters are found for each triangular face that is on the boundary for purposes of electric calculations. If these circumcenters lay outside the face, as for a poorly formed element, they are moved to the nearest edge midpoint, which is the one-dimensional Voronoi equivalent. The orientation of the

circumcenters in boundary tetrahedrons may be determined by the dot product concerning the outward normal of the boundary faces. If the circumcenter is outside the grid, it is moved to the circumcenter of the boundary face (the two-dimensional Voronoi equivalent). The Voronoi dual of a boundary edge (a planar polygon) consists of the edge midpoint, the circumcenter of one of the boundary faces containing the edge, the circumcenter of the tetrahedral cells containing the edge, and the circumcenter of the second boundary face containing the edge. This boundary enforcement scheme preserves the properties of orthogonality and equidistance of Voronoi faces from boundary edge nodes, which are important properties of the Voronoi tessellation for purposes of finite volume accuracy. Complex boundary edges (formed by the intersection of three or more boundary faces) are not treated here algorithmically, but the scheme is essentially the same. It is also noted that these types of boundary surfaces are rare for engineering applications and usually may be avoided without any loss of important geometric information.

2.2.2 Surface Grid Generation

In general, boundary conditions must be applied at surfaces defining the domain. Surfaces may also be specified internal to a flow in order to apply boundary conditions there. For neutral particles, surfaces may serve the role as exhausting particles into vacuum, injection of new particles from a prescribed distribution, or a material boundary that interacts to rebound or absorb the incident particle. For charged particles, a surface may be a conductor or a free boundary, or have the

normal component of electric field applied. Details on the implementation of boundary conditions for the charged particle case are given in section 2.6.

Triangulation of the surfaces of the domain is the first step in generation of a tetrahedral grid using Watson's algorithm. Triangulation of the surface may be done analytically for simple surfaces, or using mesh generation techniques for more complicated surfaces.

A simple surface generation scheme was developed with respect to issues of particle modeling. The surface generator constructs triangulations of axial and box-like domains according to user-specified spacing.

Surface Generator Implementation

A surface generator was written for axially symmetric objects and box-like objects (objects that are definable by bi-linear elements). From the definition of control points suitably connected by lines, arcs, or upward downward facing parabolas and appropriate spacing values at these points, a two-dimensional topology may be made (also useful for two-dimensional grid generation) according to the spacing value with edges having an attribute specified by connection. Assuming appropriate spacing values, this topology may be tiled about an axis analytically to create a high-quality axisymmetric surface. For bi-linear surfaces, only the first two edges of a bi-linear element may be created with arbitrary spacing values. The spacing values for the second two edges of an element are inferred from the requirement that the opposing edges have the same number of nodes. Care must be

taken in selection of spacing values as well as creation order of bi-linear elements and objects to ensure a high quality triangulation. After axially symmetric or bi-linear objects are created, they may be rotated and added to a group of objects, if the simulation domain includes multiple objects. If the object is represents an internal boundary, a virus point (see *Kovalev, 2000* for definition) must be included that lies within the object's interior. An object or group of objects may be output to a file that is used by the grid generator.

It is possible to triangulate many other surfaces of engineering interest, as well as to triangulate surfaces using Watson's algorithm, with respect to an analytic definition of the surface or sharp edges. There are also several commercial CAD programs that contain this feature.

2.2.3 Grid Quality Issues for DSMC and PIC Modeling

The role of the grid in particle modeling is to provide discrete cells of physical space for selection of collision partners and sampling purposes. For unstructured grids, particle movement involves complex calculations to determine the intersection point of the particle at the face. In order to generate acceptable results, the effect of grid quality should be considered in the context of stochastic particle modeling.

As long as the longest cell dimension is less than the local mean free length (the smallest mean free path, or length of where gradients of macroscopic quantities may be treated as linear), the sampling and collisional procedures should not suffer as long as enough particles are included in the cell to accurately represent the

distribution. In practice, it is desirable to have a high quality grid in all cases, as low quality grids will have more cells and faces than high quality grids and require subsequently more computational time for the same physical problem. Poor quality grids are more computationally expensive, as there will be more cells for given spacing values with corresponding lower volumes. More particles must therefore be used to obtain an accurate representation of velocity space in each cell. Also, sampling and collisional procedures may suffer in accuracy from grid biases on poor quality grids. The particle movement routine may break down as cell quality worsens, and the issue of losing particles becomes important on grids of questionable quality.

Several algorithmic procedures were added to monitor and delete lost particles. It was observed that cells with poor dihedral angles were primarily responsible for loss of the particles. Elimination of these cells, by quality grid generation or cell removal if the cell was on a boundary, proved to minimize or even eliminate lost particles entirely. Care must be taken when removing boundary cells to ensure boundary conditions and flow physics are satisfied.

Implementation of Heuristic Optimization for Unstructured Tetrahedral Grid Generation

Mesh generation diagnostics showed that the cells where particles were lost had poor quality minimal dihedral angles and solid angles. Examination of the poor-quality elements showed them to be known types of "slivers" (*Cheng et al., 2000*).

It is provable that for a decent-quality surface triangulation, it is possible to generate a conformal Delaunay mesh of high quality (*Li, 2000*). A simple optimization method was used in this work which improved quality of the triangulation to the extent that it proved good for the particle and field computations of interest. More robust optimization methods (*Li, 2000; Cheng et al., 2000*) could be implemented if the existing method proved to be inadequate for computations.

The minimum allowable dihedral angle is defined by a user in an input file. Typically, only the cells with the lowest minimum dihedral angles cause computationally invalid results. Nodes are generated according to the exponential spacing technique of *Borouchaki and George* (*1997*). The nodes are filtered to see if they are too close to other nodes, according to the local spacing criteria. The remaining nodes are checked to see if they improve mesh quality according to the minimum dihedral angle. If they do not, and their minimum dihedral angle lies under the user defined minimum, they are not inserted into the mesh. Care must be taken in selection of the minimal value, as selecting too high of an allowable minimum dihedral angle may result in a mesh with poor spacing criteria.

Figure 4 illustrates a cross-section of a closed rectangular geometry with the optimization method applied. The interior triangles shown in the cross-section all have good quality, visually illustrating the effectiveness of the method. In Figure 5, the distribution of minimum dihedral angle in a cell is shown versus number of cells for the same rectangular geometry with and without optimization. The minimum cut-off angle for the optimized case was chosen to be 0.3 rad. The presence of fewer

cells in the optimized case is due to more efficient tessellation of the domain. In Figure 6, the normalized distribution function of minimum dihedral angle in a cell is shown for the Gravity Probe-B thruster surface triangulation. Both optimized and non-optimized cases are shown, with the minimum cut-off angle for the optimized case being 0.3 rad. The optimized curve has significantly fewer low minimal dihedral angles and a greater amount of higher quality dihedral angles.

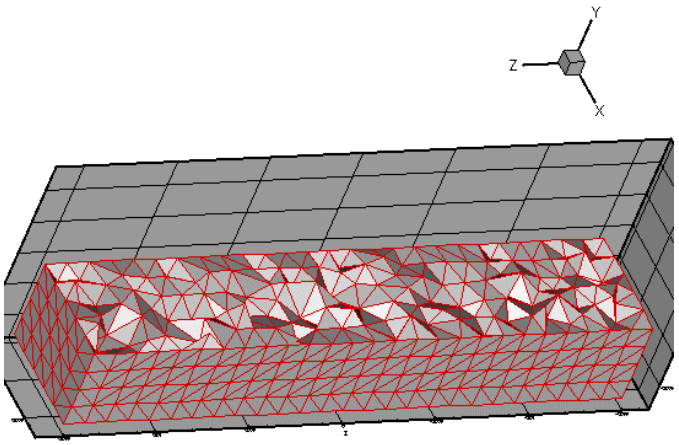

Figure 4. Cross-section of mesh for a closed rectangular geometry using a cut-off dihedral angle of 0.3 rad.

Implementation of the heuristic optimization method proved to vastly reduce the number of lost particles. In all cases presented in this work, less than one percent of the mass flow rate of particles is lost, and in many cases no particles are lost. Heuristic mesh optimization such as presented here is adequate for many numerical methods so long as the computational routines used are written for general geometries such that only round-off error and local grid biases contribute to computational error.

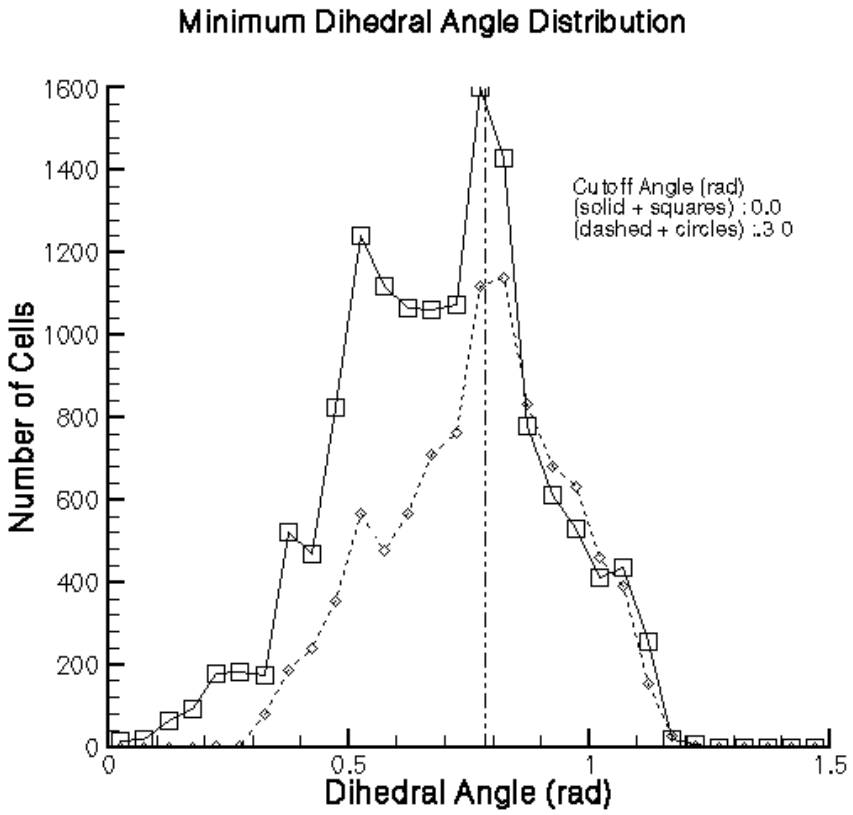

Figure 5. Effect of choosing a cut-off dihedral angle (0.30) on the dihedral angle distribution.

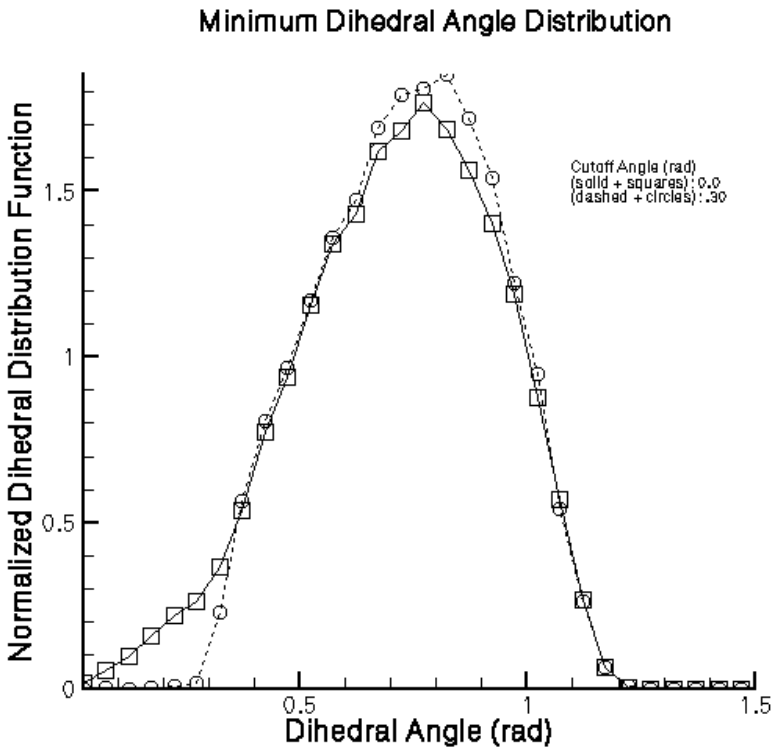

Figure 6. Normalized minimum dihedral distribution for the Gravity Probe-B surface triangulation with zero cutoff angle and a cutoff angle of 0.30 rad.

2.3 Gasdynamics via Direct Simulation Monte Carlo

2.3.1 Overview of DSMC Methodology

The Direct Simulation Monte Carlo (DSMC) method stochastically models dilute gases through the uncoupling of movement and collisional processes. A number of particles are alternatively moved and sampled for collisions. Collisional procedures are based upon the molecular cross section of each species included and the fact each computational molecule represents a large number of real molecules. The fundamental assumption of DSMC is that the time between collisions is much

greater than the duration of collisions, a condition applicable to gases of low to moderate densities.

Most DSMC implementations divide the domain of interest into cells for purposes of selection of collisional partners and flow-field sampling. This is done for computational efficiency and convenience. The cell size should be less than the mean free path of the gas as well as small enough to capture the physics of the flow-field. A sufficient number of particles must be present in each cell to accurately characterize the velocity distribution function. On average, a particle should not cross a whole cell during the time step so that it has a chance to collide with physically valid collision partners.

The no time counter scheme (*Bird, 1998*) is used for collisional sampling. The total number of collisions N_{pq}, per unit time per unit volume between molecules of species p and q, is:

$$N_{pq} = n_p n_q \left\langle \sigma_{Tpq} g_{pq} \right\rangle \tag{2.1}$$

where n_p and n_q are the number densities of species p and q, σ_{Tpq} denotes the total cross-section, and g_{pq} is the relative speed. The average value is obtained by integration over the velocity distribution function.

However, evaluation of the average of the product of relative speed and collisional cross-section requires calculations of the order of the number of particles per cell squared. The no time counter methodology greatly reduces the computational load by taking advantage of the probabilistic acceptance-rejection procedure. The no time counter scheme is such that

$$N_{pairs} = \frac{1}{2V_c} N_p N_q F_N \Delta t \left\{ \left(\sigma_T g \right)_{MAX} \right\}_{pq}$$

(2.2)

where N_{pairs} pairs are selected from the cell for consideration to be collided. In Eq. (2.2), V_c is the volume of the cell, N_p and N_q are the number of computational particles in the cell, Δt is the time step, and F_N is the particle weight. These pairs are chosen at random from the particles in the cell and the collision probability P of a chosen pair is evaluated as

$$P = \frac{\sigma_T g}{\left\{ \left(\sigma_T g \right)_{MAX} \right\}_{pq}}$$

(2.3)

Each sampled pair is checked for collision using the acceptance-rejection method. It is most efficient if the maximum probability of collision is almost one. In this case, only one random number must be used to determine if the pair of molecules collide or not. A random fraction is chosen from zero to one, and if it is less than the collision probability of Eq. (2.3) for the chosen pair, the collision occurs. Otherwise, the collision is rejected. The colliding particles are scattered according to the appropriate molecular cross-section model.

The DSMC code has also been modified to include the effects of internal energies, chemical reactions, radiation, and other collisional events important to low-density gasdynamics (*Bird, 1998*). The DSMC method makes no assumptions other than those already implied by the Boltzmann equation (*Nanbu, 2000*). Being a

stochastic method, DSMC may produce noisy results as the number of particles used is typically far fewer than the number of actual molecules.

2.3.2 Neutral Particle Loading

Particle loading is the first procedure in the process of a DSMC simulation. The cells are to be populated according to the local density number and particle weight. From a computational point of view it is more convenient to set initially the total number of computational particles. In this case, the particle weight can be calculated by integration throughout computational domain

$$F_s = \frac{\int_V n_s(\mathbf{r})\mathrm{d}V}{N_s} \tag{2.4}$$

where F_s is the particles weight of species s, N_s is the total number of computational particles and n_s is density number of real atoms or molecules of gas. Usually the numerical value of particle weight is very high, and N_s is very small in comparison with number of real gas molecules in the gas system to be modeled. Each particle is characterized by its position vector $\mathbf{r}$ and velocity $\mathbf{v}$.

It is assumed that the distribution of particles inside each cell is uniform and the number of computational particles inside the cell is calculated in accordance to the volume of the cell and total particle weight. Particles are randomly distributed within a cell with initial velocities based on the assumption of thermal equilibrium and independence of particle velocity components. Therefore, the distribution function for one component of thermal velocity is

$$f_u = \frac{\beta}{\sqrt{\pi}} \exp\left(-\beta^2 u^2\right) \tag{2.5}$$

where $\beta = \sqrt{\frac{m}{2kT}}$. Due to the independence of the velocity components, the distribution function that describes u, v, and w is a product of type (2.5) functions as given by

$$f_o = \frac{\beta^3}{\pi^{\frac{3}{2}}} \exp\left(-\beta^2 \left(u^2 + v^2 + w^2\right)\right) \tag{2.6}$$

Sampling from the Maxwellian follows standard procedures described by *Bird* (*1994*).

2.3.3 Neutral Particle Injection

The injection boundary condition is an important part of the DSMC methodology. It allows a free-stream to enter the domain with prescribed conditions (herein, from a drifting Maxwellian distribution). The injection boundary condition is useful in modeling external flows of a body moving relative to the gas velocity or in modeling internal flows such as a nozzle where gas is injected into the system from near equilibrium conditions.

The number of particles to be adding into the simulation can be evaluated based on analysis of molecular flux across a surface element. Without loss of generality, we can choose such a coordinate system where two of coordinate axes are in the injection plane. A coordinate system is chosen in such a way when the surface element lies in yz-plane, and mean flow velocity of injected particles is in xy-plane.

The inward number flux $\dot{N}$ can be defined by integration of the velocity distribution function

$$\dot{N}_s = n_s \int_{-\infty}^{+\infty} \int_{-\infty}^{+\infty} \int_{0}^{+\infty} uf \, \mathrm{d}u\mathrm{d}v\mathrm{d}w \tag{2.7}$$

In this coordinate system, particle velocity can be expressed in terms of a mean flow velocity $\mathbf{c}_0$ and a thermal molecular velocity *(u', v', w')*.

$$\begin{aligned} u &= u' + c_0 \cos(\theta) \\ v &= v' + c_0 \sin(\theta) \\ w &= w' \end{aligned} \tag{2.8}$$

Equation (2.7) can be rewritten as

$$\dot{N}_s = n_s \frac{\beta^3}{\pi^{3/2}} \int_{-\infty}^{+\infty} \int_{-\infty}^{+\infty} \int_{-c_0\cos(\theta)}^{+\infty} \left(u' + c_0\cos(\theta)\right) \exp\left(-\beta^2\left(u'^2 + v'^2 + w'^2\right)\right) \mathrm{d}u\mathrm{d}v\mathrm{d}w \tag{2.9}$$

After integration, this expression becomes (*Bird, 1998*)

$$\dot{N}_s = \frac{n_s}{2\beta\sqrt{\pi}} \left(\exp\left(-s^2\cos^2(\theta)\right) + \sqrt{\pi} s \cos(\theta)\left\{1 + \mathrm{erf}\left(s\cos(\theta)\right)\right\}\right) \tag{2.10}$$

erf denotes the error function. The molecular speed ratio *s* is given by

$$s = c_0\beta = \frac{c_o}{\sqrt{2RT}} \tag{2.11}$$

The value of $\dot{N}_s$ can be interpreted as number of gas molecules of the species of interest crossing a unit area surface element per unit time with mean flow velocity $\mathbf{c}_0$. The number of computational particles to be added ΔN_s during a time Δt is given by

$$\Delta N_s = \frac{\dot{N}_s}{F_s} S \Delta t \tag{2.12}$$

where F_s is the particle weight and S is the area of the surface element.

While the number of new computational particles is known, each particle must be characterized by position and velocity vectors. The position vector can be easily generated if we assume uniform distribution over surface element. The velocity vectors are distributed according to

$$f \propto \left(u' + c_0\cos(\theta)\right)\exp\left(-\beta^2 u'^2\right) \tag{2.13}$$

To apply the acceptance-rejection method to this distribution, it is necessary to obtain the maximum value by evaluating

$$\frac{\partial f}{\partial u'} \propto \exp\left(-\beta^2 u'^2\right)\left[1 - 2\beta^2 u'\left(u' + c_0\cos(\theta)\right)\right] = 0 \tag{2.14}$$

The most probable thermal speed, which corresponds to the maximum value of the distribution function can be found as solution of the quadratic equation

$$1 - 2\beta^2 u'\left(u' + c_0\cos(\theta)\right) = 0 \tag{2.15}$$

The above has two solutions

$$u' = \frac{-\beta^2 c_0\cos(\theta) \pm \beta\sqrt{\beta^2 c_0^2\cos^2(\theta) + 2}}{2\beta^2} \tag{2.16}$$

Due to the choice of coordinate system, u' must be greater than zero and therefore the solution may be written as

$$u' = \frac{\sqrt{c_0^2\cos^2(\theta) + 2/\beta^2} - c_0\cos(\theta)}{2} \tag{2.17}$$

Taking into account the last expression, the ratio of probability to the maximum probability used in the acceptance-rejection method is given by

$$\frac{P}{P_{max}} = \frac{2\left(u' + c_0\, cos(\theta)\right)}{\sqrt{c_0^2\cos^2(\theta) + 2/\beta^2} - c_0\cos(\theta)} \times \\ \times \exp\left(\frac{1}{2} + \frac{\beta^2 c_0\cos(\theta)}{2}\left(c_0\cos(\theta) - \sqrt{c_0^2\cos^2(\theta) + 2/\beta^2}\right) - \beta^2 u'^2\right) \tag{2.18}$$

The *v'* and *w'* velocity components are generated following the same procedure that was used for particle loading.

2.3.4 Collisional Methodology

Hard Sphere Model

Though molecular interactions often depend on complex quantum mechanical considerations, it is convenient to treat them through consideration of a phenomenological collisional cross section defined by their interaction potential. In general, neutral molecules exert collisional forces by spherically symmetric fields which are weakly attractive at large distances and strongly repulsive at short distances. Classical kinetic theory generally assumes hard sphere or Maxwell molecules for ease of calculation and since real gases exhibit behavior between these limits. The hard sphere molecular model assumes molecules of a constant size with scattering determined through the mechanics of two hard spheres colliding. However, the hard sphere model does not accurately characterize molecular interaction. Highly accurate models, such as the Lennard-Jones potential model ($\phi = \frac{\kappa}{(\eta-1)r^{\eta-1}} - \frac{\kappa'}{(\eta'-1)r^{\eta'-1}}$ [from *Bird, 1998*]), the Sutherland model (which adds an inverse power attractive potential to the hard sphere model), and inverse power

law may be applied to the DSMC method. However, these methods are generally more computationally intensive than hard spheres. It is desirable to use a method that is both computationally efficient and accurately reproduces the behavior of real gases. In the hard sphere molecular model, all real molecules and atoms are presented as rigid spheres with a symmetric force field specified by its radii and masses. While mass of the computational particle directly corresponds to mass of the real particle, the radius of the computational particle represents the characteristic length of the interaction force between real gas particles.

In elastic binary collisions as shown in Figure 7, the kinetic energy and momentum of the pair of particles must be conserved:

$$\begin{aligned} m_1 v_1^2 + m_2 v_2^2 &= m_1 \left(v_1^*\right)^2 + m_2 \left(v_2^*\right)^2 \\ m_1 \mathbf{v}_1 + m_2 \mathbf{v}_2 &= m_1 \mathbf{v}_1^* + m_2 \mathbf{v}_2^* \end{aligned} \tag{2.19}$$

The subscripts *1* and *2* denote the particle numbers and *m* and **v** are mass and velocity of corresponding particle. Post-collision values of velocities are marked by superscript *. It is convenient to describe collision process in the center of mass system of reference moving with velocity

$$\mathbf{v}_{cm} = \frac{m_1 \mathbf{v}_1 + m_2 \mathbf{v}_2}{m_1 + m_2} \tag{2.20}$$

Particle velocities in this frame of reference are

$$\begin{aligned} \mathbf{v}_1 &= \mathbf{v}_{cm} + \frac{m_2}{m_1 + m_2} \mathbf{g} \\ \mathbf{v}_2 &= \mathbf{v}_{cm} - \frac{m_1}{m_1 + m_2} \mathbf{g} \end{aligned} \tag{2.21}$$

where $\mathbf{g} = \mathbf{v}_1 - \mathbf{v}_2$ is the relative velocity.

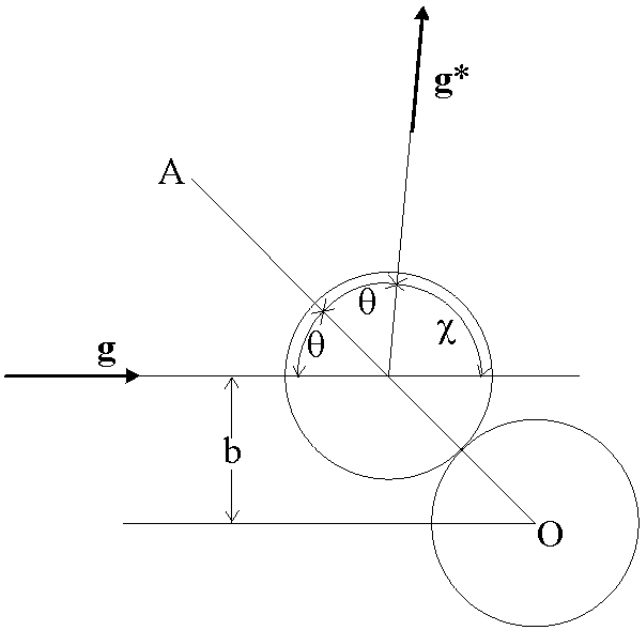

Figure 7. Interaction of Hard Sphere Molecules (from *Bird, 1998*)

It is convenient to evaluate the post-collision relative velocity in a coordinate system (x', y', z') where x' is in the direction of the pre-collision relative velocity **g**. The components of the post-collision relative velocity **g*** are given as

$$\begin{aligned} g^*_{x'} &= g\cos(\chi) \\ g^*_{y'} &= g\sin(\chi)\cos(\varepsilon) \\ g^*_{z'} &= g\sin(\chi)\sin(\varepsilon) \end{aligned} \tag{2.22}$$

where χ is the scattering angle and ε is the angle between the plane of collisions (where the pre-collisional and post-collisional relative velocities lie) and the x-y plane. Transformation into the initial system of coordinates (x, y, z) gives the components as

$$
\begin{aligned}
g_x^* &= g_x\cos(\chi) + \sin(\chi)\sin(\varepsilon)\sqrt{g_y^2 + g_z^2} \\
g_y^* &= g_y\cos(\chi) + \sin(\chi)\left(gg_z\cos(\varepsilon) - g_x g_y\right)\Big/\sqrt{g_y^2 + g_z^2} \\
g_z^* &= g_z\cos(\chi) - \sin(\chi)\left(gg_z\cos(\varepsilon) - g_x g_y\right)\Big/\sqrt{g_y^2 + g_z^2}
\end{aligned}
\tag{2.23}
$$

Finally, the pair of the post-collision velocities is given by

$$
\begin{aligned}
\mathbf{v}_1^{\,*} &= \mathbf{v}_{cm} + \frac{m_2}{m_1 + m_2}\mathbf{g}^* \\
\mathbf{v}_2^{\,*} &= \mathbf{v}_{cm} - \frac{m_1}{m_1 + m_2}\mathbf{g}^*
\end{aligned}
\tag{2.24}
$$

The collisional process is expressed in terms of a differential collisional cross section σ and a total collisional cross-section $\sigma_{\mathrm{T}pq}$, where subscript p and q denote particular species. The collision cross section is an atom specific quantity and is a function only of the kind of interaction potential involved in the collision and the relative particle speed. If one considers the situation where there are n_1 molecules per unit volume with velocity $\mathbf{v}_1$ and n_2 molecules per unit volume with velocity $\mathbf{v}_2$. Consider collisions between molecules of these two classes for which the relative velocity $\mathbf{g}^*$ after collision lies in the solid angle $\mathrm{d}\Omega$ centered about the direction specified by the angles χ and ε. The differential cross section σ_{pq} is defined such that the number of collisions per unit volume of the above type pre unit time is $n_1 n_2 \sigma_{pq} g d\Omega$. The cross-section has dimensions of area and is proportional to the probability that a collision at a relative speed g will result in a deflection χ. The differential cross-section is given by

$$\sigma_{pq} = \frac{b}{\sin(\chi)}\left|\frac{\partial b}{\partial \chi}\right| \tag{2.25}$$

If the molecules are represented as elastic spheres of diameter d, the angle of incidence is equal to the angle of reflection and the impact angle θ is related to χ as

$$\theta = \frac{1}{2}(\pi - \chi) \tag{2.26}$$

The impact parameter is given by

$$b = d\sin(\theta) = d\cos(1/2\,\chi) \tag{2.27}$$

and

$$\left|\frac{\partial b}{\partial \chi}\right| = 1/2\, d\sin\left(1/2\,\chi\right) \tag{2.28}$$

The differential cross-section is then (*Bird, 1998*):

$$\sigma_{pq} = \frac{d^2}{4} \tag{2.29}$$

For the case of species with different diameters, it is necessary to replace d by d_{12} where

$$d_{12} = \frac{1}{2}(d_1 + d_2) \tag{2.30}$$

The total cross-section may be obtained by integration of the differential cross-section over all solid angles. Since the interaction potential is spherically symmetric, this becomes:

$$\sigma_T = 2\pi\int_0^{\pi}\sigma_{pq}\sin\chi\, d\chi \tag{2.31}$$

Integrating, the total cross-section becomes (*Bird, 1998*)

$$\sigma_{Tpq} = \pi d_{12}^2 . \tag{2.32}$$

Similarly, a momentum transfer (or diffusion) cross-section may be defined:

$$\sigma_M = 2\pi \int_0^{\pi} \sigma_{pq}(1-\cos\chi)\sin\chi d\chi \tag{2.33}$$

Integration reveals that for the hard sphere model, the momentum transfer cross-section is the same as the total cross-section:

$$\sigma_{Mpq} = \sigma_{Tpq} = \pi d_{12}^2 \tag{2.34}$$

The total cross-section may be used to determine the number of collisions in a cell and for the probabilistic selection of collision partners in the no time counter methodology. Since the differential and total cross-sections are independent of scattering angle, the post-collision value of relative velocity is isotropic with respect to the center of mass frame of reference. That is, all directions are equally likely for $\mathbf{g}^*$. If a pair is selected to undergo a collision using the no-time counter methodology, the direction of the post-collision relative velocity is selected randomly. The velocities of each of the particles are then updated with respect to conservation of momentum and energy for the pair of particles using Equation (2.24).

Variable Hard Sphere Model

Bird (*1980*) proposed a model in which molecular scattering is performed identically to the hard sphere model, but the diameter of the molecule involved varies according to an exponent which may be set in order to attempt to match the

collisional behavior of real gases. This is the variable hard sphere model (VHS) and the diameter of a molecule of interest is given by:

$$d = d_{ref}(\frac{g_{ref}}{g})^{v} \tag{2.35}$$

where d_{ref} and g_{ref} are reference values chosen to provide the appropriate interaction potential based on empirical data and v is the VHS exponent, also chosen to best match the interaction potential of known empirical data. The general behavior of VHS diameter as a function of temperature can be seen in Figure 8 for nitrogen.

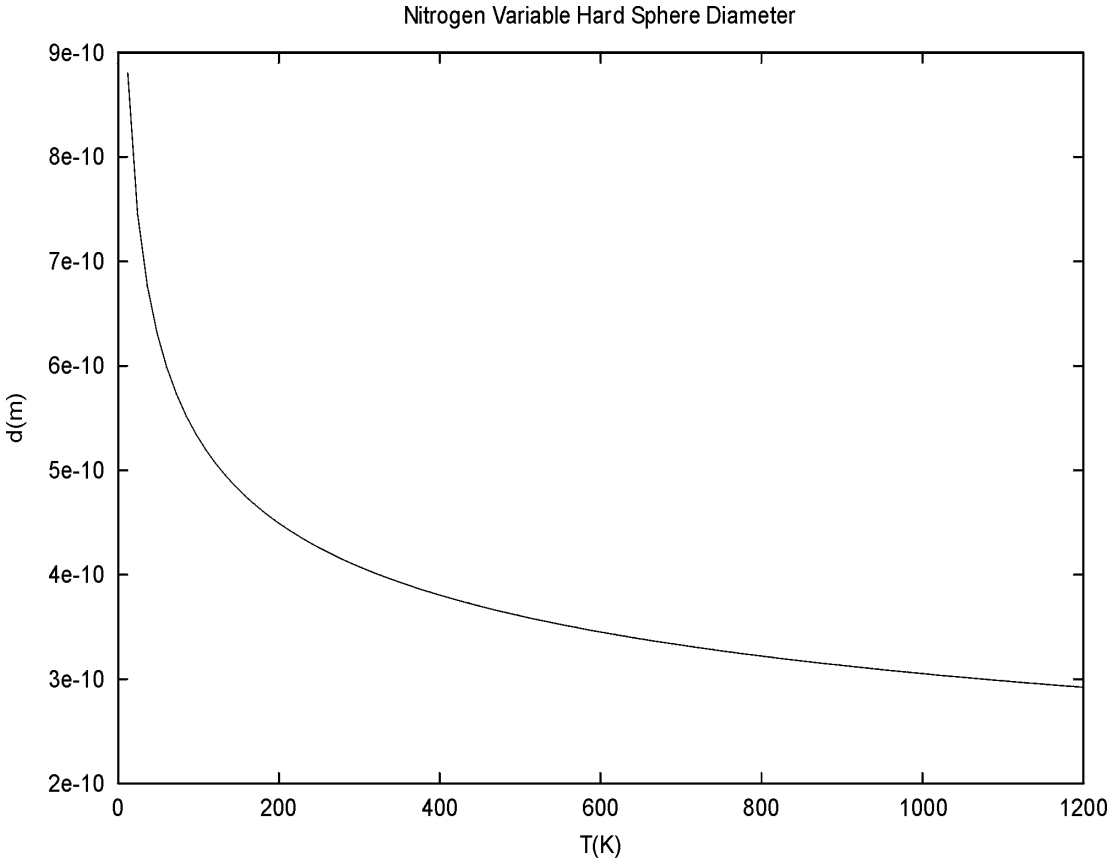

Figure 8. Variable hard sphere diameter for nitrogen gas molecules with mean relative speed as a function of temperature (v=0.24).

The cross-sections for molecular interaction are determined as one would for hard spheres, as is the scattering angle. The total cross section (Eq. (2.31)) and the momentum transfer cross section (Eq. (2.33)) for interaction between molecules *1* and *2* are identical, as in the hard sphere case and given by

$$\sigma_T = \sigma_M = \pi {d_{12}}^2 = \frac{\pi}{4}\left(d_{1,ref} \cdot \left(\frac{g_{1,ref}}{g} \right)^{\nu_1} + d_{2,ref} \cdot \left(\frac{g_{2,ref}}{g} \right)^{\nu_2} \right)^2 \tag{2.36}$$

In order to sample collisions in the no time counter scheme, the product of the total cross-section and the relative speed of the potential collision pair is needed. For the VHS model, the appropriate expression is:

$$(\sigma_T g) = \pi g {d_{12}}^2 = \frac{\pi}{4}\left(d_{1,ref} \frac{{g_{1,ref}}^{\nu_1}}{g^{\nu_1 - 0.5}} + d_{2,ref} \frac{{g_{2,ref}}^{\nu_2}}{g^{\nu_2 - 0.5}} \right)^2 \tag{2.37}$$

$$(\sigma_T g) = \frac{\pi}{4}\left(g^{0.5-\nu_1}(d_{1,ref} {g_{1,ref}}^{\nu_1}) + g^{0.5-\nu_2}(d_{2,ref} {g_{2,ref}}^{\nu_2}) \right)^2 \tag{2.38}$$

2.3.5 Internal Degrees of Freedom

For monatomic gases, the energy of the molecule is purely translational, except at very high temperatures when the electronic energies must be considered. For diatomic or polyatomic molecules, the effects of rotational and vibrational energies must also be considered. While a detailed treatment of energy transfer between internal degrees of freedom is a problem of quantum mechanics, a phenomenological description may be developed that is computationally efficient and accurate for engineering purposes.

Quantum mechanics expresses the energy in discrete energy levels. Sensible energy is measured above the ground state, which all particles would reach at absolute zero (ignoring quantum fluctuations). If the energy levels are closely spaced in the regime of interest (i.e. if the characteristic temperature of level transition is sufficiently low compared to the energies of interest) then energy may be treated as a continuum. If energy levels are widely spaced in the regime of interest then this must be taken into account.

Larsen-Borgnakke Model

The Larsen-Borgnakke model (*Borgnakke and Larsen, 1975*; *Bird, 1980; Bird, 1998*) is a phenomenological model for the exchange of internal and translational energies of a gas molecule. In the Larsen-Borgnakke model, a fraction of the collisions are regarded as completely inelastic and new values of internal and translational energies are sampled from a distribution based upon the effective temperature of the collision. The fraction of inelastic collisions is known for gases from relaxation rates.

Rotational Degrees of Freedom in a Gas Mixture

Gases in general have characteristic temperatures of rotation near absolute zero. When the overall temperature is much higher than this, as is the case in near-field plumes where collisional effects dominate, the rotational levels are very closely spaced and may be regarded as continuous (classical treatment). The Larsen-Borganakke model redistributes energy between different energy modes (rotational,

translation, etc.) from a Maxwellian distribution based on the effective temperature of the collision.

Consider a collision between molecules of type 1 and type 2. Following the notation of *Bird* (*1998*), let Ξ denote the average number of degrees of freedom in a collision. Ξ_a and Ξ_b denote one group of degrees of freedom with energy to be distributed and the remainder of the degrees of freedom for a particular collision, respectively. E_a represents energy to be assigned to the first group of modes and E_b the energy to be assigned to the remaining modes. The Larsen-Borgnakke result for the distribution of energy between the two groups is (*Bird, 1998*)

$$f\left(\frac{E_a}{E_a+E_b}\right)=f\left(\frac{E_b}{E_a+E_b}\right)=\frac{\Gamma(\Xi_a+\Xi_b)}{\Gamma(\Xi_a)\Gamma(\Xi_b)}\left(\frac{E_a}{E_a+E_b}\right)^{\Xi_a-1}\left(\frac{E_b}{E_a+E_b}\right)^{\Xi_b-1} \quad (2.39)$$

where f is the distribution function of the appropriate quantity and Γ is the gamma function,

$$\Gamma(j)=\int_0^\infty x^{j-1}\exp(-x)dx\,. \quad (2.40)$$

Since the sum of the total energy in the collision is constant, it can be shown that the average value of E_a is

$$E_{a(average)}=\frac{\Xi_a}{\Xi_a+\Xi_b}(E_a+E_b) \quad (2.41)$$

This shows that the Larsen-Borgnakke model leads to equipartition of energy (*Bird, 1998*).

For the special case of a mode with two degrees of freedom, $\Xi_a=1$ and the expression for the distribution of E_a:

$$f\left(\frac{E_a}{E_a + E_b}\right) = \Xi_b \left(1 - \frac{E_a}{E_a + E_b}\right)^{\Xi_b - 1} \tag{2.42}$$

It can be shown (*Bird, 1998*) that for the two degrees of freedom case, this distribution may be sampled using

$$\frac{E_a}{E_a + E_b} = 1 - R_f^{1/\Xi_b} \tag{2.43}$$

In this equation, R_f denotes a random fraction from zero to unity. If energy for a number of degrees of freedom other than two is up for redistribution, then the acceptance-rejection method must be used to find an appropriate value (*Bird, 1998*).

The Larsen-Borgnakke method, while completely phenomenological, has several strengths that lend to its usefulness for engineering computations. Energy is conserved and equipartition of energy is preserved on average. The method is based on the effective temperature of the collision, precluding any bias from local flow conditions. The Larsen-Borgnakke method allows arbitrary groups of energy to be redistributed, which may be taken advantage of in serial redistribution of molecular degrees of freedom.

Harmonic Oscillator Model for Vibrational Energy Exchange

Gases usually have characteristic vibrational temperatures in excess of 1000K, so vibrational levels cannot be considered closely spaced. In addition, as the temperature becomes higher, dissociative and ionization effects become important as well. In general, detailed modeling of vibrational degrees of freedom involves energy transfer between translational and rotational modes to the vibrational mode of

interest. For most engineering applications, the above approach is unnecessary unless there is sufficient non-equilibrium to warrant the detailed treatment.

The Larsen-Borgnakke model may be extended to be applicable to discrete energy levels suitable for modeling vibrational energy transfer. Vibrational energy levels are generally anharmonic, as the space between energy levels becomes smaller as energies become larger. If it is necessary to model the anharmonic nature of vibrational energy levels along with dissociation, a scheme presented in *Bird, 1998* may be used.

Vibrational energy levels are often modeled as harmonic oscillators with evenly space discrete energy levels. The harmonic oscillator approximation is good if only the first several vibrational energy levels are of interest and the effective temperature of the molecular collision is typically far beneath the characteristic temperature of dissociation (usually in excess of 30,000 K).

Bergemann and Boyd (*1993*) developed a computationally efficient form of the Larsen-Borgnakke model for vibrational energy exchange using the discrete harmonic oscillator approximation. The equilibrium energy distribution for harmonic oscillator vibrational energy levels i in a gas is

$$f_{vib}(E_{vib}, i) = \frac{1}{kT}[1 - \exp(-\frac{\Theta}{T})]\exp(-\frac{E_{vib}}{kT})\delta(E_{vib} - ik\Theta); i = 0..\infty \qquad (2.44)$$

where δ is the Dirac delta function and E_{vib} is the vibrational energy. The characteristic temperature of vibration is

$$\Theta_{vib} = \frac{h\nu}{k}, \qquad (2.45)$$

where v is the characteristic frequency of the oscillator and h is Planck's constant. The energy of level i of a particular mode is

$$E_{vib,i} = ik\Theta_{vib} \tag{2.46}$$

Since the Larsen-Borgnakke model allows the serial redistribution of energy from multiple groups, vibrational energy redistribution may be done after redistributing rotational energy (*Bergemann and Boyd, 1993*) or before (*Bird, 1998*). The method presented here redistributes vibrational energy prior to rotational energy exchange following Bird. The normalized distribution function for post-collision vibrational level is:

$$\frac{f}{f_{\max}} = (1 - \frac{ik\Theta}{E_{(collision)}})^{3/2-\omega_{12}} \tag{2.47}$$

where ω_{12} is the temperature exponent of viscosity for molecules of type *1* and *2*.

The distribution function f is a function of the collisional energy and the post-collision vibrational energy level number i. Since the collision energy is known, i may be sampled using the acceptance-rejection method. At first an integer is randomly selected from the possible values of post-collisional vibrational energy level according to the total collision energy. It is known that f_{max} lies at i=0. The acceptance-rejection procedure is applied until i is determined. The collision energy is appropriately reduced to ensure energy conservation.

The methodology for discrete harmonic oscillators is an implementation of the generalized Larsen-Borganakke model and shares its advantages. The vibrational mode of interest may be redistributed serially with rotational or other vibrational

modes. In the case of two particles with internal energies, the Larsen-Borgnakke model may be applied to each particle in turn.

Validation of Larsen-Borgnakke Model for Rotational Relaxation

The relaxation of a rotational temperature is considered in order to validate the continuum form of the Larsen-Borgnakke model for rotational degrees of freedom. For known initial values of translational and rotational temperatures, an otherwise unperturbed gas will relax towards an equilibrium temperature. The formulation of the Larsen-Borgankke allows an analytical expression for the temperatures of rotation and translation (from *Bird, 1998*):

$$T_i = T_e - (T_e - T_{i,o})\exp(-\upsilon \Lambda t) \tag{2.48}$$

In this equation, T_i is the temperature of internal modes, T_e is the equilibrium temperature of the gas, and $T_{i,o}$ is the initial temperature of internal modes. The collision frequency, υ, may be determined from the molecular model, either hard spheres or variable hard spheres. To test rotational relaxation, nitrogen is used with the translation temperature set initially to 500 K and the rotational temperature set to 0 K. The rotational collision number (which is the typical number of collisions before rotational energy is redistributed), $1/\Lambda$, was set to be 5, typical for nitrogen. The analytical expressions for translational and rotational temperature become:

$$T_{tr} = 300 + 200\exp(-\upsilon t/5) \tag{2.49}$$

$$T_{rot} = 300\{1 - \exp(-\upsilon t/5)\} \tag{2.50}$$

These analytic results are compared with DSMC computations in Figure 9 of a gas with no energy transfer to the boundary in terms of the product of collision rate and simulation time. The scatter shown is well within statistical scatter for such a small number of particles (20,000). The results are comparable to those in *Bird, 1998*. The VHS exponent for the case is 0.24 (viscosity temperature exponent ~ 0.74). The HS calculations lies within the bound of the theoretical equations and the VHS calculations match the theory almost exactly, as in *Bird*.

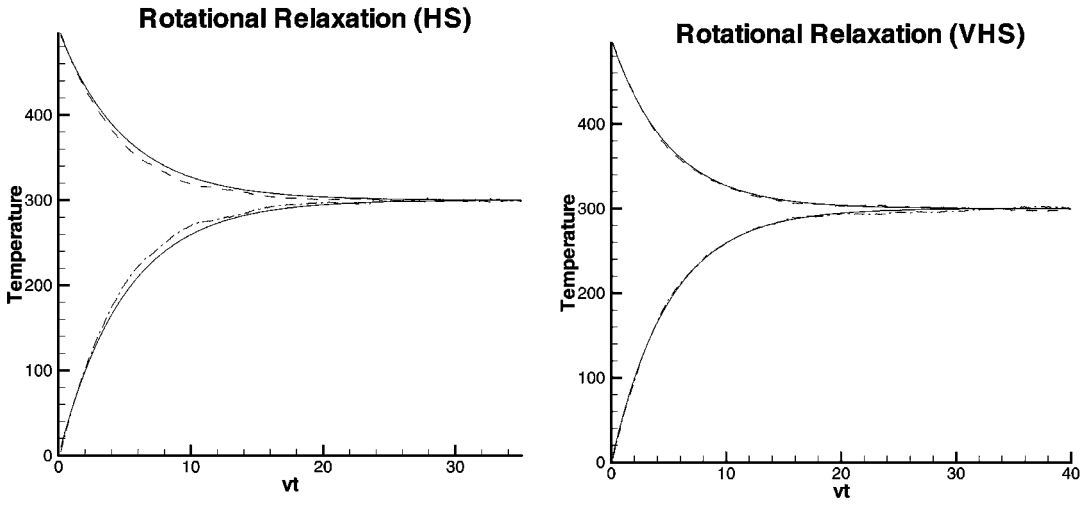

Figure 9. Analytic (solid lines) and computed (dashed lines) values of translational and rotational temperature (upper and lower contours, respectively) [K] graphed against the product of collision frequency and simulation time. HS and VHS molecular models.

Several different formulations have been considered in other works as attempts to improve on the Larsen-Borgnakke method. Energy may be distributed internally based upon collision pairs instead of considering each molecule in a pair

individually. By comparison with the analytical results above, the relaxation for the formulation based on collision pairs happens more slowly.

One criticism of the Larsen-Borgnakke model is that it is physically unrealistic in as far as only a fraction of the collisions are considered inelastic. Another formulation distributes a fraction Λ of the calculated change in rotational energy at each collision. As *Bird* (1998) points out, this does not satisfy detailed balancing and the result does not lead to the analytic temperature distribution for rotational energy. These procedures are avoided and the Larsen-Borganakke model is accepted for what it is – a phenomenological method that accurately predicts transfer of energy to internal modes for situations where the concept of an effective temperature of a collision is valid. If it is highly desirable to accurately model translational energy transfer or if the assumption of random molecular orientation is far from valid, more accurate transfer models may be used at the expense of higher computation time. The Larsen-Borgnakke model has shown good results in comparison with empirical data for flows of engineering interest, including those where equilibrium of translational temperature breaks down.

Validation of Larsen-Borgnakke Model for Vibrational Relaxation

The discrete Larsen-Borgnakke model for vibrational energy may be validated by comparison with computational results of known validity. As the method of redistribution is identical to Bird's methodology, we turn to his handbook (*Bird, 1998*) that provides an excellent example for comparison. Again, the general scheme

is to examine relaxation times versus temperature for a gas with internal degrees of freedom initially set to zero vibrational temperature and a high translational temperature.

The DSMC simulation took place in an adiabatic box using a diatomic gas with a single vibrational mode with a characteristic temperature of 2000K. Variable hard spheres were used as the molecular model. The translational temperature was initially 5000K and the rotational and vibrational temperature was initially 0K. The collision numbers for rotational and vibrational energy exchange were both set to be 5. Though five is unrealistically high for a collision number for vibrational exchange, it allows the behavior of the rotational and vibrational energy exchange to be compared. The vibrational temperature of the gas was determined from the near equilibrium equation:

$$T_{vib} = \Theta_{vib} / \ln(N_0 / N_1) \tag{2.51}$$

where N_o and N_1 are the number of molecules in the ground and first excited state, respectively.

The results shown in Figure 10 agree well with Bird, both qualitatively and quantitatively. The discrepancy between vibrational temperature evolutions may be due to different values of the variable hard sphere exponent between this simulation and that of Bird, as the VHS exponent is not given by Bird for this simulation.

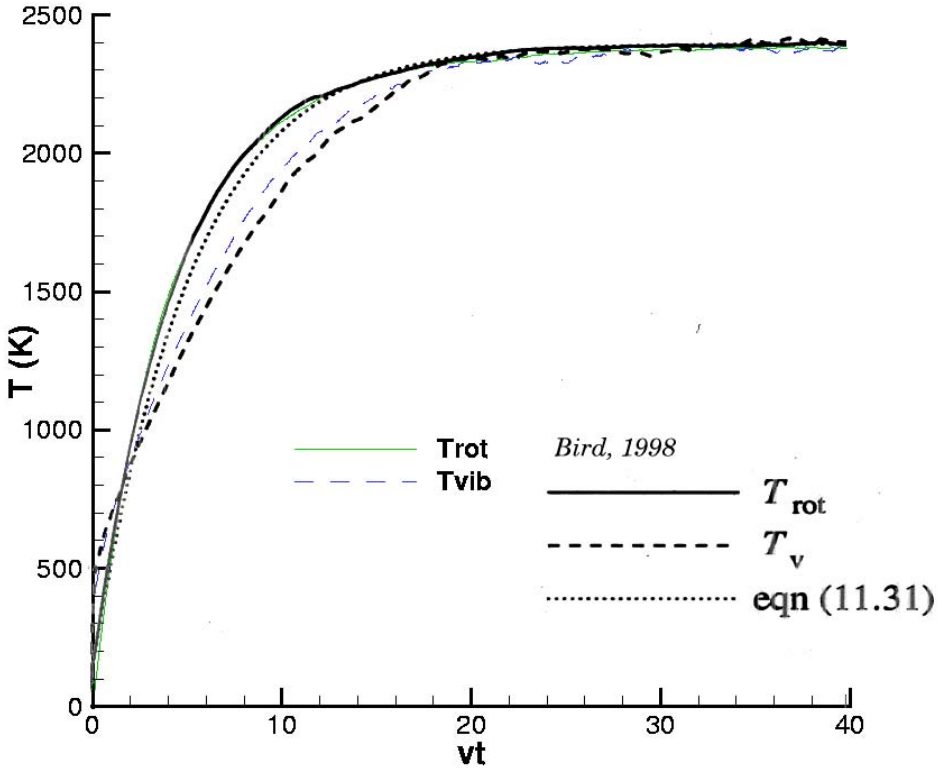

Figure 10. Comparison of calculated rotational, vibrational relaxation with Bird's results. Eqn. 11.31 in *Bird* is the results if vibrational energy was continuous rather than discrete.

2.3.6 Boundary Conditions for Gas-Surface Interaction

The details of gas-surface interaction are not generally known for an arbitrary surface. When a gas molecule strikes a surface, it may be absorbed, react with the surface, or be reflected. Unless surface mechanics are important in the problem of interest, it is standard practice in DSMC to assume that all gas molecules impinging on a surface are reflected.

When a gas molecule strikes a surface, some or all of its momentum and energy may be transferred to the surface. Similarly, the thermal (vibrational) motion of the surface molecules may transfer momentum and energy to the gas molecule. Determining how much momentum and energy is transferred in a gas-surface collision is a detailed problem based primarily on surface roughness and the gas adsorbed on the surface. A qualitative model of gas-surface interaction may be developed by the specification of accommodation coefficients – for energy (thermal), normal and tangential momentum. The accommodation coefficients expresses the ratio of the quantity transferred between the gas molecule and the wall over the quantity available for transfer.

The thermal accommodation coefficient (*Wachman, 1992*) is defined as the difference in temperature (equivalently, energy) between the impinging molecule and the reflected molecule over that between the impinging molecule and the wall, according to

$$\alpha = \frac{T_{incident} - T_{reflected}}{T_{incident} - T_{surface}} = \frac{E_{incident} - E_{reflected}}{E_{incident} - E_{surface}} \tag{2.52}$$

where $E_{surface}$ is the energy that would be carried away by the molecule if it had totally equilibrated to the surface temperature. The limits of the thermal accommodation coefficient, zero and unity, correspond to a molecule reflecting with no energy exchange to the wall and total thermal accommodation with the wall, respectively. These correspond to specularly and diffusely reflecting boundaries.

For specularly reflecting boundaries, no momentum or energy is exchanged with the wall. Specular reflection may be used to model either rigid surfaces or planes of symmetry. If a particle strikes a specularly reflecting surface, the normal component of the particle's velocity changes its sign.

For diffusely reflecting boundaries, the temperature of reflected particles is given as the wall temperature. After the particle strikes the boundary, a new velocity must be prescribed to the particle, which is generated through the equilibrium distribution with the wall's temperature. This is similar to the injection of particles from a surface element using the Maxwellian distribution with zero mean flow velocity.

As most engineering surfaces have sufficient microscopic roughness and adsorbed gas molecules near the surface, using diffuse reflection is a good characterization of the boundary. Conditions where this assumption is questionable are given in *Bird, 1998*.

2.3.7 Neutral Particle Motion

The DSMC method is a stochastic solution to Boltzmann's equation:

$$\frac{\partial f}{\partial t} + \mathbf{v} \bullet \nabla f + \frac{1}{m} \mathbf{F} \bullet \nabla_V f = \left(\frac{\partial f}{\partial t} \right)_{collisions} \tag{2.53}$$

where f is the velocity distribution function and ∇_V is the del operator with respect to velocity space coordinates. Since the DSMC method uncouples collisional and movement operations, the particle motion phase of computations corresponds to

solution of the collisionless Boltzmann equation. The equations of motion for a neutral particle are

$$m\frac{d\mathbf{v}}{dt} = \mathbf{F} \tag{2.54}$$

$$\frac{d\mathbf{x}}{dt} = \mathbf{v} \tag{2.55}$$

For a non-constant (or non-uniform) body force, an integration scheme must be used to update the equations of motion. However, the only forces on neutral particles is the collisional force and gravity. Collisions are dealt with using the molecular cross-section concept. As gravity is constant, no accuracy is lost in the application of the force either before or after the particle motion phase of computations.

Particles are moved between adjacent tetrahedral cells using a particle tracing technique. The intersection of a particle with the plane defined by a triangular cell face is expressed as a system of linear equations involving two edges of the face, the current particle position, and velocity. Solution of these equations yields the time of intersection and point of intersection in a skewed coordinate system defined by the edges used in the calculation. Intersections occurring outside the face or in negative time are ignored. If the particle does intersect the face, its position and owning cell are updated. Small displacements are made relative to the face dimensions if the intersection occurs near the edges of the face, in order to avoid intersecting near an edge that may lead to an incorrect solution with any finite precision. Each face of the current cell is checked in turn for intersection.

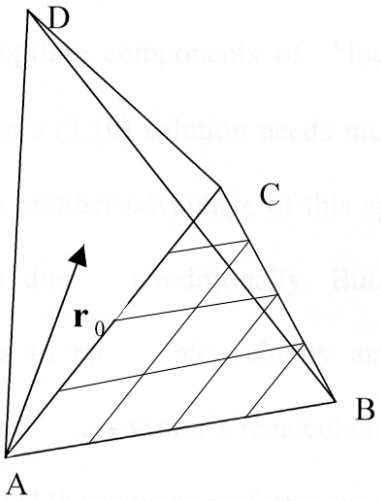

Figure 11. Skew local coordinate system used for particle tracing for face ABC.

Following Figure 11, the intersection of a particle with initial position $\mathbf{r_o}$ and velocity **v** with face ABC is

$$\mathbf{r}_o + \mathbf{v}\tau = \alpha\overrightarrow{AB} + \beta\overrightarrow{AC} \tag{2.56}$$

In this equation, $\overrightarrow{AB}$ and $\overrightarrow{AC}$ are the vectors from point *A* to points *B* and *C*, respectively, τ is the time elapsed in moving from the initial point to the plane defined by points *A*, *B*, and *C*; α and β define the point of intersection in the skewed coordinate system of face *ABC*. If the time τ is negative, an intersection does not occur. If α or β are less than zero or greater than unity, an intersection does not occur within the face. If the sum of α and β is greater than unity, then the intersection occurs outside the face.

The linear system of equations does not necessarily have good characteristics and may be ill-conditioned if the cells and corresponding faces are badly shaped or

velocity is very large. In practice, the former is more severe than the latter as the latter may be prevented by using a smaller global time-step.

2.4 Plasmadynamics via the Particle in Cell Method

The necessary equations for expression of the electrostatic condition are available from two of Maxwell's equations:

$$\nabla \times \mathbf{E} = -\frac{\partial \mathbf{B}}{\partial t} = 0 \qquad \text{Faraday's Law} \qquad (2.57)$$

$$\nabla \bullet \mathbf{E} = \frac{\rho}{\varepsilon_o} \qquad \text{Gauss's Law} \qquad (2.58)$$

This limit assumes the magnetic field induced by currents in the domain of interest is negligible, though a external magnetic field, **B**, (nearly) constant in time is still permitted in the approximation. In the electrostatic approximation, the electric field may be expressed as the gradient of a scalar potential:

$$\mathbf{E} = -\nabla \Phi \qquad (2.59)$$

Gauss's law then becomes Poisson's equation for the case of electrostatics:

$$\nabla^2 \Phi = -\frac{\rho}{\varepsilon_o} = -\frac{\sum_{i=1}^{Ni} q_i n_i + q_e n_e}{\varepsilon_o} \qquad (2.60)$$

In the above, the total charge density in the volume of interest is ρ; ε_o is the permitivity of free space; N_i is the number of ionized species; q is the charge per particle, and n is the number density. The subscripts i and e denote ion and electron species, respectively.

The differential form of Gauss's law may be applied over a closed surface S with outward unit normal $\hat{\mathbf{n}}$ which and results in the integral form of Gauss's law:

$$\varepsilon_o \oiint_S \mathbf{E} \cdot \hat{\mathbf{n}} dA = \iiint_V \rho dV = Q \tag{2.61}$$

where Q is the total charge enclosed.

2.4.1 Charged Particle Loading

The loading of the domain with charged particles is accomplished in a manner identical to the loading of neutral particles described in Section 2.3.2. Particle velocities are sampled from a drifting Maxwellian distribution function. Positions are randomly assigned such as to maintain the necessary density. As the leap-frog method is used for the integration of the equations of motion for charged particles, it is necessary to move the velocities back half a time step using the force field values at the initial time. This is done after all particles are loaded into the domain.

2.4.2 Charged Particle Injection

The injection of charged particles into the domain is accomplished in a manner identical to the injection of neutral particles described in Section 2.3.3. Particle velocities are sampled from the portion of the Maxwellian equilibrium distribution function that correspond to particles which could physically cross an open surface with the prescribed drift velocity. As the leap-frog method is used for the integration of the equations of motion for charged particles, it is necessary to move the velocities back half a time step using the force field at the current time.

This is done after each particle is moved into the domain a random fraction of a time step using the initial velocity sampled from the equilibrium distribution function.

2.4.3 Charged Particle Motion

In a plasma, the equation of motion of a particle is coupled with the electromagnetic fields. The equations of motion for non-relativistic particles in vector form are:

$$m\frac{d\mathbf{v}}{dt} = \mathbf{F} \tag{2.62}$$

$$\frac{d\mathbf{x}}{dt} = \mathbf{v} \tag{2.63}$$

The leap-frog method shown schematically in Figure 12, obtains second-order accuracy in time through use of a velocity that is staggered at half time-steps relative to the particle position. The particle position and velocity derivatives are discretized using a linear finite difference form:

$$m\frac{\mathbf{v}^{n+1/2} - \mathbf{v}^{n-1/2}}{\Delta t} = \mathbf{F}^n \tag{2.64}$$

$$\frac{\mathbf{x}^{n+1} - \mathbf{x}^n}{\Delta t} = \mathbf{v}^{n+1/2} \tag{2.65}$$

where n is the time-step counter. The time centered property of the discretized equations is what gives second order accuracy, as can be seen from examination of the Taylor series. The leap-frog method requires minimal information to be stored with respect to velocity and position, as the new values of velocity and position may

be updated directly from previous values and only one set of velocity and position components need be stored.

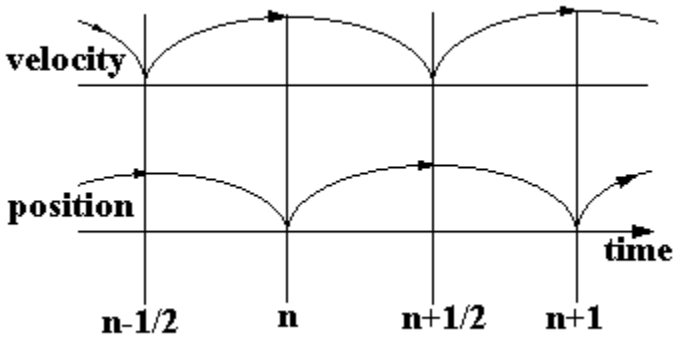

Figure 12. Schematic of leap-frog integration method (from *Birdsall, 1991*).

In the case of PIC, the force on a charged particle is due to the Lorentz force:

$$\frac{d\mathbf{v}}{dt} = \frac{q}{m}(\mathbf{E} + \mathbf{v} \times \mathbf{B}) \tag{2.66}$$

This may be discretized by using a time-centered average for the magnetic term, consistent with the leap-frog formulation. The discretized form of the equation is:

$$\frac{\mathbf{v}^{n+1/2} - \mathbf{v}^{n-1/2}}{\Delta t} = \frac{q}{m}(\mathbf{E}^n + \frac{\mathbf{v}^{n+1/2} - \mathbf{v}^{n-1/2}}{2} \times \mathbf{B}^n) \tag{2.67}$$

Since the previous velocity is known, the above represent a set of three equations and three unknowns for the velocity at the new time step. However, computationally faster methods have been developed to obtain the new velocity. The methodology discussed here is from *Birdsall et al.,* (*1991*) following a method developed by *Boris,* (*1970*).

The magnetic and electric forces may be separated completely from the substitution of two new variables into the discretized force equation:

$$\mathbf{v}^{n-1/2} = \mathbf{v}^{-} - \frac{q\mathbf{E}^{n}}{m}\frac{\Delta t}{2} \tag{2.68}$$

$$\mathbf{v}^{n+1/2} = \mathbf{v}^{+} + \frac{q\mathbf{E}^{n}}{m}\frac{\Delta t}{2} \tag{2.69}$$

Contributions from the electric field cancel entirely, which leaves just a rotation due to the magnetic field:

$$\frac{\mathbf{v}^{+} - \mathbf{v}^{-}}{\Delta t} = \frac{q}{2m}(\mathbf{v}^{+} + \mathbf{v}^{-}) \times \mathbf{B}^{n} \tag{2.70}$$

Half of the electric impulse is added to the initial velocity to obtain $\mathbf{v}^{-}$, the rotation is performed to obtain $\mathbf{v}^{+}$, and then the second half of the electric impulse is added to $\mathbf{v}^{+}$.

The magnitude of the angle of rotation can be evaluated from construction of the vectors $\mathbf{v}^{+}$ and $\mathbf{v}^{-}$ according to

$$\left|\tan\frac{\theta}{2}\right| = \frac{\left|\mathbf{v}_{\perp}^{+} - \mathbf{v}_{\perp}^{-}\right|}{\left|\mathbf{v}_{\perp}^{+} + \mathbf{v}_{\perp}^{-}\right|} = \frac{q|\mathbf{B}|}{m}\frac{\Delta t}{2} \tag{2.71}$$

The velocity components in this equation are perpendicular to the magnetic field and θ is the angle between the velocity vectors.

Several steps are necessary to implement the rotation due to the magnetic field efficiently. First, $\mathbf{v}^{-}$ is incremented to produce a vector $\mathbf{v}'$ which is perpendicular to both $(\mathbf{v}^{+} - \mathbf{v}^{-})$ and $\mathbf{B}$ according to

$$\mathbf{v}' = \mathbf{v}^{-} + \mathbf{v}^{-} \times \mathbf{t} \tag{2.72}$$

The vector **t** is defined from the requirement that the angle between $\mathbf{v}^-$ and $\mathbf{v}^+$ is *θ/2* according to

$$\mathbf{t} \equiv \frac{q\mathbf{B}}{m}\frac{\Delta t}{2} \tag{2.73}$$

Since $\mathbf{v}^+ - \mathbf{v}^-$ is parallel to $\mathbf{v}' \times \mathbf{B}$, $\mathbf{v}^+$ can be found from

$$\mathbf{v}^+ = \mathbf{v}^- + \mathbf{v}' \times \mathbf{s} \tag{2.74}$$

The vector **s** is parallel to **B** and its magnitude is determined by the requirement that the square of the velocities (kinetic energy) is unchanged by the rotation according to

$$\mathbf{s} = \frac{2\mathbf{t}}{1+t^2} \tag{2.75}$$

This algorithm, from Boris (*1970*), may be made relativistic if necessary for the simulation.

Updating of particle positions is performed identically to that of the neutral case, using the particle tracing technique for unstructured tetrahedral grids. Consideration of grid quality for PIC computations has the same issues as for DSMC.

2.4.4 Validation of Leap-Frog Integration for Particle Motion

A simple test was performed to ensure that leap-frog integration was implemented correctly and that sufficient accuracy is achieved for particle velocity and position versus time. A single ion was placed randomly in a domain with a steady electric field (1000 V/m) resulting from the monotonic decay of potential between two infinite conducting plates 0.1 m apart. The force should be steady on

the particle – velocity is expected to increase linearly and position quadratically. The particle was monitored until it hit a surface.

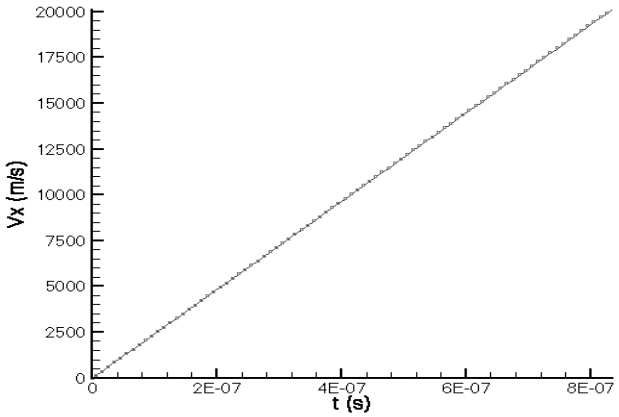

Figure 13. Particle velocity in x-direction versus time. The line indicates analytic results and the symbols are calculated results.

Computational results shown in Figure 13 and Figure 14 are nearly identical to analytic results. It was noted in preliminary results of this test when runs were made with multiple particles and a very large time step that some particles escaped the domain, despite the precautions taken to detect and eliminate lost particles. These particles contributed physically unrealistic values of charge due to use of the Lagrange weighting procedure outside of the domain. This illustrates the importance of using a time-step appropriate to the simulation of interest.

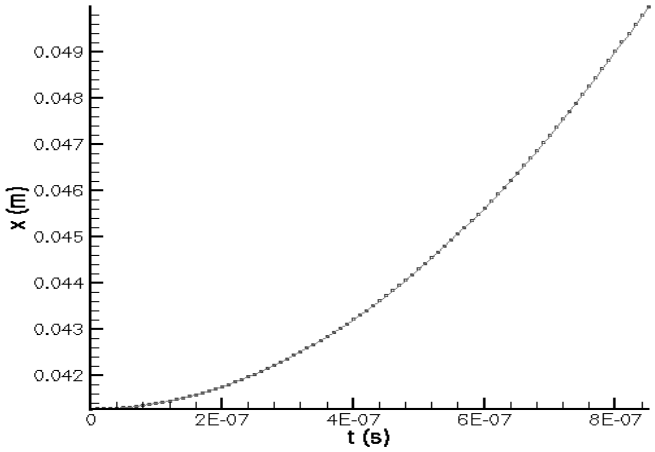

Figure 14. Particle position versus time. The line indicates analytic results and the symbols indicate calculated results.

2.4.5 Finite Volume Method for Poisson's Equation in Delaunay Tetrahedral Domains

The finite volume method separates the domains into discrete control volumes. In each control volume, the differential equation is discretized. When applicable, integrals over volume involving gradients are transformed into integrals over surfaces using the divergence theorem. Similarly, integrals over surfaces may be transformed into integrals around closed contours and back using Stokes's theorem. Quantities in a single cell, face, or edge may be considered constant or vary depending on the formulation or accuracy desired.

The order of error for a finite difference or finite element formulation is given as the highest derivative kept from a Taylor series expansion. Using two evenly spaced points about the point of interest, one may obtain an expression second-order

accurate in space for the first derivative. Considering the direction x to be the direction that the points are collinear:

$$\left.\frac{\partial u}{\partial x}\right)_{i,j} = \frac{u_{i+1} - u_{i-1}}{2\Delta x} + O(\Delta x)^2 \tag{2.76}$$

Overall accuracy may be increased by considering more points in the Taylor series or using small values of spacing.

In this work, advantage is taken of the Voronoi dual of the Delaunay triangulation in order to formulate a finite volume method for Poisson's equation with accuracy adequate for engineering calculations. The Voronoi cell corresponding to each Delaunay node contains the set of points closer to that point than any other. Also, the facets of the Voronoi cell are orthogonal to the lines joining the tetrahedral nodes.

Finite Volume Formulation

If one considers a node-centered finite-volume scheme with finite volume i associated with node i with a number of faces N_F that is (in theory) small enough to accurately capture the physics, the semi-discrete equation form of Gauss's law is:

$$\sum_{k=1}^{N_{F,i}} \mathbf{E} \bullet \mathbf{A}_{i,k} = \frac{Q_i}{\varepsilon_o}. \tag{2.77}$$

In the above, Q_i is the total charge enclosed by volume i, $A_{i,k}$ is the area of the face k of associated with volume i, and the summation is over all the faces of the finite volume as shown in Figure 15 for a 2-D case. Using the electric potential Φ:

$$\sum_{k=1}^{N_F} \nabla\Phi \bullet \left(\hat{\mathbf{n}} A\right)_{i,k} = \sum_{k=1}^{N_F} \left(A \frac{\partial \Phi}{\partial n} \right)_{i,k} = -\frac{Q_i}{\varepsilon_o} \tag{2.78}$$

where $\mathbf{A}_{i,k}=(A\,\hat{\mathbf{n}})_{i,k}$ is the magnitude of the area of the face k for the volume associated with node i multiplied by the unit outward normal vector. In deriving Eq. (2.78), we used the definition of the gradient,

$$\nabla\Phi \bullet \hat{\mathbf{n}} = \frac{\partial \Phi}{\partial n}. \tag{2.79}$$

As the planes defined by the faces of the Voronoi dual are orthogonal to the edges of the tetrahedral grid and contain the midpoint of each edge, an expression for the derivative at the faces of the Voronoi dual may be obtained from the central difference method which is second-order accurate with node spacing.

$$\frac{\partial \Phi}{\partial n}\Bigg)_i = \frac{\Phi_{i+1} - \Phi_{io}}{L} + O(h^2). \tag{2.80}$$

Here, *io* (equivalent to *i-1* in a standard finite difference lattice) denotes the index of the node in the Voronoi cell of interest, *i+1* is the index of the node at the opposing end of the edge, and L is the distance between the nodes. Note that switching places of the index counters switches the sign of the derivative, which may be taken advantage of during computations. The local value of node spacing (in this case, one half the edge length) is denoted as h.

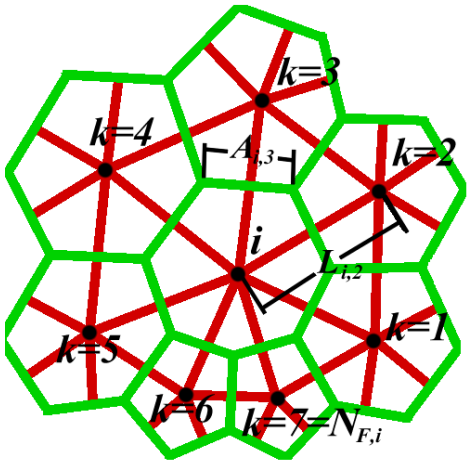

Figure 15. Example of 2-D Delaunay mesh (red lines)and its Voronoi dual (green lines) used in electrostatic computations.

An approximation of the electric flux into a cell containing node *i* across a Voronoi face corresponding to an edge with nodes *k* and *i* is:

$$\sum_{k=1}^{N_{F,i}} \nabla\Phi \bullet \left(\hat{\mathbf{n}} A\right)_{i,k} = \frac{A_{i,k}}{L_{i,k}} (\Phi_k - \Phi_i) \tag{2.81}$$

In the above, $L_{i,k}$ is the distance from node *i* to node *k*. Summing over all faces *k* of a Voronoi cell corresponding to node *i*, a system of linear equations may be formed assuming the charge inside the volume, Q_i, is known. The system is

$$\sum_{k=1}^{N_{F,i}} (\Phi_i - \Phi_k) \frac{A_{i,k}}{L_{i,k}} = \frac{Q_i}{\varepsilon_o} . \tag{2.82}$$

It is noted that this method reduces to the standard 2nd order finite-difference method on Cartesian meshes.

The matrix form of this equation is:

$$\begin{bmatrix} R_{1,1} & R_{1,2} & R_{1,3} & \cdots & R_{1,N} \\ R_{2,1} & R_{2,2} & R_{2,3} & \cdots & R_{2,N} \\ R_{3,1} & R_{3,2} & R_{3,3} & \cdots & R_{3,N} \\ \vdots & \vdots & \vdots & \ddots & \vdots \\ R_{N,1} & R_{N,2} & R_{N,3} & \cdots & R_{N,N} \end{bmatrix} \begin{Bmatrix} \Phi_1 \\ \Phi_2 \\ \Phi_3 \\ \vdots \\ \Phi_N \end{Bmatrix} = \frac{1}{\varepsilon_o} \begin{Bmatrix} Q_1 \\ Q_2 \\ Q_3 \\ \vdots \\ Q_N \end{Bmatrix} \tag{2.83}$$

N is the number of nodes in the mesh. $R_{i,j}$ is the coefficient, which is determined by

$$R_{i,j} = \sum_{k=1}^{N_{F,i}} \frac{A_{i,k}}{L_{i,k}} \text{ for } i = j, \tag{2.84}$$

$$R_{i,j} = -\frac{A_{i,j}}{L_{i,j}} \text{ if } j \text{ is adjacent to } i, \tag{2.85}$$

$$R_{i,j} = 0 \text{ otherwise.} \tag{2.86}$$

$\frac{A_{i,j}}{L_{i,j}}$ is the ratio of the area of the Voronoi face between nodes i and j to the distance between nodes i and j if the nodes.

The resulting symmetric matrix equations may be solved for using any standard solution technique. The sparse matrix was stored in compressed row storage (CRS) format that is computationally efficient both in terms of storage and matrix operations. Details of the CRS format may be found in Hammel (2001).

Electric Field Evaluation

The divergence theorem may be used to construct the electric field (negative of the gradient of the potential) in a volume of interest. For a volume V bound by a surface S composed of n faces F_i, the divergence theorem is expressed as

$$\int_V \nabla \bullet \mathbf{Y} dV = \oint_S \mathbf{Y} \bullet d\mathbf{A} \tag{2.87}$$

where ***Y*** is a vector and *dA* is an outward normal differential surface element. A formula for the gradient can be constructed through use of a constant vector ***k***,

$$\int_V \nabla\bullet(\Phi\mathbf{k})dV = \oint_S \Phi\mathbf{k}\bullet d\mathbf{A}\,. \tag{2.88}$$

Since ***k*** is arbitrary and constant, it may be taken outside of the integral and divided out according to

$$\mathbf{k}\bullet\int_V \nabla\Phi dV = \mathbf{k}\bullet\oint_S \Phi d\mathbf{A} \tag{2.89}$$

$$\int_V \nabla\Phi dV = \oint_S \Phi d\mathbf{A}\,. \tag{2.90}$$

To this point, the formulation is arbitrary and exact. If one assumes that the gradient varies only slightly over the control volume and the potential is constant for a given face, a discrete formulation of equation (2.90) may be constructed as follows:

$$\nabla\Phi = \frac{1}{V}\sum_{i=1}^{n}\Phi_i\mathbf{S}_i \tag{2.91}$$

where $\mathbf{S_i}$ is the outward normal vector of face *i* with a magnitude equal to the area of the face.

Since the potential is known at the nodes and not the faces of either the Delaunay or Voronoi mesh, averaging must be done to obtain the potential at the faces. It is worth noting that this is a general method for finding the gradient on unstructured meshes with minimal information.

Another method of finding the gradient of a scalar function known at the nodes on general meshes is the least squares algorithm. A locally linear variation of the potential is assumed, such that

$$\Phi_o + \nabla\Phi \bullet \Delta\mathbf{r} = \Phi_1 \tag{2.92}$$

where, $\Delta\mathbf{r}$ is the vector from node *0* to node *1*. For a point with *J* neighbors, this may be written in Cartesian coordinates considering the neighbor point *j* as

$$\Delta x_j \left.\frac{\partial\Phi}{\partial x}\right|_o + \Delta y_j \left.\frac{\partial\Phi}{\partial y}\right|_o + \Delta z_j \left.\frac{\partial\Phi}{\partial z}\right|_o = \Phi_j - \Phi_o \tag{2.93}$$

In matrix form, this is expressed as

$$\overline{\overline{\mathbf{M}}}\mathbf{d} = \Delta\Phi \tag{2.94}$$

where, $\overline{\overline{\mathbf{M}}}$ is the $J \times 3$ matrix:

$$\overline{\overline{\mathbf{M}}} = \begin{bmatrix} \Delta x_1 & \Delta y_1 & \Delta z_1 \\ \Delta x_2 & \Delta y_2 & \Delta z_2 \\ \vdots & \vdots & \vdots \\ \Delta x_J & \Delta y_J & \Delta x_J \end{bmatrix}. \tag{2.95}$$

In Equation (2.94), **d** is the components of the gradient at node *0:*

$$\mathbf{d} = \begin{bmatrix} \left.\frac{\partial\Phi}{\partial x}\right|_o \\ \left.\frac{\partial\Phi}{\partial y}\right|_o \\ \left.\frac{\partial\Phi}{\partial z}\right|_o \end{bmatrix} \tag{2.96}$$

and $\Delta\Phi$ is the length *J* vector of differences in Φ:

$$\Delta\Phi = \begin{bmatrix} \Phi_1 - \Phi_o \\ \Phi_2 - \Phi_o \\ \vdots \\ \Phi_J - \Phi_o \end{bmatrix} \tag{2.97}$$

This linear system contains J equations and three unknowns. Since in practice J will be larger than three, this is an over-determined system. Physically, this means that we cannot assume a linear profile for the potential around point *0* such that exactly reconstructs the known solution at all of its neighbors. It is necessary to search for a solution that fits this data in the best possible way.

The least squares method gives a way to find a solution to this system that minimizes the root mean square value of error. The error in the reconstructed value for point j is given by

$$R_j = \Delta x_j \left.\frac{\partial\Phi}{\partial x}\right|_o + \Delta y_j \left.\frac{\partial\Phi}{\partial y}\right|_o + \Delta z_j \left.\frac{\partial\Phi}{\partial z}\right|_o - (\Phi_j - \Phi_o) \tag{2.98}$$

The square of the error over all the neighbors of point *0* is

$$R = \sum_j R_j^{\,2} = \sum_j \left[\Delta x_j \left.\frac{\partial\Phi}{\partial x}\right|_o + \Delta y_j \left.\frac{\partial\Phi}{\partial y}\right|_o + \Delta z_j \left.\frac{\partial\Phi}{\partial z}\right|_o - (\Phi_j - \Phi_o) \right]^2 \tag{2.99}$$

It is desired to find the derivatives of the potential such that the error is minimized. The standard way is the differentiate R with respect to the derivatives of the potential and set the result equal to zero:

$$\frac{\partial R}{\partial\left(\left.\frac{\partial\Phi}{\partial x}\right|_o \right)} = 0 \tag{2.100}$$

$$\frac{\partial R}{\partial\left(\left.\frac{\partial \Phi}{\partial y}\right|_o\right)} = 0 \tag{2.101}$$

$$\frac{\partial R}{\partial\left(\left.\frac{\partial \Phi}{\partial z}\right|_o\right)} = 0 \tag{2.102}$$

This set of equations is the same as that obtained by multiplying the matrix equation for $\overline{\overline{\mathbf{M}}}$, $\mathbf{d}$, and $\Delta\Phi$ by the transpose of $\overline{\overline{\mathbf{M}}}$:

$$\overline{\overline{\mathbf{M}}}^T \overline{\overline{\mathbf{M}}}\mathbf{d} = \overline{\overline{\mathbf{M}}}^T \Delta\Phi \tag{2.103}$$

This is a set of three equations and three unknowns that may be solved for by a standard linear algebra technique.

Implementation of Gradient Calculations on Unstructured Meshes

Several methods of calculating the gradient were studied in order to assess their relative accuracy. Both the control volume approach (from the divergence theorem) and least-squares approach gave an approximation of the gradient usable in calculations.

The least squares approach was implemented using the neighbors of the node sharing an edge of the Delaunay mesh. For the divergence approach, two different control volumes studied produced acceptable gradients: a tetrahedron (cell-centered gradient) and the volume of all tetrahedra which share the node of interest (node-centered scheme). The schemes are assessed here for applicability.

It is highly desirable to use the same particle weighting function as force weighting function (*Birdsall, 1991*). Use of different weighting functions represents different particle shapes for charge accumulation and field calculation and may lead to non-physical instabilities (*Birdsall, 1991*). Use of the same weighting function for charge accumulation and field distribution also eliminates the self-force and conserves momentum (*Birdsall, 1991*). Therefore, if it is desired to use linear Lagrange polynomials to accumulate charge at the node, the same function should be used to weight the electric field (and magnetic field, when applicable) back to the particles. Use of a tetrahedral cell-centered scheme is, in general, inappropriate to this type of weighting. Averaging techniques could be used to obtain the value at the node from the value at the cell, but it would be difficult to formulate an average that conserved all the relevant quantities of interest as well as was identical to the linear Lagrange function. Therefore, it is desirable for purposes of calculating the electric field from the electric potential to use a method that gives the gradient at the node. Cell-centered methods, if desirable, could be used for other purposes involving the calculation of the gradient on unstructured meshes.

It is noted that the cell-centered tetrahedral method and the node-centered method using all the cells bordering a node give equivalent results. It is obvious that the results obtained using the explicit node-centered control volume approach correspond to results at the node, while this is not necessarily obvious for the tetrahedral cell-centered method. The control volume for an interior node *i* is shown in Figure 16.

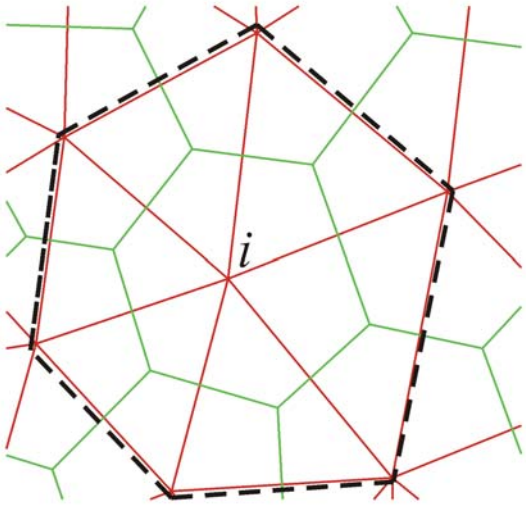

Figure 16. Volume used for interior node *i* for the calculation of the gradient using the divergence theorem.

Another method to calculate the gradient is the differentiation of the linear Lagrange function which can be used to approximate the potential in a node. At the nodes, this method is identical to the control volume method applied to the volume of all tetrahedra that contain the node. However, this method has the conceptual advantage that the field is applied directly to the particle and is consistent with using the same function to accumulate charge as to interpolate the electric field.

Each method studied is weakest at the boundaries of the domain, as information about the derivative is not available in the direction into the boundary. It is possible to correct the field at the boundaries of the mesh by using the imposed boundary conditions. For Neumann boundary conditions, the normal component of

the electric field is known and may be applied directly to the calculated gradient. For conductors, the electric field is normal to the boundary and its magnitude may be may be computed from the surface charge density:

$$\left|\mathbf{E}_i\right| = \frac{\sigma_i}{\varepsilon_o} \tag{2.104}$$

An expression for the surface charge density may be obtained to the discretized Gauss's law:

$$\sigma_i = \frac{\varepsilon_o \left[\sum_{k=1}^{N_{F,i}} (\Phi_i - \Phi_k) \frac{A_{i,k}}{L_{i,k}} \right] - Q_{(plasma)i}}{A_{(boundary)i}} \tag{2.105}$$

Correcting for the potential at the boundary proved to slightly increase the accuracy of the node-centered method.

The accuracy of the methods was studied numerically for problems of engineering interest. Accuracy of the methods was observed to be less than that obtained on Cartesian meshes, but could be acceptable for engineering calculations. The least squares method and both the tetrahedral cell-centered control volume method and node-centered control volume method share about linear accuracy. For the cell-centered method, values were obtained at the nodes by straight volume averaging over the cells sharing the node. It was noticed that all three methods exhibited problems in the same geometric regions, which indicates that spacing in these regions may need to be refined and that these methods suffer from some geometric biases. The best method was shown to be grid dependent, as least-squares

proved better on some meshes and the control volume method proved better on others.

One test used imposed a monotonic decay of potential between two infinite parallel conductors. For such a case, the value of the gradient should be a constant vector. All of the methods were accurate to within 7% for the component of electric field perpendicular to potential lines.

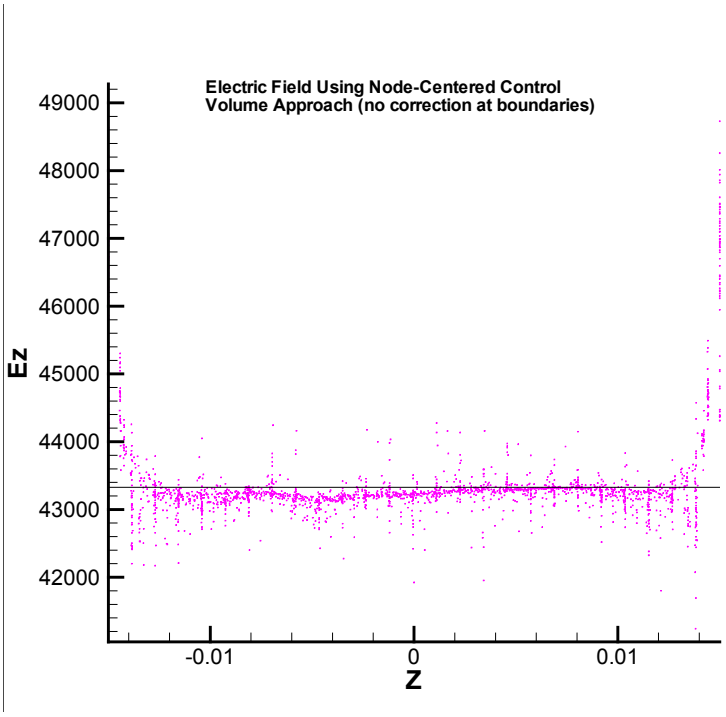

Figure 17. Electric field at grid points using the node-centered control volume method.

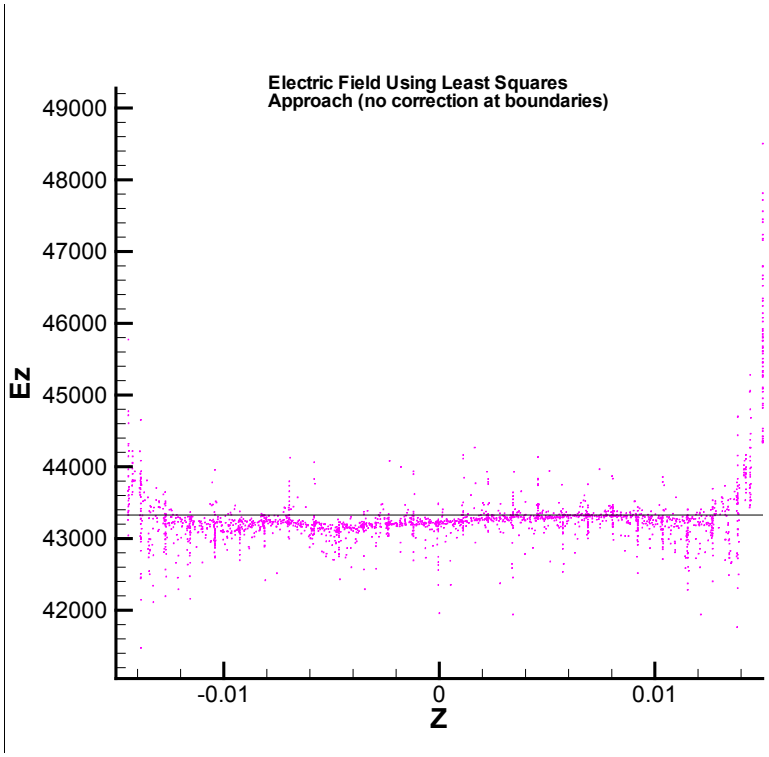

Figure 18. Electric field at grid points using least-squares method.

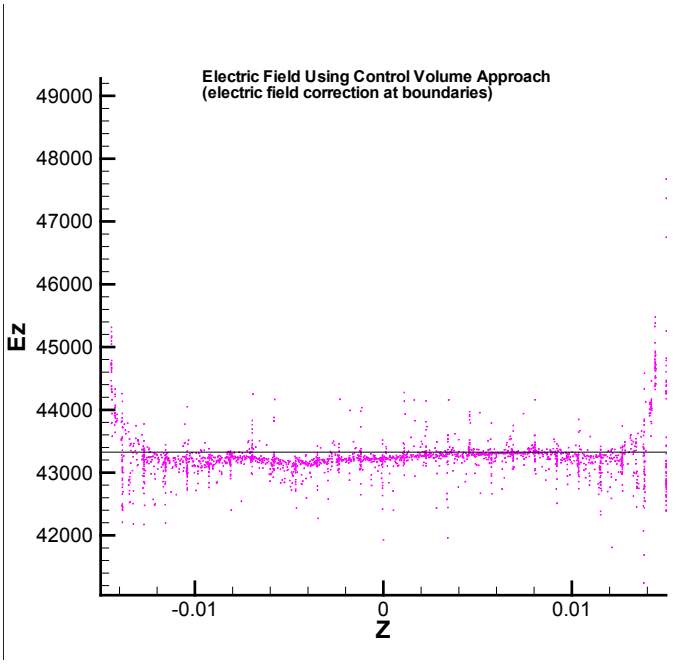

Figure 19. Electric field using the node-centered control volume approach using field corrections at the boundaries.

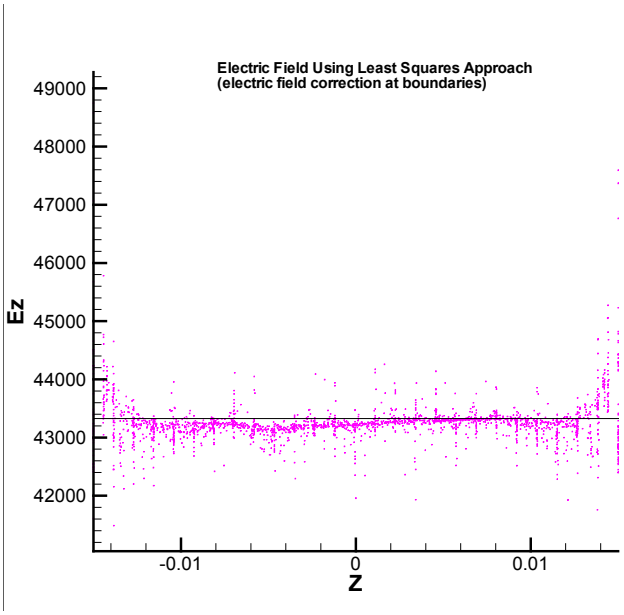

Figure 20. Electric field using the least squares approach using field corrections at the boundaries.

The results of the gradient calculations are shown in Figures 16-19. The analytical value for the field is 43,333 V/m, shown in solid black lines. Figures 16 and 17 illustrate the value of the electric field using the node-centered control volume approach and the least squares approach. Figures 18 and 19 illustrate the effect of correcting the electric field using boundary conditions. Figure 18 illustrates the node-centered control-volume approach and Figure 19 illustrates the least-squares approach. As seen in the illustrations, all methods have similar accuracy and suffer in accuracy in the same locations. Correcting for boundary conditions slightly improves the electric field near the boundaries. The electric field accuracy should be sufficient for most computations of engineering interest, but attention should be paid to locations and conditions where the electric field accuracy is questionable.

2.4.6 Boundary Conditions for PIC Methodology

In a bounded domain, a solution to Poisson's equation may be specified uniquely by piece-wise continuous Dirichlet and Neumann boundary conditions (*Jackson, 1999*). Dirichlet boundary conditions involve the specification of the voltage on the boundaries, as with a system of conductors. Neumann boundary conditions involve the specification of the component of the electric field normal to the surface. It is to be noted that a domain enclosed by only Neumann boundary conditions has an arbitrary (unspecified) zero potential, but as only the gradient of potential is of interest anyway, this should not be an issue of concern. The solution to a problem with the arbitrary specification of both Φ and $\partial \Phi / \partial n$ (Cauchy boundary conditions) does not exist for a bounded domain since the piece-wise specification of mixed boundary conditions determines the problem uniquely (*Jackson, 1999*).

Since the boundaries of the Delaunay mesh are forced to coincide with the boundaries of the tetrahedral mesh during the construction of the Voronoi mesh, the implementation of boundary conditions is straightforward and requires no special technique. Specification of voltage on the boundaries is considered a strong condition: the voltage is placed on the right hand side of the matrix and the corresponding row zeroed with a one placed on the diagonal. Fluxes due to the Neumann boundary condition are added to the flux formulation for the Voronoi cell corresponding to the boundary node. Dirichlet boundary conditions have precedence over Neumann boundary conditions in the case when a node is in the interface between boundary condition types.

To enforce a Dirichlet condition, the coefficient for the node of interest on the diagonal is set to unity and the rest of the row is zeroed. To enforce a Neumann condition, the value of the inward normal electric field multiplied by the boundary area is added to the right hand side of the node of interest.

This is illustrated in matrix form for the boundary shown in Figure 21. Node 1 is a node on a Dirichlet boundary with potential Φ_o. Node 2 is a node on a Neumann boundary with associated inward flux $E_{N,2}A_{N,2}$. Nodes 3 and N are interior nodes (not shown in figure). $R_{i,j}$ are the coefficients from Equations (2.84) to (2.86).

$$\begin{bmatrix} 1 & 0 & 0 & \cdots & 0 \\ R_{2,1} & R_{2,2} & R_{2,3} & \cdots & R_{2,N} \\ R_{3,1} & R_{3,2} & R_{3,3} & \cdots & R_{3,N} \\ \vdots & \vdots & \vdots & \ddots & \vdots \\ R_{N,1} & R_{N,2} & R_{N,3} & \cdots & R_{N,N} \end{bmatrix} \begin{Bmatrix} \Phi_1 \\ \Phi_2 \\ \Phi_3 \\ \vdots \\ \Phi_N \end{Bmatrix} = \frac{1}{\varepsilon_o} \begin{Bmatrix} \Phi_o \\ Q_2 + \varepsilon_o E_{N,2} A_{N,2} \\ Q_3 \\ \vdots \\ Q_N \end{Bmatrix} \tag{2.106}$$

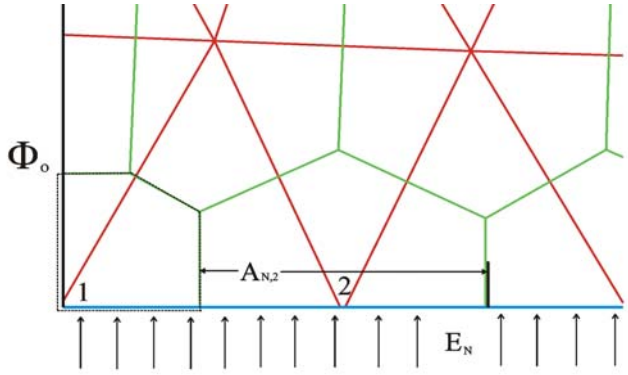

Figure 21. Illustration of enforcement of boundary conditions on Voronoi dual for nodes 1 and 2. Node 1 is on conducting boundary with potential Φ_o (black line). Node 2 is on a Neumann boundary with inward normal electric field E_N (blue line). The control volume associated with node 1 is shown as a dotted line.

2.4.7 PIC Simulation of Bounded Plasmas

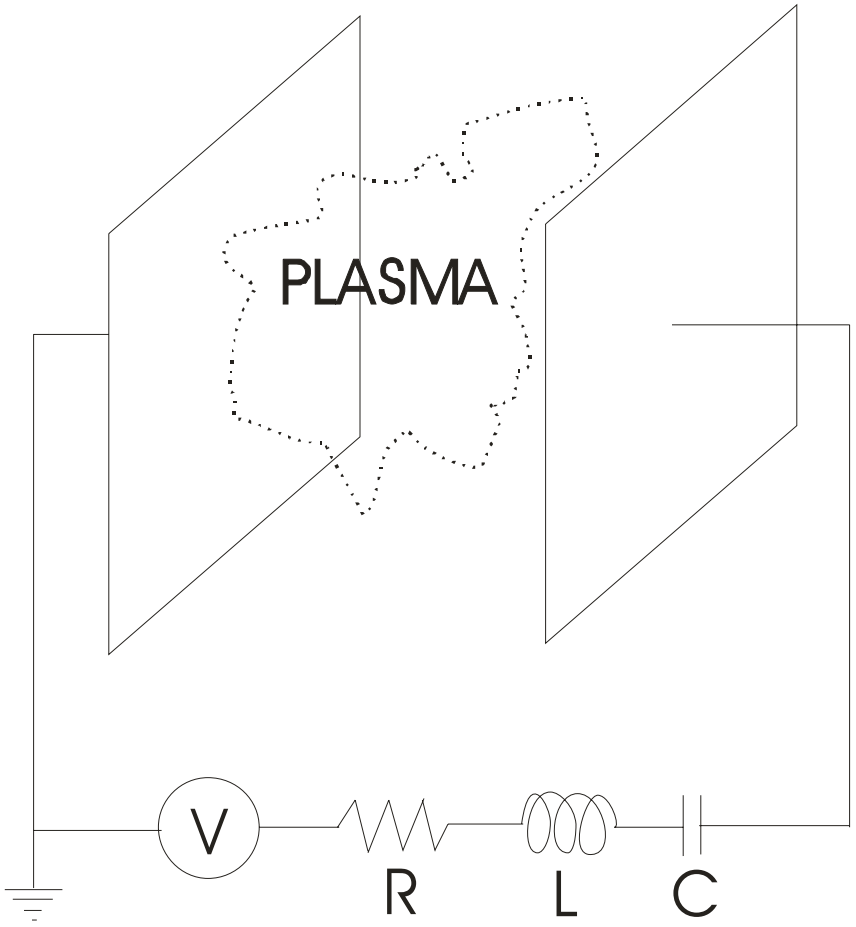

Figure 22. A plasma in series with an RLC circuit.

In general, the conductors of a plasma device system are not held at an independent potential but may interact with the plasma and an external circuit. The plasma serves as a conducting medium that may deposit charge on electrodes and is driven by their time-dependent potential. A bounded plasma is illustrated in Figure 22. In order to model the electrostatic behavior of a plasma correctly, the circuit and the plasma must be solved in a coupled manner.

It is possible to model an arbitrary system of conductors and circuit elements in conjunction with a plasma through the discretization of Maxwell's equations (*Thomas et al., 1994*). However, in general it is necessary to explicitly model the devices external the plasma including geometric details. For the application of an electrostatic code, another approach is taken. The standard equations for an external circuit are solved in conjunction with Poisson's equation for electrostatics using the assumption that a conductor is at a constant potential and the standard circuit equations apply.

Assume that a system of conductors bounding a plasma includes one driven and one grounded electrode as shown in Figure 22. The potential on the driven conductor is unknown and is a function of circuit and plasma parameters. Other conductors with explicitly specified potentials may be present, though it is assumed that their potentials are independent of the plasma and the circuit, as if connected to an ideal battery with a very thin wire. The potential on the grounded conductor is asserted to be zero so that at least one Dirichlet boundary condition is present. To obtain the potential on the driven conductor, it is useful to apply Gauss's law:

$$\varepsilon_o \oiint_S \mathbf{E} \bullet d\mathbf{S} = -\varepsilon_o \oiint_S \nabla\Phi \bullet d\mathbf{S} = \iiint_V \rho dV + \oiint_S \sigma dS = Q \tag{2.107}$$

where, Q is the total charge enclosed in the volume of interest (in Coulombs) and it is assumed that the permittivity in the volume is that of free space, and σ is the surface charge density on the conductor.

The surface charge density may be associated with the boundary faces or the boundary nodes. It is convenient to associate the surface charge density with the nodes for the node-based scheme described in the development of the finite volume approach. A semi-discrete expression for Gauss's law is available directly from the finite volume discretization of Equation (2.82):

$$\varepsilon_o \left[E_{N,i} A_{N,i} + \sum_k (\Phi_i - \Phi_k) \frac{A_{i,k}}{L_{i,k}} \right] = Q_{(plasma)i} + \sigma_i A_{(boundary)i} \tag{2.108}$$

The expression here is evaluated at the Voronoi volume corresponding to boundary node *i*. The outward electric flux due to Neumann boundary conditions into the node's corresponding Voronoi volume is designated by $E_{N,i}A_{N,i}$, if any. The sum is taken over all neighbors of node *i*. There will be no contribution from neighbor nodes *k* on the same conducting boundary since their potential will be the same as potential at *i*. The boundary area associated with node *i* is $A_{(boundary)i}$, and $Q_{(plasma)i}$ is the charge due to the plasma weighted to node *i*:

$$Q_{(plasma)i} = \iiint_V \rho dV \tag{2.109}$$

The electric field inside a perfect conductor in electrostatics is zero, so it is unnecessary to include a flux term that would correspond to flux into the conductor. This is equivalent to saying that all current in the driven electrode is perpendicular to the surface.

It is necessary to develop an expression that constrains the potential to be constant on a conductor in accordance with the principles of electrostatics.

The time variation of the total surface charge density (the surface charge density integrated over the conductor divided by its area) can be obtained from the law of charge conservation following *Vahedi and DiPeso,* (*1997*):

$$A\frac{d\sigma_T}{dt} = I(t) + Aj_{conv} \tag{2.110}$$

In the above, I is the external current, j_{conv} is the convected plasma current density arriving at the electrode, and A is the total area of the electrode:

$$A = \sum_{(boundary)i} A_{(boundary)i} \tag{2.111}$$

A discrete form of the charge conservation at the boundary which is first order accurate in time is following *Vahedi and DiPeso* (*1997*):

$$A(\sigma_T{}^t - \sigma_T{}^{t-1}) = Q^t - Q^{t-1} + Q^t_{conv} \tag{2.112}$$

The superscript integral counter t indicates the time step number. In Equation (2.112), Q is the total charge on the capacitor and Q_{conv} is the charge deposited on the electrode during the time interval (*t-1*, *t*). Using Equation (2.108) and summing over all the boundary nodes gives an expression for the total charge at the current time.

$$\sigma_T^t \sum_i A_{(boundary)i} = \sum_i \sigma_i{}^t A_{(boundary)i} = \sum_i \varepsilon_o [E_{N,i}{}^t A_{N,i} + \sum_k (\Phi^t{}_i - \Phi^t{}_k)\frac{A_{i,k}}{L_{i,k}}] - Q^t{}_{(plasma)i} \tag{2.113}$$

Applying charge conservation (Equation (2.112)), Equation (2.113) becomes

$$A\sigma_T^t = A\sigma_T^{t-1} + Q^t - Q^{t-1} + Q^t_{conv} = \sum_i \varepsilon_o [E^t{}_{N,i} A_{N,i} + \sum_k (\Phi^t{}_i - \Phi^t{}_k)\frac{A_{i,k}}{L_{i,k}}] - Q^t{}_{(plasma)i} \tag{2.114}$$

If we constrain the potential to be a constant value Φ_o for all boundary nodes i on the conductor, then Eq. (2.114) becomes

$$\varepsilon_o\left[\sum_i {E^t}_{N,i} A_{N,i} + \sum_k ({\Phi^t}_o - {\Phi^t}_k)\frac{A_{i,k}}{L_{i,k}}\right] = A\sigma_T^{t-1} + Q^t - Q^{t-1} + Q_{conv}^t + \sum_i {Q^t}_{(plasma)i} \quad (2.115)$$

$${\Phi^t}_o = \frac{\frac{1}{\varepsilon_o}[A\sigma_T^{t-1} + Q^t - Q^{t-1} + Q_{conv}^t + \sum_i {Q^t}_{(plasma)i}] + \sum_i\left[-{E^t}_{N,i} A_{N,i} + \sum_k {\Phi^t}_k \frac{A_{i,k}}{L_{i,k}}\right]}{\sum_i\sum_k \frac{A_{i,k}}{L_{i,k}}} \quad (2.116)$$

In general, the value of Q^t comes from the circuit equation of the external circuit and is a function of the potential Φ_o. In effect, the wall is treated as a single unknown node, with connections to all of the adjacent nodes and appropriate geometric quantities.

The linearity of Maxwell's equations allows the total field to be considered as contributions of fields from separate sources. This is the principle of linear superposition. Similarly, the electrostatic potential may be seen as the superposition of the potential due to the plasma charge density with zero boundary conditions, the potential due to an imposed the electric field, and the potential due to the electrodes.

$$\Phi^t = \left(\Phi_{plasma} + \Phi_{E-field} + \Phi_{electrodes}\right)^t \quad (2.117)$$

The potential due to the imposed electric field comes from Neumann boundary conditions. The potential due to the (driven and grounded) electrodes needs only to be solved initially using Laplace's equation in absence of any space charge. The potential on the driven electrode is normalized to unity, such that the potential

field at an arbitrary time due only to the potential drop from the driven electrode may be obtained as the initial potential field multiplied by a constant.

$$\Phi_i^{\,t} = \Phi_o^{\,t}\Phi_{NL,i} + \Phi_{plasma,i}^{\,t} \tag{2.118}$$

In this equation, Φ_{plasma} denotes the potential due to the volume (plasma) charge distribution, the imposed electric field, and independently biased conductors. The potential due to the driven conductor is $\Phi_o^{\,t}\Phi_{NL,i}$, where $\Phi_{NL,i}$ is the normalized time-independent potential profile obtained initially due to the driven and grounded conductors and $\Phi_o^{\,t}$ is the potential on the driven conductor at time t. If K independent external circuits are considered (with either a common ground or grounds specifically provided by constant Dirichlet boundary conditions) this equation becomes:

$$\Phi_i^{\,t} = \sum_{k=1}^{K} \Phi_{o,k}^{\,t}\Phi_{NL,ik} + \Phi_{plasma,i}^{\,t} \tag{2.119}$$

Note that Laplace's equation must be solved once for each driven electrode.

A value may be obtained explicitly for the driven electrode potential by substituting this solution for neighbors j of the electrode into the expression for potential from consideration of Gauss's law near the boundaries:

$$\Phi^t{}_o = \frac{\frac{1}{\varepsilon_o}[A\sigma_T^{t-1} + Q^t - Q^{t-1} + Q_{conv}^t + \sum_i Q^t{}_{(plasma)i}] + \sum_i \left[-E^t{}_{N,i} A_{N,i} + \sum_k \frac{A_{i,k}}{L_{i,k}} \Phi^t{}_{(plasma)k} \right]}{\sum_i \sum_k \frac{A_{i,k}}{L_{i,k}} (1 - \Phi_{NL,k})} \tag{2.120}$$

Once the potential on the conductor is known, the total charge on the conductor, $A\sigma_T^t$, may be calculated from Gauss's law (Equation (2.108). The new value of charge on the capacitor may be obtained from the discretized Kirchoff's current loop law:

$$Q^t = A(\sigma_T^t - \sigma_T^{t-1}) + Q_c^{t-1} - Q_{conv}^t \tag{2.121}$$

Floating conductor

A conducting boundary is floating if it cannot exchange charge via an external circuit. This is equivalent to an open circuit. Floating boundary conditions are useful in modeling electrostatic (Langmuir) probes, spacecraft charging, and other phenomenon of engineering interest.

A floating conductor may be modeled as above by simply removing the Q^t terms. Then Equations (2.114) and (2.120) become

$$A\sigma_T^t = A\sigma_T^{t-1} + Q_{conv}^t = \sum_i \left\{ \varepsilon_o [E^t{}_{N,i} A_{N,i} + \sum_k (\Phi_i - \Phi_k) \frac{A_{i,k}}{L_{i,k}}] - Q^t{}_{(plasma)i} \right\} \tag{2.122}$$

$$\Phi^t{}_o = \frac{\frac{1}{\varepsilon_o}[A\sigma_T^{t-1} + Q_{conv}^t + \sum_i Q^t{}_{(plasma)i}] + \sum_i \left[-E^t{}_{N,i} A_{N,i} + \sum_k \frac{A_{i,k}}{L_{i,k}} \Phi^t{}_{(plasma)k} \right]}{\sum_i \sum_k \frac{A_{i,k}}{L_{i,k}} (1 - \Phi_{NL,k})} \tag{2.123}$$

Capacitative Circuit

A simple type of external circuit useful in plasma simulations is an ideal voltage source and capacitor in series with the plasma with a grounded electrode.

This circuit type is useful for analysis of capacitative discharges (*Vahedi and DiPeso, 1997*). The circuit analysis presented above is applied here to the capacitative circuit. The voltage across the capacitor is available from Kirchhoff's voltage loop law:

$$V_c = V(t) - \Phi_o \tag{2.124}$$

In this equation, V_c is the voltage across the capacitor, $V(t)$ is the time-dependent ideal voltage source, and Φ_o is the potential at the driven electrode. The charge on the capacitor, Q^t, is (*Vahedi and DiPeso, 1997*)

$$Q^t = CV_c = C(V(t) - \Phi_o) \tag{2.125}$$

Equation (2.120) for the potential Φ_o becomes

$$\Phi_o = \frac{\frac{1}{\varepsilon_o}[A\sigma_T^{t-1} + CV(t) - C\Phi_o - Q^{t-1} + Q_{conv}^t + \sum_i Q_{(plasma)i}] + \sum_i \left[-E_{N,i}A_{N,i} + \sum_k \frac{A_{i,k}}{L_{i,k}} \Phi_{(plasma)k} \right]}{\sum_i \sum_k \frac{A_{i,k}}{L_{i,k}} (1 - \Phi_{NL,k})} \tag{2.126}$$

$$\Phi_o = \frac{\frac{1}{\varepsilon_o}[A\sigma_T^{t-1} + CV(t) - Q^{t-1} + Q_{conv}^t + \sum_i Q_{(plasma)i}] + \sum_i -E_{N,i}A_{N,i} + \sum_j \frac{A_{ij}}{L_{ij}} \Phi_{(plasma)j}}{\frac{C}{\varepsilon_o} + \sum_i \sum_j \frac{A_{ij}}{L_{ij}} (1 - \Phi_{NL,j})} \tag{2.127}$$

Series RLC Circuit

Many plasma discharges, including the pulsed plasma thruster, are initiated by and coupled with a series RLC circuit. The equation for an RLC circuit with a voltage drop Φ_o across a plasma is

$$L\frac{dI}{dt} + RI + \frac{1}{C}\int_0^t Idt = V(t) - \Phi_o \tag{2.128}$$

where, *V(t)* is the applied voltage. This equation may also be cast in terms of the charge on the capacitor *Q*:

$$L\frac{d^2Q}{dt^2} + R\frac{dQ}{dt} + \frac{Q}{C} = V(t) - \Phi_o \tag{2.129}$$

It is desirable to obtain a backwards difference expression in order to evaluate this circuit. A representation of the derivatives of interest is (taken from *Verboncoeur et al., 1993*):

$$\left(\frac{dQ}{dt}\right)^t = \frac{3Q^t - 4Q^{t-1} + Q^{t-2}}{2\Delta t} \tag{2.130}$$

$$\left(\frac{d^2Q}{dt^2}\right)^t = \frac{2Q^t - 5Q^{t-1} + 4Q^{t-2} - Q^{t-3}}{\Delta t^2} \tag{2.131}$$

These expressions are second order accurate in time (*Verboncoeur et al., 1993*). A slightly more accurate second order expression for the second derivative may be obtained by substituting $(dQ/dt)^t$ for *Q* into the finite difference expression for the first derivative, but this results in a five-point expression. It is generally preferable to use as few points as possible in a finite difference scheme unless significant gains in accuracy are achieved.

The four-point finite difference equation for the RLC circuit may be solved to obtain the current charge on the capacitor as a function of the driven electrode potential, voltage source, and charge on the capacitor at previous time steps. This is given by

$$Q^t = \frac{V(t) - \Phi_o + (\frac{5L}{\Delta t^2} + \frac{4R}{2\Delta t})Q^{t-1} - (\frac{4L}{\Delta t^2} + \frac{R}{2\Delta t})Q^{t-2} + \frac{L}{\Delta t^2}Q^{t-3}}{\frac{2L}{\Delta t^2} + \frac{3R}{2\Delta t} + \frac{1}{C}} \qquad (2.132)$$

The equation for the potential on the driven electrode is

$$\Phi_o = \frac{1}{\frac{1}{\varepsilon_o}\left[\frac{1}{\frac{2L}{\Delta t^2} + \frac{3R}{2\Delta t} + \frac{1}{C}}\right] + \sum_i \sum_j \frac{A_{ij}}{L_{ij}}(1 - \Phi_{NL,j})} \cdot$$

$$\left[\frac{1}{\varepsilon_o}\left(A\sigma_T^{t-1} + \frac{V(t) + \left[\frac{5L}{\Delta t^2} + \frac{4R}{2\Delta t}\right]Q^{t-1} - \left[\frac{4L}{\Delta t^2} + \frac{R}{2\Delta t}\right]Q^{t-2} + \frac{L}{\Delta t^2}Q^{t-3}}{\frac{2L}{\Delta t^2} + \frac{3R}{2\Delta t} + \frac{1}{C}} - Q^{t-1} + Q^t_{conv} + \sum_i Q_{(plasma)i}\right) + \sum_i -E_{N,i}A_{N,i} + \sum_j \frac{A_{ij}}{L_{ij}}\Phi_{(plasma)j}\right] \qquad (2.133)$$

Initialization of External Circuits and Stability Considerations

For circuits dependent on more than one previous value of charge on the capacitor, it is necessary to obtain these values in starting the simulation.

A method was adopted from *Verboncoeur et al.* (*1993*) for obtaining the initial circuit parameters. The circuit equation is solved for the potential on the electrode in absence of plasma in the region. If the method is stable, the initial conditions will be damped with time (*Verboncoeur et al., 1993*).

External Circuits and Neumann Boundary Conditions

The capacitance matrix concept (*Haus and Melcher, 1989; Jackson, 1999*) used here is typically presented for a system of conductors using only Dirichlet

boundary conditions. It is possible to implement Neumann boundary conditions as well (*Vahedi and DiPeso, 1997*), but care should be exercised in doing so.

The method for circuit solution implemented here uses only the no-flux Neumann boundary conditions such that the imposed electric field normal to the boundary is zero ($E_{N,i}=0$). The implementation of the no-flux condition requires no additional computational effort, only that both Laplace's equation for the capacitance matrix and Poisson's equation for plasma potential are solved with the no-flux Neumann boundary condition (*Vahedi and DiPeso, 1997*). As this is trivially implemented in this finite volume approach (zero is added to the right hand side of the appropriate linear equation), the method can be used without alteration.

It can be seen that the implementation of the no-flux condition is done trivially for the capacitance matrix method for circuit electrodes. When the normalized potential profile (obtained from Laplace's equation) is multiplied by the value of the potential at the current time, the effect is that the gradient of the potential field is multiplied by this value. As the slope of the potential normal to the no-flux boundary is zero, it will remain zero when multiplied by any number. The total potential profile is obtained from the sum of all potential profiles (including that due to the plasma). As each potential profile will be flat normal to the no-flux surface, their sum will also be flat normal to this surface. Thus the no-flux condition is trivially satisfied.

2.4.8 Validation of the Electrostatic Solver

Electrostatics is a well-studied field. Many analytic solutions are available for comparison, both with and without free charges. In order to validate the electrostatic solver, comparison is made to both types of these cases.

One classic problem is a grounded conducting sphere immersed in a uniform electric field. *Jackson* (*1999*) gives the potential far from a conducting sphere at the origin as

$$\Phi = -E_o(r - \frac{a^3}{r^2})\cos\theta \tag{2.134}$$

where, E_o is the imposed electric field strength, a is the radius of the sphere (in meters), r is the distance from the sphere, and θ is the angle from the imposed electric field vector.

This problem was simulated in a cylindrical domain 7 meters long and 7 meters in radius. The sphere radius was one meter. About 60,000 elements were used to discretize the domain, with spacing concentrated near the sphere where high gradients were expected as shown in Figure 23. The analytic solution is plotted in Figure 24 and the numerical result in Figure 25. Figure 26 plots the absolute value of the analytic minus the numerical results. Figure 27 illustrates the electric field as calculated using the control volume approach, and Figure 28 illustrates the orthogonality of the potential and electric field lines in the vicinity of the sphere.

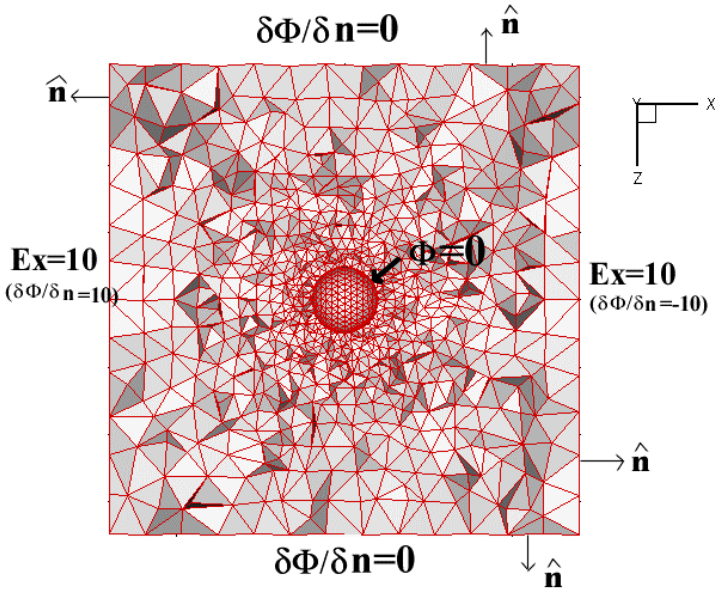

Figure 23 Domain and boundary conditions used for grounded sphere in imposed electric field problem.

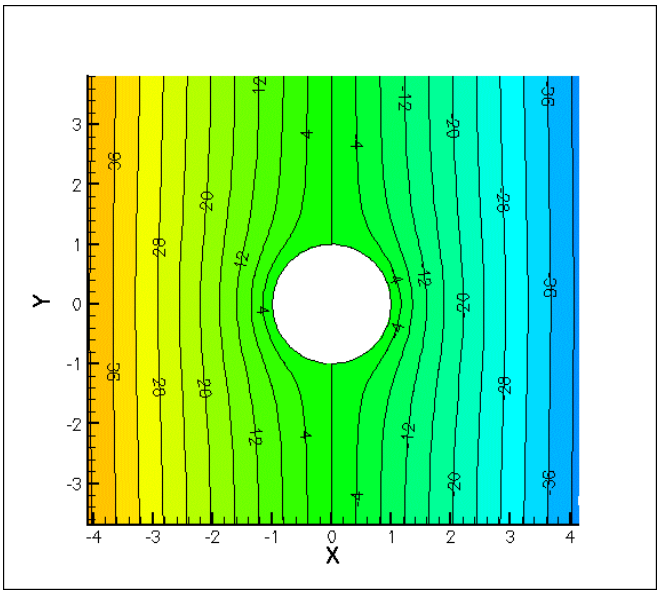

Figure 24. Analytic solution for potential around a grounded sphere in a uniform electric field (from *Jackson, 1999*)

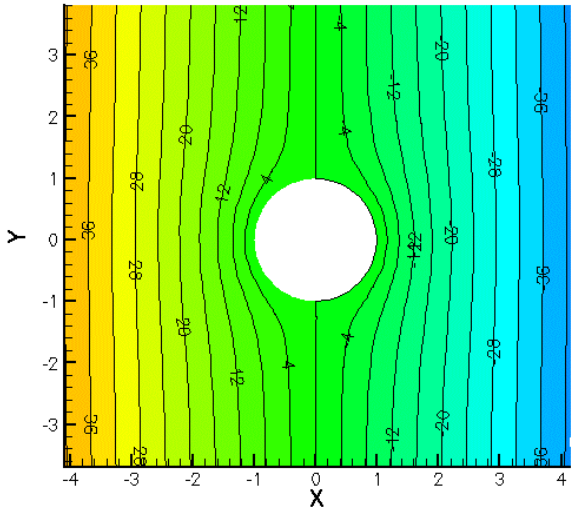

Figure 25. Computed solution for potential around grounded sphere.

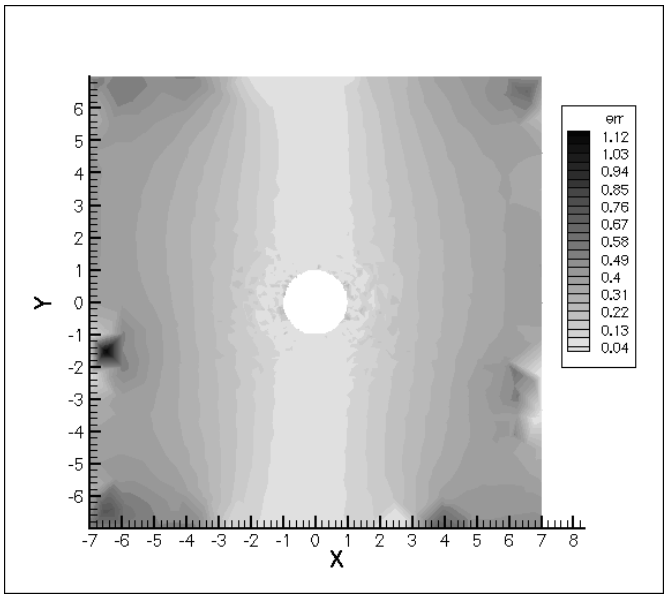

Figure 26. Absolute value of error in volts.

In general, agreement was excellent between calculated and numeric potential. The values of electric field at the boundaries also matched the prescribed conditions. Slight disagreement is shown in Figure 26 near the boundaries (though small compared to the value of potential there), but this is due to the imposition of a finite domain on what is, in principle, an unbounded problem. This example illustrates the validity of the electrostatic solver for a variety of boundary conditions.

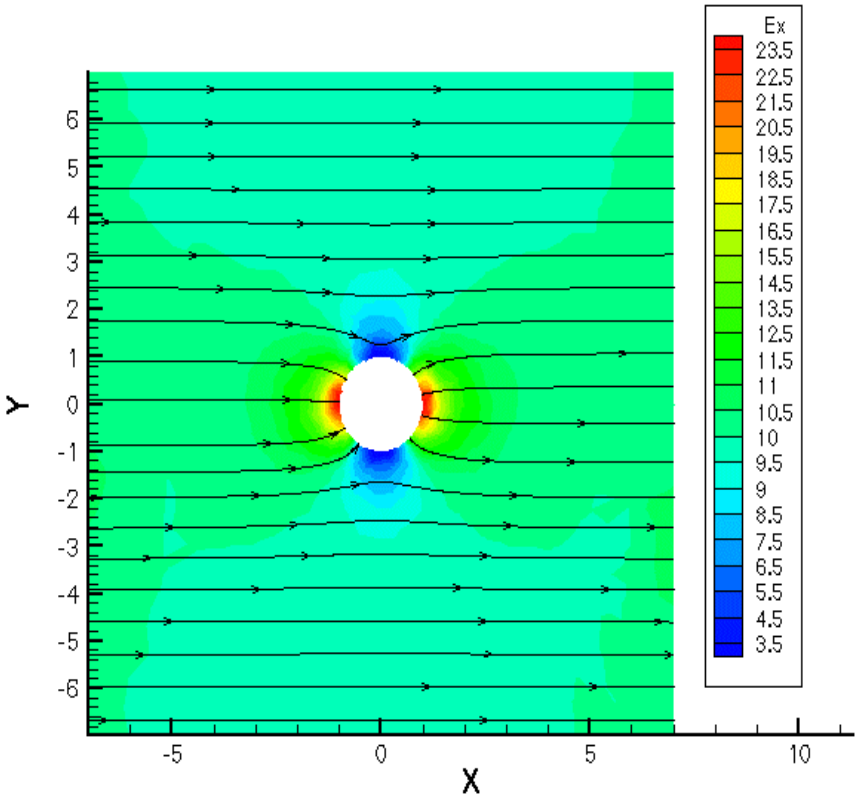

Figure 27. Electric field lines and contour plot of x-component of electric field (V/m). The discrepancy near the boundary may be caused by sensitivity to boundary conditions and poorer resolution in this region, and does not seems to affect the general field shape.

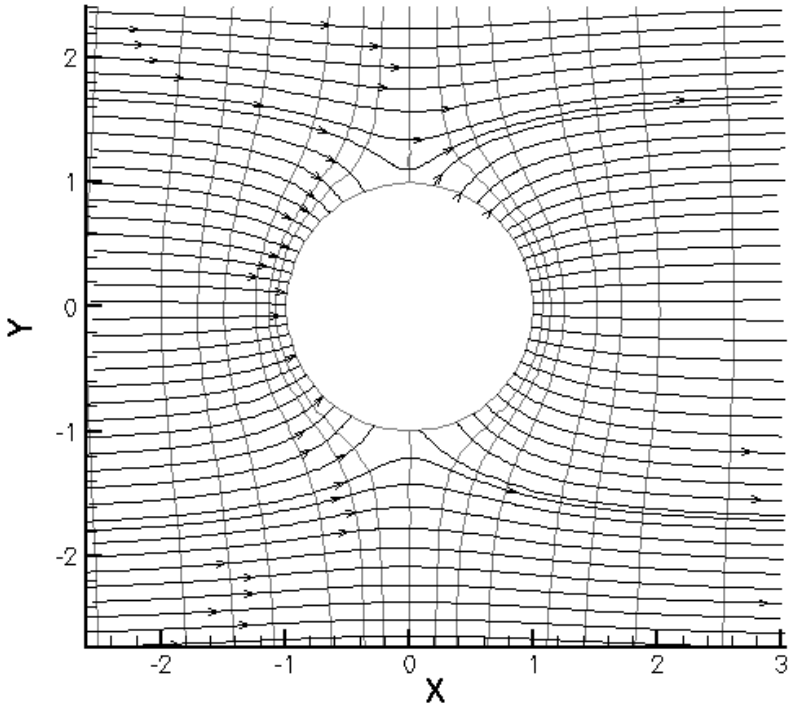

Figure 28. Close-up showing orthogonality of electric field lines and potential contours. The spacing between electric field lines and potential contours is not to scale.

Another problem of interest is that of a uniform charge distribution between two infinite grounded conducting plates at $x = -l/2$ and $x=l/2$. Poisson's equation in one dimension is:

$$\frac{d^2\Phi}{dx^2} = -\frac{en_i}{\varepsilon_o} \tag{2.135}$$

An exact formulation proceeds from the imposition of boundary conditions. Imposing $\Phi=0$ at $x = -l/2$ and $x = l/2$ and $d\Phi/dx=0$ at $x=0$ (from symmetry) leads to an analytic formulation for the potential:

$$\Phi = \frac{1}{2}\frac{en_i}{\varepsilon_o}\left[\left(\frac{l}{2}\right)^2 - x^2\right]$$

(2.136)

This problem was simulated with the electrostatic solver in a cylindrical domain and the results compared to the analytic formulation. The distance of plate separation was 0.1 m and the ion number density (n_i) was 10^{16} m^{-3}, using parameters similar to *Lieberman and Lichtenberg* (*1994*). One million singly-charged particles were used on grids ranging from 12,000 to 25,000 cells. On average, about 50 particles resided in each cell, which is a similar number to simulation parameters. Variation in the number of particles per cell to as low as about 10 did not seriously affect the outcome. The charge weighting used in this and subsequent simulations is based on linear Lagrange polynomials, as nearest grid point weighting proved inadequate. Figure 29 illustrates the potential contours with the projection of the background mesh shown. Figure 30 shows the potential as a function of *x* and *y* with contour levels.

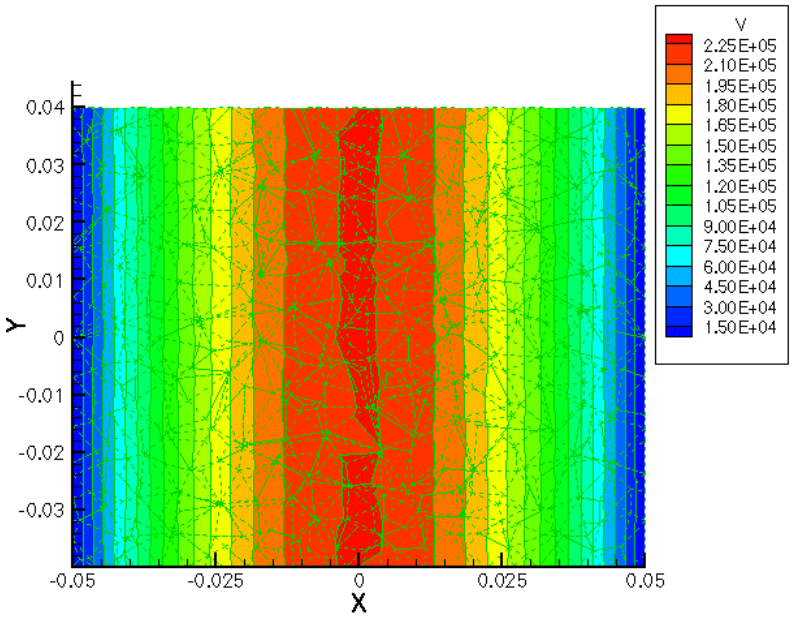

Figure 29. 2-D view of potential lines and background mesh for uniform charge distribution between infinite grounded conducting plates.

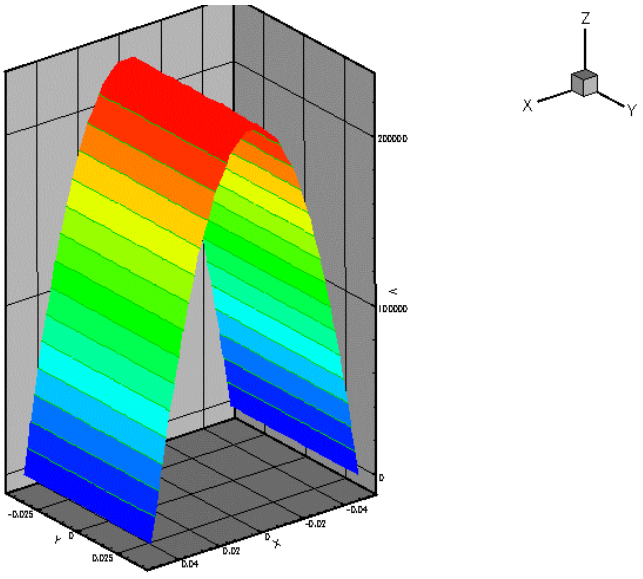

Figure 30. Potential between two infinite grounded conducting plates for a uniform charge distribution.

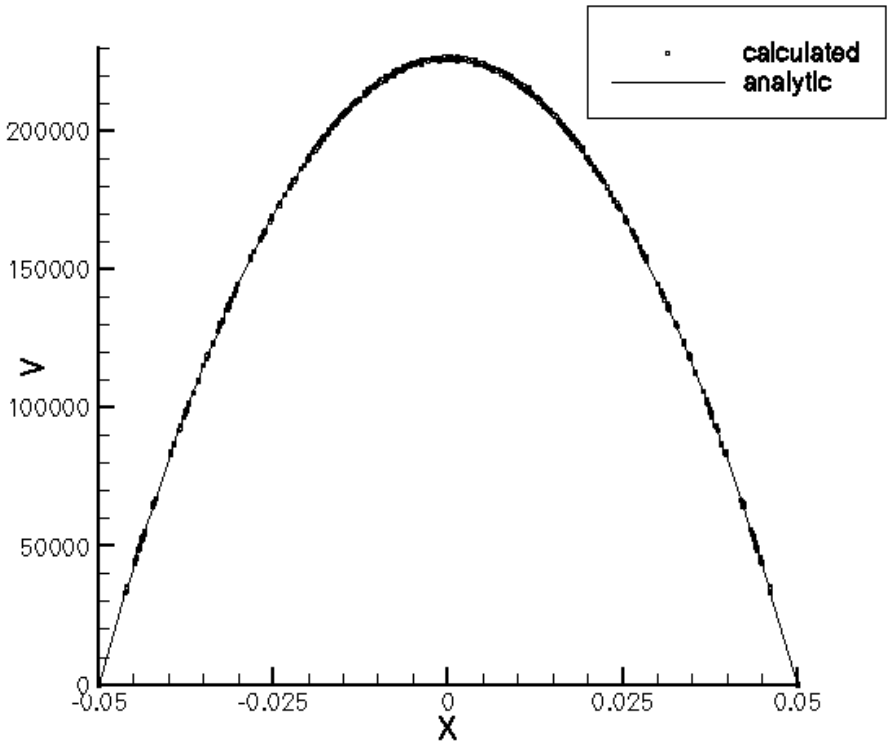

Figure 31. Comparison between calculated and analytic potential for a uniform charge distribution between two infinite parallel grounded conducting plates. (X: distance (m); Y: volts)

This simulation assesses several important aspects of the electrostatic solver. The general accuracy of the algorithm may be seen through the good comparison with analytic data in Figure 31, as well as the accuracy of the boundary conditions for a grounded exterior boundary and the no-flux condition. Also, the charge weighting routine was verified and shown to be robust. The only location where error was numerically considerable compared to the voltage was near the conductor boundary, where the gradient of the potential is large. Use of a smaller characteristic spacing near this boundary would have corrected for this error. Deviation from smoothness

shown on the two-dimensional mesh cross-section is due to the interpolation algorithm of Tecplot and is present in both numerical and analytic data.

Particle weighting and loading procedures and discretization scale is assessed in the next simulation involving the monotonic decay of potential between two conductors. This simulation illustrates the importance of using a discretization smaller than the Debye length, as well as the need for improved weighting procedures. It is known (*Birdsall, 1991*) that even a Maxwellian distribution may be numerically unstable using a cell length h such that $\left(\lambda_{De}/h\right)\tilde{<}0.3$. The Debye length is the scale over which significant charge separations may be seen and is the characteristic length scale of a plasma dominated by electrostatic interaction. For a plasma in equilibrium, the Debye length is given as (*Lieberman and Lichtenberg, 1994*)

$$\lambda_{De} = \left(\frac{\varepsilon_o T_e}{e n_o} \right)^{1/2} \tag{2.137}$$

where, n_o is the bulk plasma density. For singly ionized species and quasi-neutral plasma, $n_o=n_e=n_i$.

A simulation domain similar to the interior of the LES-6 PPT (*Vondra, 1970*) was used. The two opposing electrodes were set 3.0 cm apart, one biased to 100 V and the other grounded. No-flux boundary conditions were used on remaining domain walls. An equal number of electrons and positive ions were randomly distributed throughout the domain such that the plasma should be neutral everywhere. The spacing value used in the discretization of the domain was 1.14×10^{-3} m.

While the velocity components are not important in this simulation (as only the initial electric and potential fields are desired), the Debye length was calculated according to an assumed electron temperature of 10 eV. It is noted that if the voltage drop across the electrodes was of the order of that of the plasma electron temperature, a much more detailed resolution would be necessary as the thermal noise would be of the order of the potential of interest. A minimum of 15 particles per cell was used.

Two different bulk plasma densities were used: 1.77×10^{15} and 1.0×10^{16} m^{-3}. This corresponds to Debye lengths at electron temperatures of 10 eV of 5.68×10^{-4} m and 2.34×10^{-4} m, respectively. The discretization length was 2.0 and 4.9 times larger than the Debye length. Though normally it is desirable to use values of discretization spacing smaller than Debye length, these values were chosen to numerically characterize the error induced by using too large of a spacing value.

For the case where a spacing value twice the Debye length is used, the potential shown in Figure 32 drops evenly over the domain and the electric field lines are such that a physical simulation could progress with these initial conditions. For the case where the discretization spacing is 4.9 times the Debye length, the potential shown in Figure 33 does not drop evenly and considerable error is seen in the electric field lines. An analytically neutral reference (no particles) is shown in Figure 34. While the temperature used (10 eV) is arbitrary, the case where the Debye length for the 1.0×10^{16} m^{-3} case is set to equal the Debye length of the 1.77×10^{15} m^{-3} case illustrates the context of this temperature. The electron temperature for the first case would be equal to 56.4 eV. Since the voltage drop over the domain is 100 V,

statistical fluctuations in electron behavior for a temperature of 56.4 eV would be considerable. In order to properly resolve this case with the existing implementation, it is desirable to use a smaller discretization scale and many more particles. If it is important to load particles such that no biases are introduced, the quiet start method (*Birdsall, 1991*) may be used. The quiet start method produces a phase space that is initially ordered. An improved weighting procedure would also improve accuracy considerably.

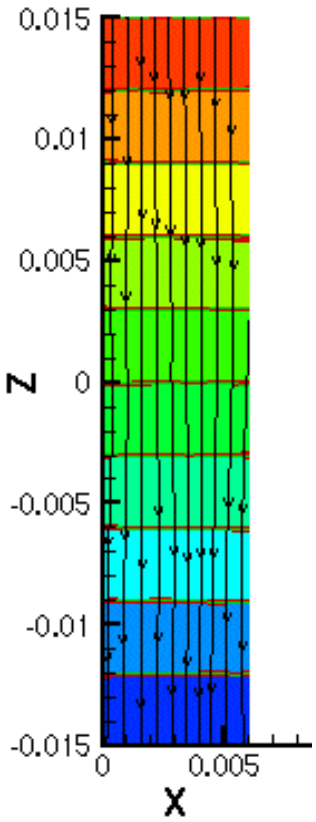

Figure 32. Potential contours and electric field lines for a discretization spacing of twice the Debye length. Contours shown every 10 V.

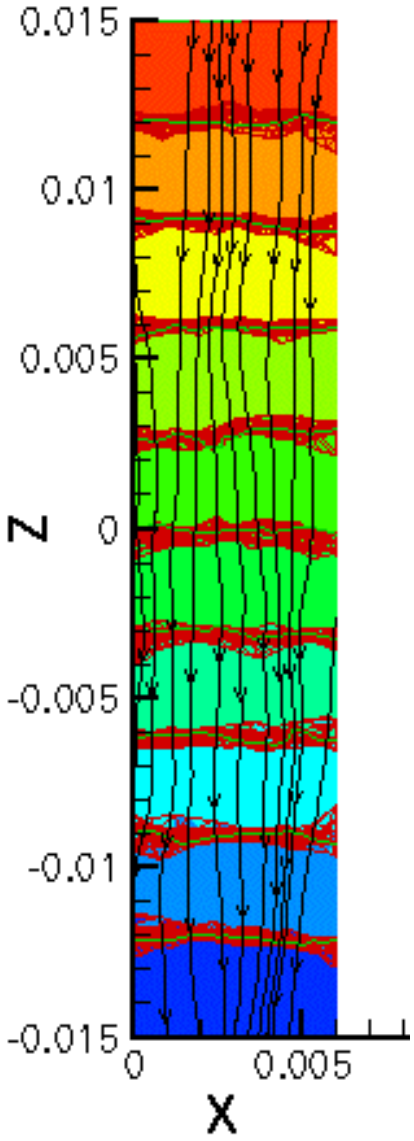

Figure 33. Potential contours and electric field lines for a discretization of 4.9 times the Debye length. Contours shown every 10 V.

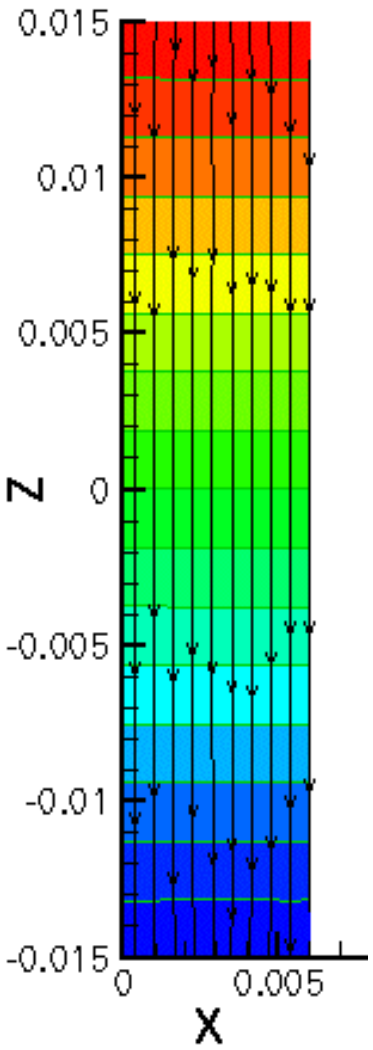

Figure 34. Potential contours and electric field lines with no charged particles (analytically neutral). Contours are shown every 6.25 V..

Though these simulations possess symmetries not found in fully three-dimensional problems, the unstructured solver is unbiased by these symmetries and the validation provided by these examples can be considered general. Few fully three-dimensional analytic solutions exist for electrostatic problems.

Chapter 3

DSMC and PIC Simulations

Gasdynamic thrusters are considered for micropropulsion for the role of attitude control as well as primary propulsion. These devices derive their thrust from thermal energy in the plenum being transformed to kinetic energy as the gas expands through the nozzle. These neutral thrusters may use a cold gas for simplicity, or derive additional energy from electric heating or exothermic chemical reactions. The transformation of thermal energy into directed energy his is most often accomplished with a converging-diverging nozzle.

In this chapter we present simulations using the DSMC/PIC code. The internal and external flow of the Gravity Probe-B thruster prototype is simulated and compared with data from *Boyd et al.* (*1994*a*, 1994*b*)*. Rothe's nozzle was simulated at low pressures. A two-dimensional planar MEMS nozzle was simulated and compared to DSMC simulations on structured meshes. A three-dimensional MEMS nozzle was simulated to assess the effect of side walls. To assess the PIC code, high voltage sheath formation was simulated.

3.1 Gravity Probe-B Thruster Prototype

The Gravity Probe-B (GP-B) thruster prototype is described by *Jafry and Vanden Beukel* (*1992*). Mass flow rates for this thruster range from 0.012-3.6 mg/s corresponding to thrust forces from 0.02 to 4.5 mN and Knudsen numbers ranging

from 1.1 and 0.01, respectively. The experiment obtained mass flux profiles via a mass spectrometer in a vacuum facility. The mass flux profiles were normalized to centerline flow at three points in the plume in angular increments of 10 degrees. The GP-B thruster prototype was numerically modeled using the DSMC method on structured grids by *Boyd et al.* (*1994*a*, 1994*b*)*. These DSMC calculations compared favorably with the mass spectrometer measurements of mass flux when diffuse reflection with full thermal accommodation was used as the surface interaction model for the nozzle wall. Cases were considered zero and finite background pressure corresponding to experimental conditions.

The unstructured DSMC code is used to model this nozzle for validation and also in order to study the characteristics of the rarefied nozzle flow. In addition, the GP-B thruster chamber is at the stagnation conditions at the chamber and therefore, it can serve as a case-study for proper application of subsonic boundary conditions in DSMC simulations. The mass flow rate considered is 0.012 mg/s = 1.2×10^{-8} kg/s. For this flow, stagnation conditions are taken from *Boyd et al*. as P_o=7 Pa and T_o=286K.

The surface is discretized with care taken to make sure the local mean free paths are greater than the average cell spacing. The computational grid is shown in Figure 35 and a close-up of the nozzle in Figure 36. The spacing of the grid interior to the nozzle is approximately 0.35 mm, which is about ten times smaller than the mean free path for equilibrium stagnation conditions. Several sizes of bounding cylinders external to the nozzle were used to obtain plume flow data. The largest

bounding cylinder was set to be 11 cm in radius and extended 20 cm from the nozzle. The grid spacing on this boundary is about 34 mm, which is much smaller than the mean free path of ~10 m evaluated using the background density. The calculations of *Boyd et al.* (*1994*a*, 1994*b) show that the density near the boundary for a domain of this size is essentially the same as the background value. The increase in spacing from the nozzle to the exterior domain was chosen as some approximation of flow diffusivity.

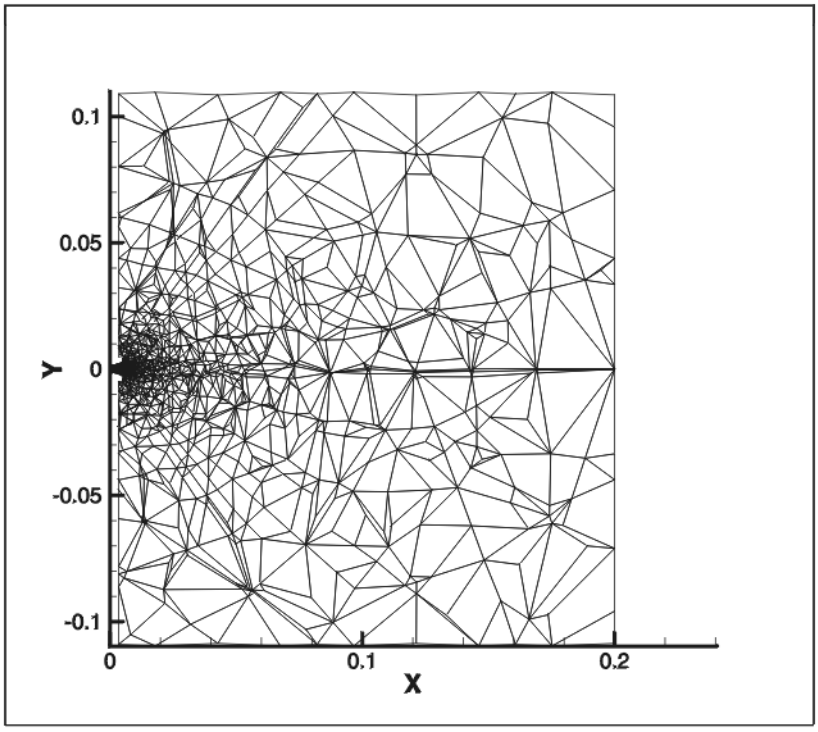

Figure 35. Cross-section of computational grid used for GP-B thruster simulations. Nozzle located at 0, 0.

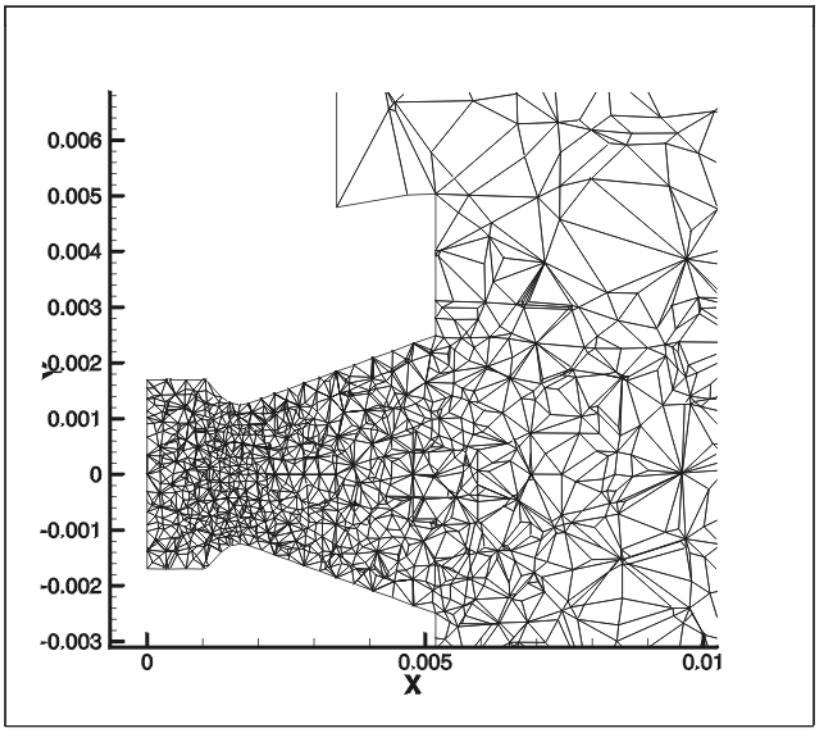

Figure 36. Cross-section of GP-B grid, close-up of nozzle region.

Boundary conditions were prescribed to the various surfaces. The exterior domain was set to a free boundary. The nozzle surfaces were set to be diffusely reflecting with a temperature equal to the stagnation temperature. To ensure a correct mass flow rate, two approaches were investigated. First, injection was implemented from an orifice in the back of the chamber wall. In this case boundary conditions were set such that particles could not leave across this orifice. The orifice size and injection flow velocity were set such that the correct mass flow rate was ensured. The second approach involved prescribing the back and side walls of the chamber as free boundaries, injecting with some finite stream velocity from the back wall and allowing diffusion across the side wall. The stream velocity was assigned such that

the incoming mass flux was close to the flux of particles escaping back across the boundary in an iterative process.

The first injection condition was found to match mass flow rate, far field temperature, and stagnation temperature. This injection condition also showed the unity Mach number contour intersecting the lip as well as other Mach contours intersecting the wall at appropriate locations. Number density was up to 50% higher than the stagnation value, but only at a small location near the injection orifice. Mach contours for this injection condition are shown in Figure 37 and are compared with the results of *Boyd et al.* In the bulk of the flow, the results compare well. The results shown in Figure 37 were obtained on a coarser grid than that shown in Figure 36, and resulting in the poor resolution of Mach contours near the wall. However, the chamber used matched stagnation conditions and the Mach contours of *Boyd et al.* better. Number density contours for this injection condition are shown in Figure 38.

The second injection condition matched mass flow rate as well. However, stagnation temperature was low (~265 vs. 286 K). The unity Mach contour did not intersect the lip but remained upstream of it. Other Mach contours did not compare well with the results of *Boyd et al.* Stagnation number density matched experimental data within numerical accuracy of the DSMC solver.

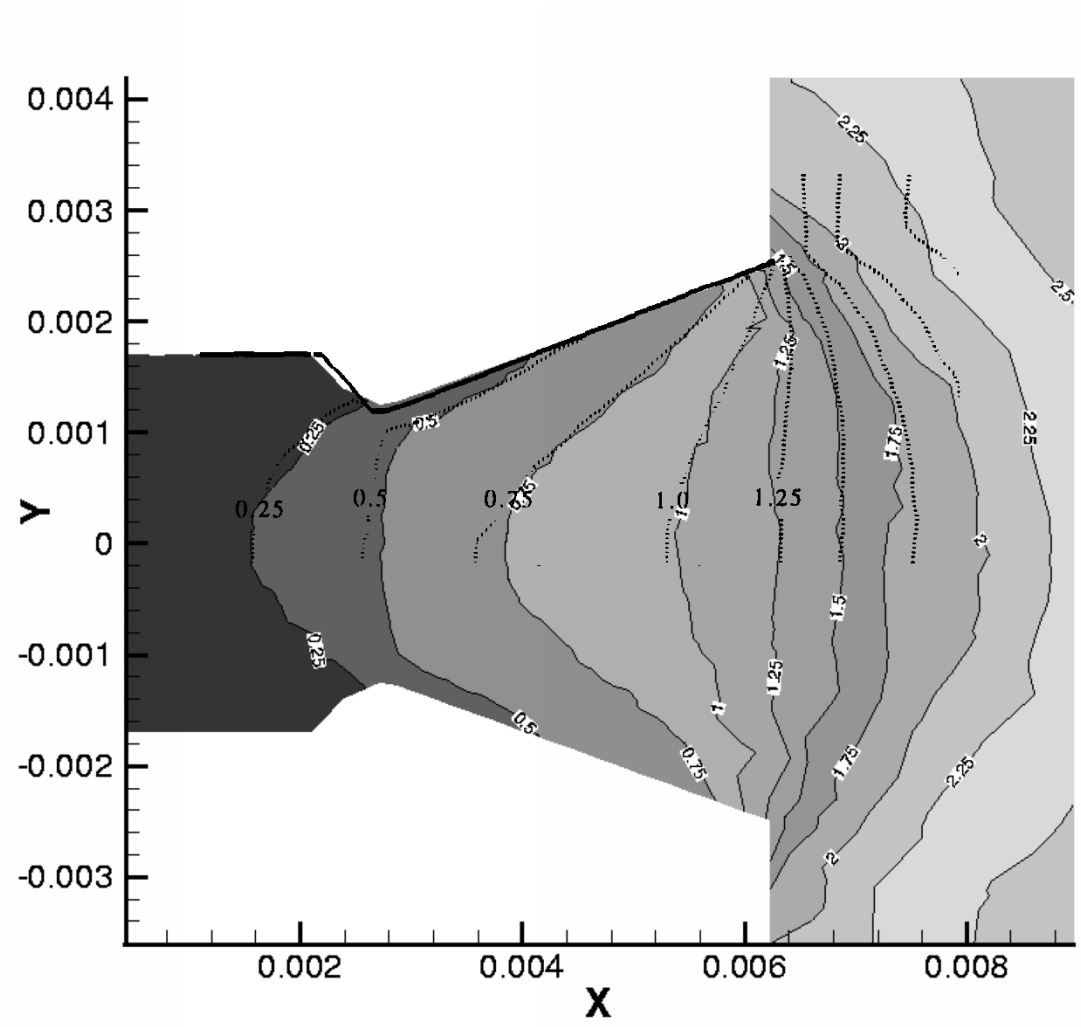

Figure 37. Gravity Probe-B Mach contour comparison. Current results: shaded contours; Boyd's: dotted lines.

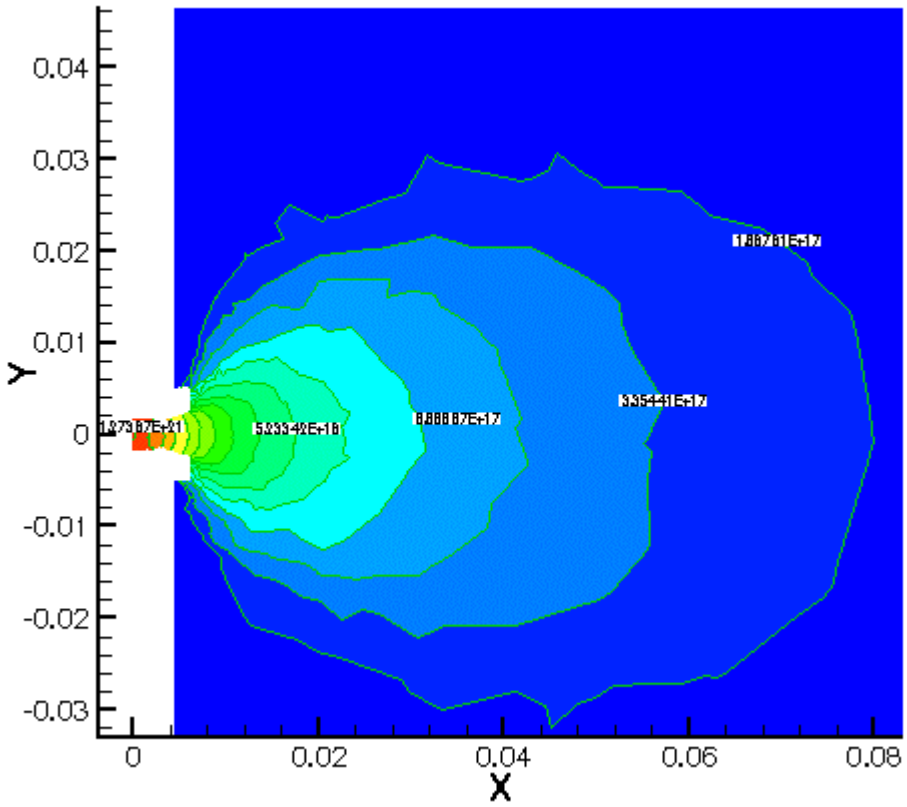

Figure 38. Plume shape (number density contours) for Gravity Probe-B prototype nozzle.

3.2 Rothe's Nozzle

Rothe (*1971*) presented experimental investigations of two graphite nozzles with throat diameters of 2.5 and 5.1 mm. Reynolds numbers ranged from 100 to 1500 with stagnation pressures as low as 80 Pa. Electron beams were used to determine the centerline rotational temperature and density as well as radial number density profiles. Rothe showed a qualitative difference in the behavior of flows as the Reynolds number dropped: for higher values of Re and chamber pressure, temperature decreased monotonically along the centerline; for lower values of Re,

temperature initially decreases but then rises again due to the dominance of viscous behavior. This result is important to micronozzles design, because viscous losses should be minimized to obtain maximum efficiency.

Rothe's 5-mm nozzle is modeled using our DSMC code on unstructured tetrahedral grids in order to validate the code and demonstrate the behavior of small nozzles at low Reynolds numbers. Only the lowest pressure (80.3 Pa) is simulated with a stagnation temperature of 300 K. The nozzle walls are modeled as diffusely reflecting and a constant value of relaxation collision number is used.

The simulation did not converged, even for a simulation time of 9.0×10^{-4} seconds. From the interim results, the formation of a viscous boundary layer on the diverging nozzle side-walls is observed. Contours of translational and rotational temperature are presented in Figures 39 and 40, respectively. Notice that the rotational temperature falls out of equilibrium with translational temperature due to the lack of collisions as the flow becomes increasingly rarefied. Number density contours are shown in Figure 41.

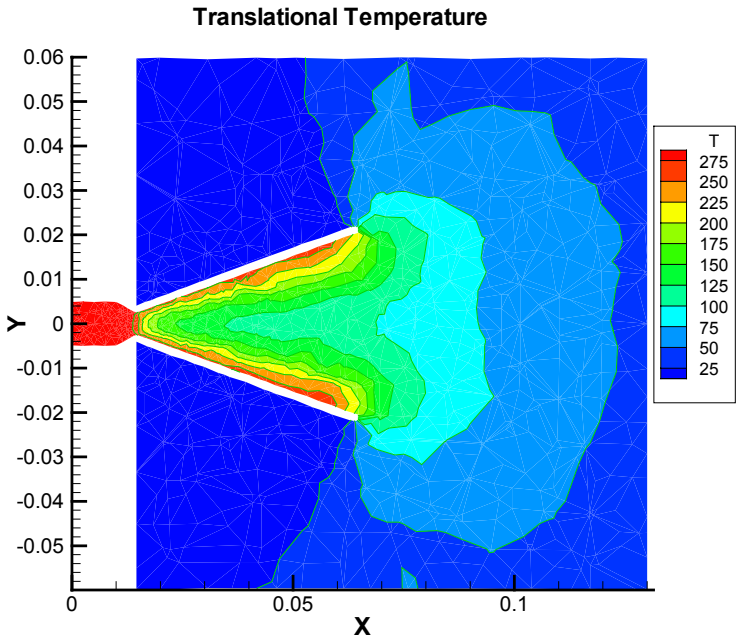

Figure 39. Translational temperature for Rothe's nozzle (K).The time is 9.0×10^{4} s.

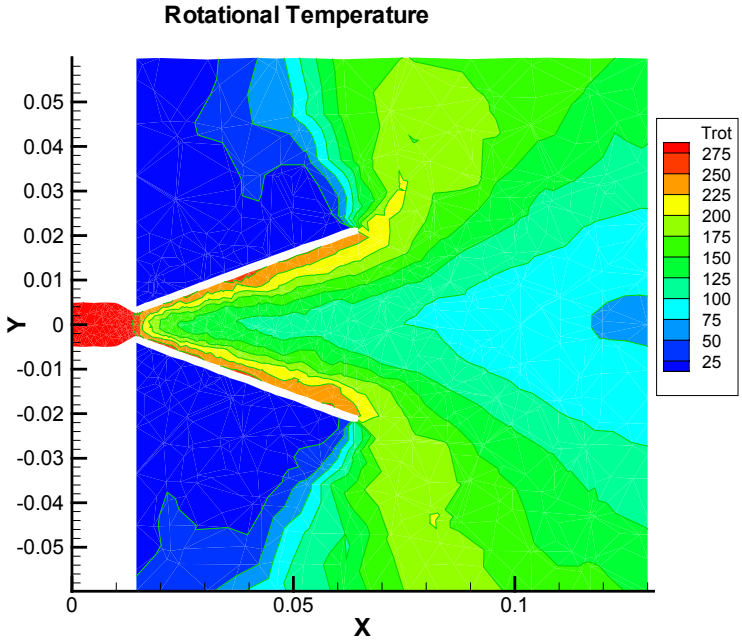

Figure 40. Rotational temperature for Rothe's nzzle (K). The time is 9.0×10^{-4} s.

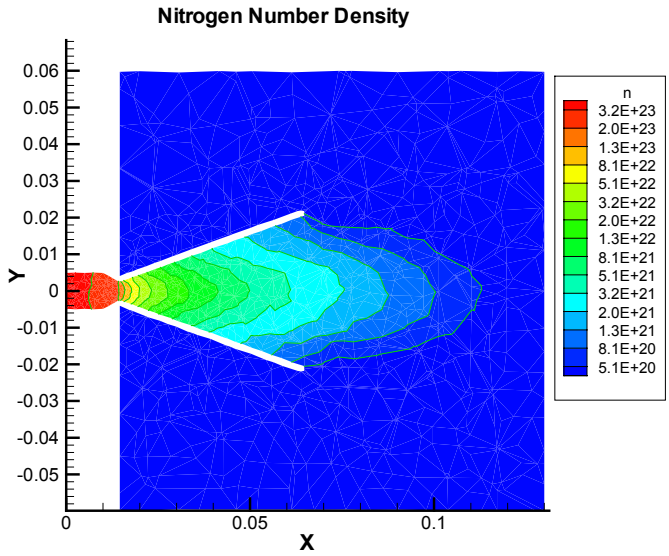

Figure 41. Nitrogen number density contours for Rothe's nozzle ($1/m^3$). The time of the simulation is $9.0x10^{-4}$ s.

3.3 Parabolic MEMS Nozzle

Piekos and Breuer (*1995, 1996*) presented two-dimensional DSMC studies of flows in micro pipes and a planar parabolic nozzle chosen to be similar in flow regime to MEMS micronozzles. The inlet condition for their studies was atmospheric and a perfect vacuum was assumed at the exit plane. The width of the throat was 15.4 microns and the nozzle walls were modeled as diffusely reflecting. Piekos and Breuer (*1995,1996*) illustrated important kinetic effects associated with flows in this flow regime, such as thermal and velocity slip at the wall.

This parabolic nozzle is modeled in two dimensions using our DSMC code on an unstructured grid. In order to model only half the flow field, the plane of symmetry was modeled as a specularly reflecting wall. The flow conditions are

identical to those used by Piekos and Breuer (*1995, 1996*). In our simulation we added a small surface outside of the nozzle that includes a lip.

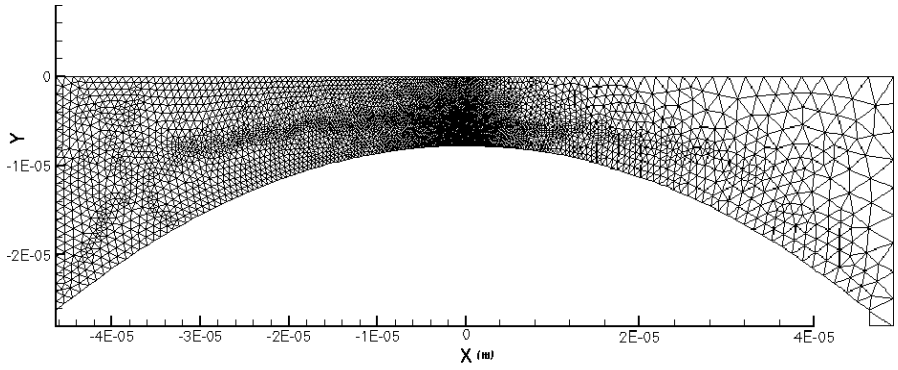

Figure 42. Two-dimensional grid used for modeling of planar parabolic nozzle. The chamber is located at left.

Results of the simulation on unstructured grids agree with the results of *Piekos and Breuer* (*1995, 1996*). A comparison of Mach number contours is shown in Figure 43. Disagreement in the chamber is probably due to insufficient simulation time in both models, though this should not significantly affect supersonic results.

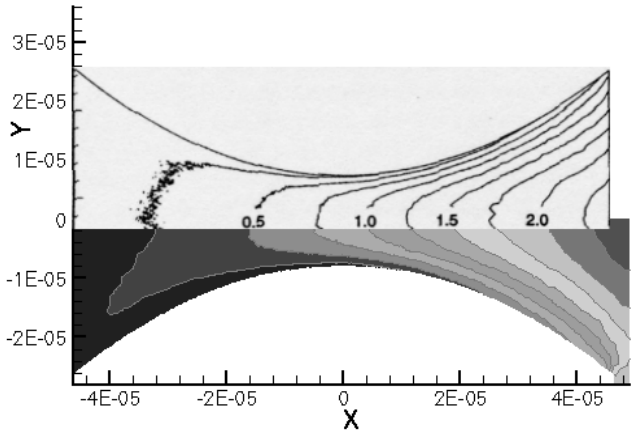

Figure 43. Comparison of Mach number contours. The results of Piekos and Breuer are shown above, and our results are shown below.

3.4 Planar MEMS Nozzle

Our direct simulation Monte Carlo code was applied to the study of a micronozzle manufactured using deep reactive ion etching (*Bayt and Breuer, 1998*). These nozzles are planar in profile with side walls binding the upper and lower surfaces. The ion etch is highly anisotropic with a depth of 308 microns. The flow field including the entrance was solved numerically by *Bayt et al*. (*1998*) using a Navier-Stokes finite volume code. These nozzles were tested experimentally at chamber pressures from 3.45×10^4 to 6.895×10^5 Pa with thrust on the order of milliNewtons. At lower pressures and corresponding mass flow rates, experimental results for the coefficient of discharge fall significantly below results predicted by the Navier-Stokes code. *Bayt et al*. (*1998*) attribute this to viscous losses due to increasing boundary layers on the side walls at low pressures, which were not modeled in the two-dimensional code.

The nozzle chosen for our DSMC study has a 7.1:1 expansion ratio and a 34 micron throat (*Bayt et al., 1998*). In order to assess sidewall effects, a fully three-dimensional discretization was performed of the domain of interest as shown in Figure 44. Advantage may be taken of planes of symmetry, which may be modeled as specularly reflecting surfaces, in order than only one quarter of the nozzle may be modeled. High grid quality may be ensured by taking advantage of the planar nature of the nozzle and mapping a two-dimensional triangular grid to a tetrahedral grid. In general, if this discretization is inadequate then adaptation may be used to further enforce grid spacing requirements.

A stagnation pressure of 3447.4 Pa, one-tenth of the lowest stagnation pressure studied by Bayt and Breuer (*Bayt, 1999; Bayt et al, 1998*), was chosen for the three-dimensional simulation. The use of this stagnation pressure represents the limit of very low thrust required for highly sensitive missions and results in a much faster computation time than higher pressures, as larger cells and a smaller number of computational particles may be used than for the high pressure case. As the Reynolds number is lower in this case than in Bayt and Breuer's study, sidewall effects will be heightened as the boundary layers will be thicker and more prominent as the viscous behavior becomes more important.

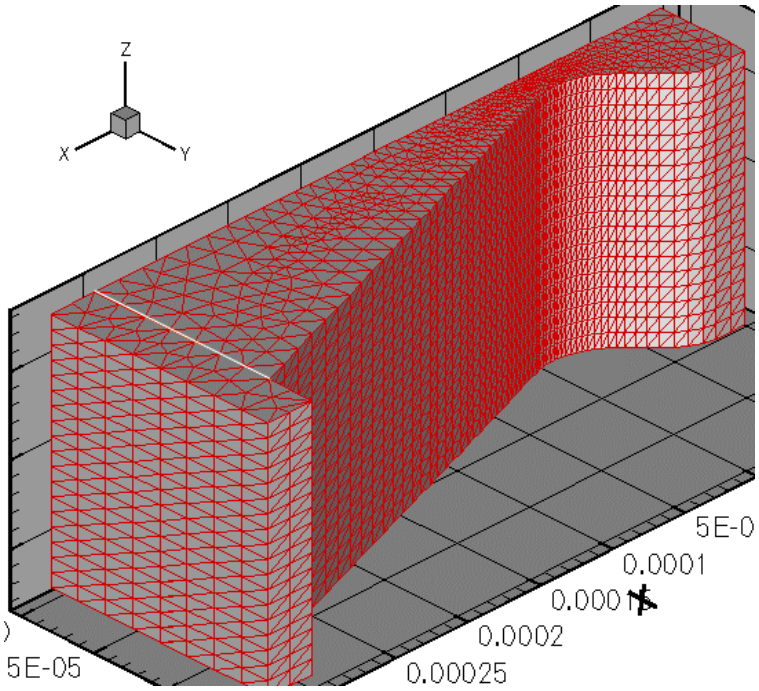

Figure 44. Computational mesh for MEMS 7.1:1 micronozzle (3447 Pa stagnation pressure). The white line designates the location of the lip.

The chamber in the simulation is not geometrically identical with the physical one, but is intended to give representative chamber conditions. The nozzle lip of the side wall is assumed to be infinitesimally thin in order to more easily construct the computational mesh.. The effect of the nozzle lip on flow parameters is well known but it is believed that this assumption will not significantly affect flow parameters internal to the nozzle except in the vicinity of the lip. In actuality, the nozzle lip of the MEMS thruster has considerable thickness.

The nozzle walls, including the side wall, are modeled as diffusely reflecting with a temperature equal to the stagnation temperature of the gas. The planes of symmetry are specularly reflecting. Particles are injected from the back wall of the chamber at equilibrium conditions with the same temperature as the wall temperature.

The results of this simulation heighten the concerns of the sidewall at this plenum pressure. The temperature contours shown in Figure 45 illustrate a hot viscous boundary layer on the side wall. The retardation of the flow may be seen in Figures 46 and 47, which present directed velocity and Mach numbers, respectively. The expansion of the gas is dampened by the viscous boundary layer formed on the side wall. It can be seen that the boundary layer is much thicker than in *Markelov et al*. (*2000*), as expected due to the corresponding lower pressure. This illustrates the importance of both high etch anisotropy and high plenum pressure in the minimization of viscous losses.

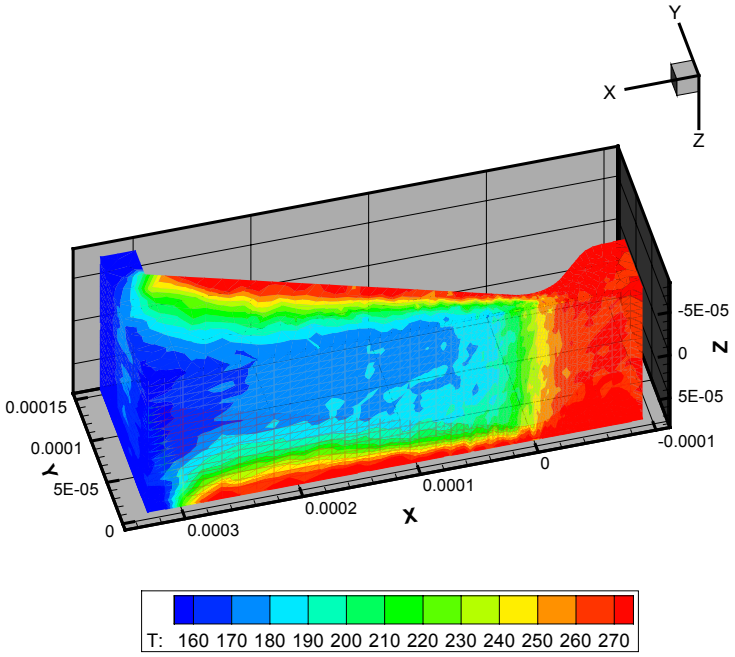

Figure 45. Temperature (in K) contours interior to MEMS nozzle.

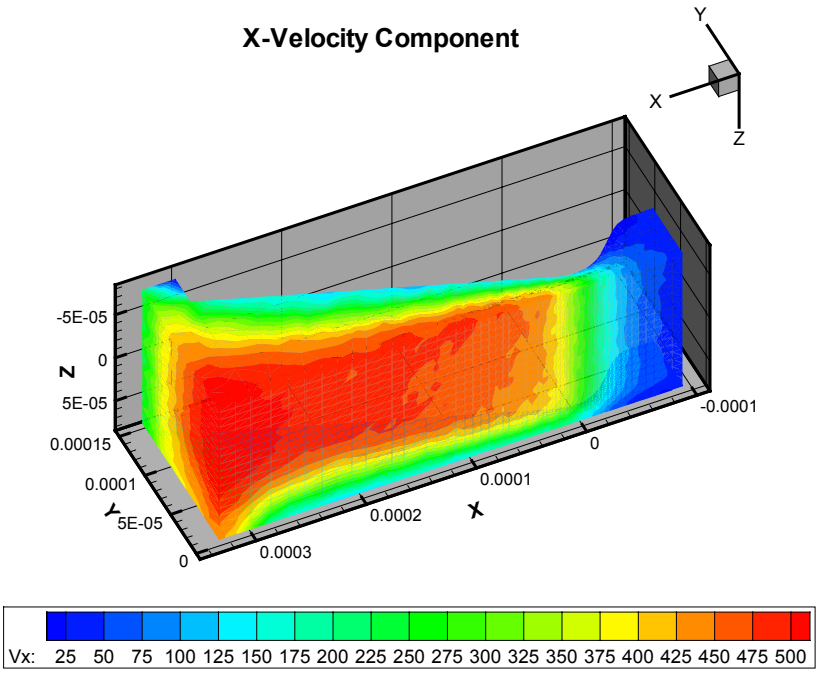

Figure 46. Effect of sidewalls on directed velocity (m/s). The top plane is a plane of symmetry, the bottom plane is the sidewall (diffusely reflecting).

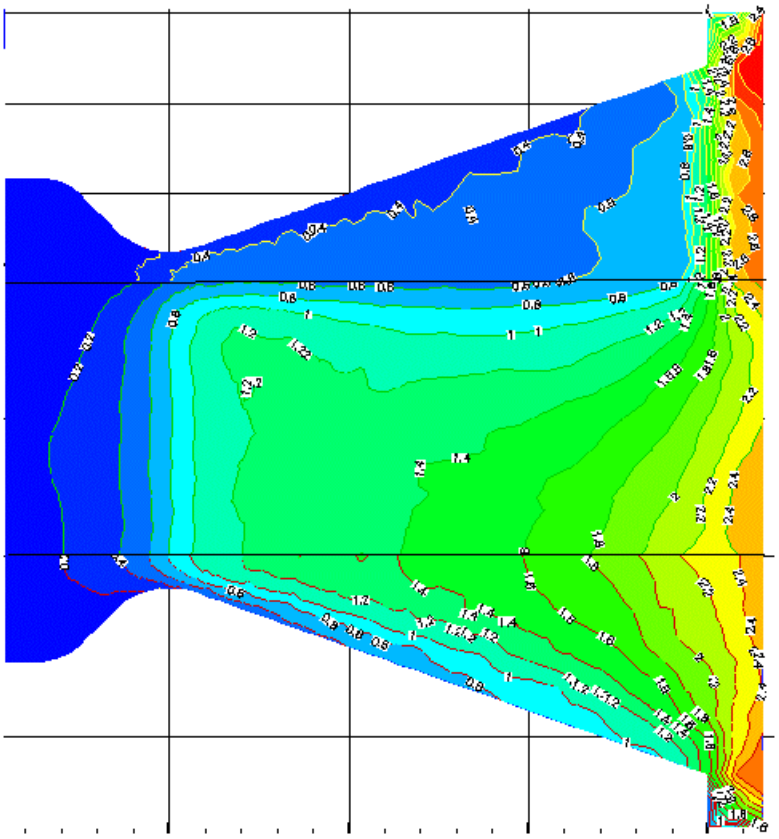

Figure 47. Mach contours of MEMS nozzle. The sidewall is at the top. The middle section is the plane of symmetry dividing the nozzle width-wise. The lower portion is the plane of symmetry dividing the nozzle height-wise.

Planar MEMS micronozzles operate at high nozzle efficiencies for large plenum pressures and highly anisotropic etches. As plenum pressures become lower or the etch depth becomes smaller, boundary layers formed on the side wall become important loss mechanisms. The DSMC method with the added flexibility of unstructured grids with adaptation can be used to aid in the understanding of viscous loss mechanisms and help in their elimination.

3.5 High Voltage Sheath

When the sheath drop is much larger than the plasma potential (both in volts), Child's law is observed. Simulation was done of the initial process of sheath formation in a domain bounded by two infinite planar electrodes with a voltage drop of 100 V. No current is injected into the domain, so the simulations differ from Child's law in this respect. However, the process of sheath formation remains much the same.

The domain was a thin cylindrical region 10 cm long with a diameter of about 0.1 cm. This extreme aspect ratio was used in order to have few enough cells to tackle this one-dimensional problem in three dimensions. The domain was initially loaded with a neutral plasma with a density of $1.0\times10^{13}\,\mathrm{m}^{-3}$ and an electron and ion temperature of 1 eV. The simulation results were compared with the code xpdp1 (http://ptsg.eecs.berkeley.edu). For the first $1.0\times10^{-8}\,\mathrm{s}$, the phase space results were nearly identical as shown in Figure 48. Electric field and potential profiles also compared favorably. However, after this time the results diverge, as the electrons in the unstructured code are not prevented from entering the sheath around the cathode as they are in the xpdp1 simulation. It is believed that this is caused by artificial heating of the plasma due to a poor quality gradient calculation and poor weighting procedures. As the gradient calculation suffers near the boundaries, the overall quality is poor on this mesh which has a high surface area to volume ratio. In order to simulate long-term behavior of a plasma, the accuracy of these procedures must be increased.

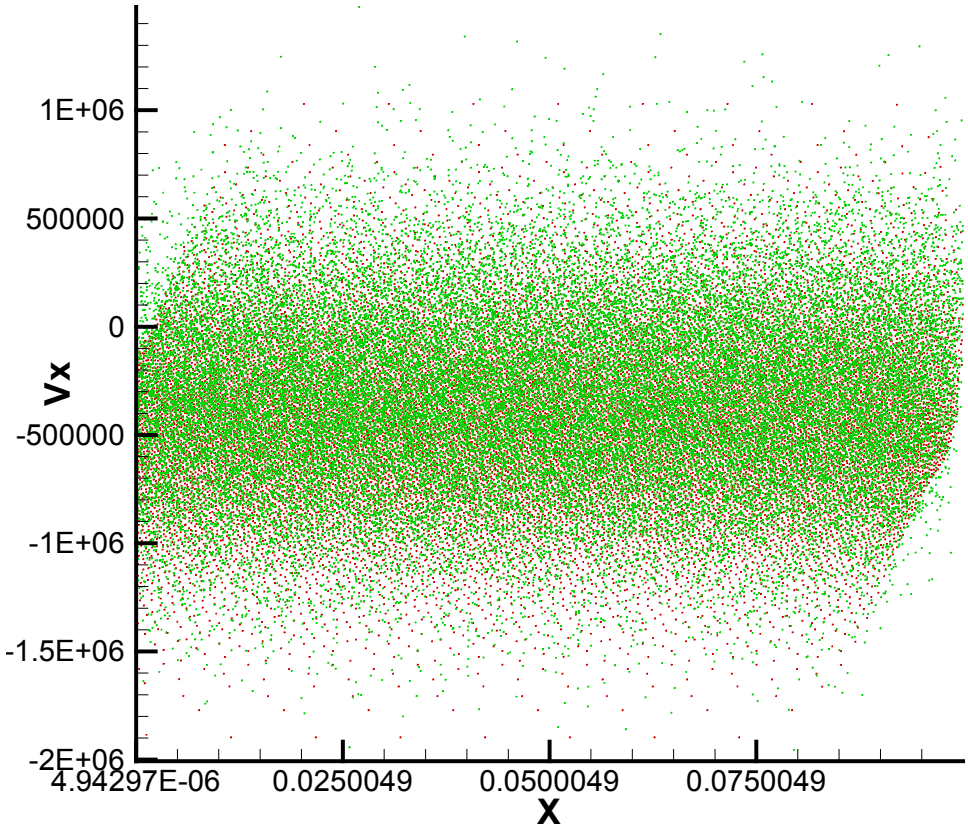

Figure 48. Electron X-Vx phase space. Red: xpdp1. Green: unstructured 3-D phase space.

Chapter 4

Conclusions and Recommendations

4.1 Conclusions

This thesis involved the development of a DSMC/PIC solver on unstructured grids. A surface generator was developed for the design of surfaces of engineering interest in the study of microthrusters. Grid quality was heuristically optimized to reduce lost particles and increase computational efficiency. Several improvements were made to the DSMC solver. First, the variable hard sphere model was added to the DSMC code in order to increase the accuracy of collision modeling. Second, internal degrees of freedom were added and verified. The implementation of these modules allowed us to perform DSCM simulations of micropropulsion devices.

A particle-in-cell program for the simulation of electrostatic plasmas was implemented on unstructured meshes. The code uses a finite volume approach for the solution of Poisson's equation. Several methods were investigated and implemented to evaluate the electric field on unstructured meshes. The integration of the particle equations of motion is done via the leap-frog method. Particle gather and scatter operations use volume weighting (linear Lagrange polynomials) to obtain an acceptable level of accuracy. Simulations were performed to assess the accuracy of the solution method and to gain insight into the gas dynamics of micropropulsion devices.

The DSMC solver was used to characterize flows in micronozzles. It was shown that as the chamber pressure decreased or the throat diameter increased, viscous losses increasingly reduced total nozzle thrust. Boundary conditions for such flows were assessed for the Gravity Probe-B nozzle, showing that it is important for simulation accuracy to match subsonic boundary conditions in the plenum.

The electrostatic PIC code was used to model a high voltage sheath. The accuracy of the electric field solver (discrete gradient operator) proved inadequate for long-term plasma simulations (for instance, comparable to a few microseconds necessary for the simulation of a micro-PPT). The numerical noise artificially heated the plasma, leading to increasingly inaccurate results with the procession of time. More work is needed to remedy this problem.

4.2 Recommendations for Future Work

1. Using a multiple domain approach with time steps and weights variable between domains may considerably increase computational efficiency, as each domain needs only to be resolved to local conditions. This is in contrast to global time-steps and weights over the entire flow field. Areas requiring high spatial and temporal resolution may be modeled separately and matched to their neighbors only in time increments. Also, areas with few computational particles under the single-weight system may achieve more accurate resolution of phase-space through use of a lower weight. The use of multiple domains also lends itself to parallelization of the program, which is required for any large-scale simulation.

2. In continuum conditions, such as a nozzle plenum, DSMC is computationally inefficient as very small cells and time steps must be used with a corresponding large number of particles. The use of a Navier-Stokes solver for neutral flows may greatly reduce this inefficiency. The Navier-Stokes equations (with or without velocity slip conditions at the wall) are solved in the continuum region and flow-field information is communicated to the DSMC flow solver. The location where the transition between the two numerical methods is made may be decided based on evaluation of a breakdown parameter (*Bird, 1970*) or chosen conservatively such that the continuum assumption is satisfied (*Ivanov et al., 1997*). The latter approach has the advantage of avoiding a complicated shape that bridges the regions, though care must be taken to ensure the cut-off breakdown parameter is not exceeded. Similarly, the test particle Monte Carlo method (*Bird, 1998*) may be used when collisions are not important and the flow is free-molecular. This method is illustrated in the context of thruster plume studies by *Ivanov et al*. (*1997*). The test particle Monte Carlo method is applicable also to ionized flows as long as close-range Coulomb collisions have little effect and the Lorentz force law is applied. The magnetogasdynamic (MGD) equations may be applied to ionized flows in the continuum regime, but only with the realization that there are multiple length and time scales in a plasma and the smallest scales must be satisfied. While a definitive semi-empirical breakdown criterion for gasdynamic flows has been defined by Bird, the author is unaware of any such universal criteria being defined for plasma flows. The application of a PIC-MGD solver must be done with care in order that kinetic effects are minimal in the region where the MGD

equations are applied. A region of overlap between the PIC and MGD methods may be necessary to ensure that the system is in quasi-equilibrium in the MGD solution region.

3. The primary advantage of unstructured tetrahedral grids is that any surface of engineering interest may be represented and meshed by a single grid generator. However, as noted in this study and elsewhere, a large percentage of the time is spent moving particles using ray-tracing techniques. In contrast, updating particle cell ownership and position on Cartesian grids is semi-automatic: in absence of boundary interactions, a particle is added to the cell determined through indexing of the particle's new position through division of the grid spacing. Drawing from the literature on finite element and finite volume methods, an approach may be used where a tetrahedral mesh is used near the boundaries and a Cartesian mesh, either structured or unstructured (*Bird, 1998*) is used in as much of the interior as possible. The location and direction to the nearest boundary is stored in each cell and particle location and cell ownership are updated semi-automatically when applicable. This would greatly increase computational efficiency in the flow far from the boundaries. This would require modification of the grid generator to mesh appropriate grids and the flow solver to take into account the type of cell for calculation purposes.

4. Local coordinates may be used to update particle position instead of global coordinates. The use of local coordinates may speed up particle motion as well as help prevent lost particles. The relevant data can be calculated once for each cell and stored to minimize running computation time. In addition, the weighting procedures

associated with linear Lagrange polynomials (volume weighting), which now consume much of the time in each electrostatic iteration, would become trivial.

5. Improved boundary conditions could be implemented for dielectrics, especially considering the external circuit case. Currently, only a constant-valued Neumann condition may be implemented and only the no-flux condition for circuit cases. The capacitance matrix may be formulated in terms of charge instead of voltage, and using this formulation a complete picture of the electrostatic potential could be developed in conjunction with the circuit methodology. In order to correctly model dielectrics, particle-surface interactions appropriate to the physics must also be implemented.

6. An improved method of obtaining the electric field is also desirable. Currently, field accuracy may be poor and may artificially heat the plasma. One possibility that avoids grid biases is the use of radial basis functions to compose the potential and differentiate these functions to obtain electric field components at the nodes.

7. A matrix solver based on a Krylov sub-space could be used to speed up the solution of the CRS matrix for Poisson's equation.

8. The use of the quiet start method reduces the initial noise and produces an ordered phase-space and should be implemented as well.

Bibliography

Anderson, John, Jr., Modern Compressible Flow With Historical Perspective, McGraw-Hill, Boston, 1990.

Baker, T.J., "Automatic Mesh Generation for Complex Three-Dimensional Regions Using a Constrained Delaunay Triangulation," Engineering With Computers, Springer-Verlag, No. 5, p161-175, 1989.

Bayt, R.L., "Analysis, Fabrication and Testing of a MEMS-based Micropropulsion System," Massachusetts Institute of Technology, FDRL TR 99-1, Ph. D. Thesis, June, 1999.

Bayt, R.L., Ayon, A.A., Breuer, K.S., "A Performance Evaluation of MEMS-based Micronozzles", AIAA 97-3169, 33rd AIAA/ASME/SAE/ASEE Joint Propulsion Conference & Exhibit, Seattle, Washington, July, 1997.

Bayt, R.L., Breuer, K.S., "Viscous Effects in Supersonic MEMS-fabricated Micronozzles," Proceedings of the 3rd ASME Microfluids Symposium, Anaheim, CA., November, 1998.

Bergemann, F., Boyd, I.D., "New Discrete Vibrational Energy Model for the Direct Simulation Monte Carlo Method," AIAA Progress in Astronautics and Aeronautics, Vol. 158, Proceedings of the Eighteenth International Symposium on Rarefied Gas Dynamics, Vancouver, Canada, July, 1992.

Bird, G.A., "Breakdown of Translational and Rotational Equilibrium in Gaseous Expansions," AIAA Journal, Vol. 8, No. 11, November, 1970.

Bird, G.A., "Monte-Carlo Simulation in an Engineering Context," Invited Paper 221, Twelfth International Symposium on Rarefied Gas Dynamics, Charlottesville, VA, July, 1980.

Bird, G.A., Molecular Gas Dynamics and the Direct Simulation of Gas Flows, Clarendon Press, Oxford, 1998.

Birdsall, C.K., "Particle-in-Cell Charged Particle Simulations, Plus Monte Carlo Collisions With Neutral Atoms, PIC-DSMC," IEEE Transactions on Plasma Science, Vol. 19, No. 2, April, 1991.

Birdsall, C.K., Langdon, A.B., Plasma Physics via Computer Simulation, Institute of Physics Publishing, Bristol, 1991.

Borgnakke, C., Larsen, P.S., "Statistical Collision Model for Monte Carlo Simulation of Polyatomic Gas Mixture," Journal of Computational Physics, Vl. 18, pp405-420, 1975.

Boris, J.P., "Relativistic plasma simulation-optimization of a hybrid code," Proceedings of the Fourth Conference on Numerical Simulation of Plasmas, Naval Res. Lab, Washington, D.C., 3-67, 2-3 November, 1970.

Borouchaki, H., George, P.L., "Aspects of 2-D Delaunay Mesh Generation," International Journal for Numerical Methods In Engineering, Wiley, Vol. 40, pp1957-1975, 1997.

Boyd, I.D., Jafry, Y., Vanden Beukel, J., "Particle Simulations of Helium Microthruster Flows", Journal of Spacecraft and Rockets, Vol. 31., No. 2, March-April, 1994.

Boyd, I.D., Jafry, Y., Vanden Beukel, J., "Investigation of Nozzle and Plume Expansions of a Small Helium Thruster," Proceedings of the Eighteenth International Symposium on Rarefied Gas Dynamics, Washington, D.C., 1994.

Boyd, I.D., Penko, P.F., Meissner, D.L., DeWitt, K.J., "Experimental and Numerical Investigations of Low Density Nozzle and Plume Flows of Nitrogen," AIAA Journal, Vol. 30, No. 10, October, 1992.

Cassady, J.R., Hoskins, W.A., Campbell, M., Rayburn, C., "A Micro Pulsed Plasma Thruster (PPT) for the 'Dawgstar' Spacecraft," *IEEE Aerospace Conference*, March, 2000.

Cheng, S., Dey, T.K., Edelsbrunner, H., Facello, M.A., Teng, S., "Sliver Exudation," J. ACM, 47(5):883-904, Sept., 2000.

Fehringer, M., Rüdenauer, F., Steiger, W., "Micronewton Indium Ion Thrusters," Proceedings of the 26th International Electric Propulsion Conference, Kitakyushu, Japan, October, 1999.

Gatsonis, N., Yin, X., "Numerical Investigation of Pulsed Plasma Thruster Plumes," Proceedings of the 25th International Electric Propulsion Conference, Cleveland, Ohio, August, 1997.

Gatsonis, N., Yin, X., "Theoretical and Computational Analysis of Pulsed Plasma Thruster Plumes," Proceedings of the 25th International Electric Propulsion Conference, Cleveland, Ohio, August, 1997.

Gatsonis, N., Nanson, R., LeBeau, G., "Navier-Stokes/DSMC Simulations of Cold-Gas Nozzle/Plume Flows and Flight Data Comparisons," AIAA Paper 99-3456, 33rd Thermophysics Conference, Norfolk, VA, July, 1999.

de Groot, W.A., Reed, B.D., Brenizer, M., "Preliminary Results of Solid Gas Generator Micropropulsion," AIAA Paper 98-3225, 34th Joint Propulsion Conference, Cleveland, OH, July, 1998.

Gulczinski III, F.S., Dulligan, M.J., Lake, J.P., Spanjers, G.G., "Micropropulsion Research at AFRL," AIAA 2000-3255, 38th Joint Propulsion Conference & Exhibit, Huntsville, Alabama, July, 2000.

Hammel, J., Kovalev, K., Gatsonis, N.A., "Unstructured Adaptive Monte Carlo Simulations of Flows in Micronozzles," AIAA 2001-2891, 35th AIAA Thermophysics Conference, Anaheim, California, June, 2001.

Hammel, J., "Description of the DSMC/PIC Code," CGPL Report, 2001.

Haus, H.A., Melcher, J.R., Electromagnetic Fields and Energy, Prentice-Hall, Inc., London, 1989.

Hermeline, "Two Coupled Particle-Finite Volume Methods Using Delaunay-Voronoï Meshes for the Approximation of Vlasov-Poisson and Vlasov-Maxwell Equations," Journal of Computational Physics, Vol. 106, 1993.

Ivanov, M.S., Markelov, G.N., Kashkovsky, A.V., Giordano, D., "Numerical Analysis of Thruster Plume Interaction Problems," ESPC 97-A5/3, 2nd European Space Propulsion Conference, Noordwijk, NL, May, 1997.

Ivanov, M.S., Markelov, G.N., "Numerical Study of Cold Gas Micronozzle Flows," AIAA Paper 99-0166, 37th Aerospace Sciences Meeting & Exhibit, Reno, Nevada, January, 1999.

Ivanov, M.S., Markelov, G.N., "Numerical study of thruster nozzle plume," AIAA Paper 2000-0468, 38th AIAA Aerospace Sciences Meeting & Exhibit, Reno, NV, January, 2000.

Jackson, J. D., Classical Electrodynamics, Third Edition, John Wiley & Sons, Inc., New York, 1999.

Jafry, Y., Vanden Beukel, J., "Ultralow density plume measurements using a helium mass spectrometer," Journal of Vacuum Science and Technology, July/Aug., 1992.

Jahn, Robert G., Physics of Electric Propulsion, McGraw-Hill Book Company, New York, 1968.

Janson, S.W., Helvajian, H., Breuer, K., "MEMS Microengineering and Aerospace Systems," AIAA Paper AIAA 99-3802, 1999.

Kamhawi, H., Turchi, P.J., Leiweke, R.J., "Design and Operation of a Laboratory Bench-Mark Thruster," AIAA 96-2732, 32nd AIAA/ASME/SAE/ASEE Joint Propulsion Conference, Lake Buena Vista, FL, July, 1996.

Kantor, A.L., Long, L.N., Micci, M.M., "Molecular Dynamics Simulation of Dissociation Kinetics," AIAA Paper AIAA-2000-0213, 2000.

Keefer, D., Rhodes, R., "Electromagnetic Acceleration in Pulsed Plasma Thrusters," IEPC 97-035, International Electric Propulsion Conference, 1997.

Ketsdever, A.D., Wadsworth, D.C., Vargo, S.E., Muntz, E.P., "The Free Molecule Micro-Resistojet: An Interesting Alternative to Nozzle Expansion," AIAA Paper AIAA 98-3918, 1998.

Ketsdever, A.D., Wadsworth, D.C., Vargo, S.E., Muntz, E.P., "Flow Properties of a Free Molecule Micro-resistojet for Small Spacecraft Application," Proceedings of the 21st International Symposium on Rarefied Gas Dynamics, Marseille, France, July, 1998.

Ketsdever, A.D., Micci, M.M., *Micropropulsion for Small Spacecraft*, Progress in Astronautics and Aeronautics, Vol. 187, edited by M. Micci and A Ketsdever, AIAA, Reston, VA, 2000, Preface.

Kovalev, Konstantin, "Development of a 2-D/3-D Unstructured Adaptive Grid Generator for Direct Simulation Monte Carlo Computations," Master's Thesis, Worcester Polytechnic Institute, 2000.

Li, Xiang-Yang, "Spacing Control and Sliver-free Delaunay Mesh," *Proceedings, 9th International Meshing Roundtable*, Sandia National Laboratories, pp.295-306, October, 2000.

Lieberman, M.A., Lichtenberg, A.J., Principles of Plasma Discharges and Materials Processing, John Wiley & Sons, Inc., New York, 1994.

Madsen, N. K., "Divergence Preserving Surface Integral Methods for Maxwell's Curl Equations Using Non-orthogonal Unstructured Grids," Journal of Computational Physics, Vol. 119, 1995.

Marrese, C.M., Wang, J.J., Gallimore, A.D., Goodfellow, K.D., "Space-Charge-Limited Emission from Field Emission Cathodes for Electric Propulsion and Tether Applications," Micropropulsion for Small Spacecraft, Progress in Astronautics and Aeronautics Vol. 187, ed. Micci, M.M., and Ketsdever, A.D., American Institute for Aeronautics and Astronautics, Reston, Virginia, 2000.

Mueller, Juergen, "Thruster Options for Microspacecraft: A Review and Evaluation of State-of-the-Art and Emerging Technologies," *Micropropulsion for Small Spacecraft*, Progress in Astronautics and Aeronautics, Vol. 187, edited by M. Micci and A Ketsdever, AIAA, Reston, VA, 2000, Chapter 3.

Mullins, Jennifer, www@relgyro.Stanford.EDU, *Private Communication*, September 22, 2000.

Nanbu, Kenichi, "Probability Theory of Electron-Molecule, Ion-Molecule, Molecule-Molecule, and Coulomb Collisions for Particle Modeling of Materials Processing Plasmas and Gases," IEEE Transactions on Plasma Science, Vol. 28, No. 3, June, 2000.

Piekos, E.S., Breuer, K.S., "DSMC Modeling of Micromechanical Devices," AIAA Paper 95-2089, 30th AIAA Thermophysics Conference, San Diego, CA, June, 1995.

Piekos, E.S., Breuer, K.S., "Numerical Modeling of Micromechanical Devices Using the Direct Simulation Monte Carlo Method," Journal of Fluids Engineering, Vol. 118, September, 1996.

Rothe, Dietmar E., "Electron-Beam Studies of Viscous Flow in Supersonic Nozzles", AIAA Journal, Vol. 9, No. 5, May, 1971.

Sarkis, Marcus, *MA 590 Special Topics: Parallel Processing*, Class Notes, Worcester Polytechnic Institute, Fall, 2000.

Schilling, J.H., Spores, R.A., Spanjers, G.G., "Micropropulsion Options for the TechSat21 Space-Based Radar Flight," *Micropropulsion for Small Spacecraft*, Progress in Astronautics and Aeronautics, Vol. 187, edited by M. Micci and A Ketsdever, AIAA, Reston, VA, 2000, Chapter 1.

Tannehill, J.C., Anderson, D.A., Pletcher, R.H., Computational Fluid Mechanics and Heat Transfer, Second Edition, Taylor & Francis, Washington, DC, 1997.

Thomas, V.A., Jones, M.E., Piket-May, M., Taflove, A., Harrigan, E., "The Use of SPICE Lumped Circuits as Sub-grid Models for FDTD Analysis," IEEE Microwave and Guided Wave Letters, Vol. 4, No. 5, May, 1994.

Vahedi, V., DiPeso, G., "Simultaneous Potential and Circuit Solution for Two-Dimensional Bounded Plasma Simulation Codes," Journal of Computational Physics, Vol. 131, pp149-163, 1997.

Vencenti, W.G., Kruger, C.H., Introduction to Physical Gas Dynamics, John Wiley and Sons, Inc., New York, 1965.

Verboncoeur, J.P., Alves, M.V., Vahedi, V., Birdsall, C.K., "Simultaneous Potential and Circuit Solutions for 1D Bounded Plasma Particle Simulation Codes," Journal of Computational Physics, Vol. 104, pp321-328, 1993.

Villasenor, J., Buneman, O., "Rigorous charge conservation for local electromagnetic field solvers," Computer Physics Communications, 69, pp306-316, 1992.

Vondra, R.J., Thomassen, K., Solbes, A., "Analysis of Solid Teflon Pulsed Plasma Thruster," Journal of Spacecraft and Rockets, Vol. 7, No. 12, December, 1970.

Wachman, H.Y., "Thermal Accommodation Coefficient: The Contributions of Lloyd Brewster Thomas," Proceedings of the 18th International Symposium on Rarefied Gas Dynamics, Vancouver, Canada, July, 1992.

Wang, J., Kondrashov, D., Liewer, P. C., "A study of stability and energy conservation of a 3-D electromagnetic PIC code for non-orthogonal meshes," IEEE International Conference on Plasma Science, 1997.

Watson, D.F., "Computing the Delaunay Tessellation with Application to Voronoi Prototypes," The Computer Journal, Vol. 24(2), pp167-172, 1981.

Yee, Kane S., "Numerical Solution of Initial Boundary Value Problems Involving Maxwell's Equations in Isotropic Media," IEEE Transactions on Antennas and Propogation, Vol. AP-14, No. 3, May, 1966.

Zelesnik, D., Micci, M.M., Long, L.N., "DSMC Simulation of Low Reynolds Number Nozzle Flows," AIAA Paper 93-2490, 29th AIAA/SAE/ASME/ASEE Joint Propulsion Conference and Exhibit, Monterey, CA, June, 1999.